Volume: 3 Issue: 1   2022

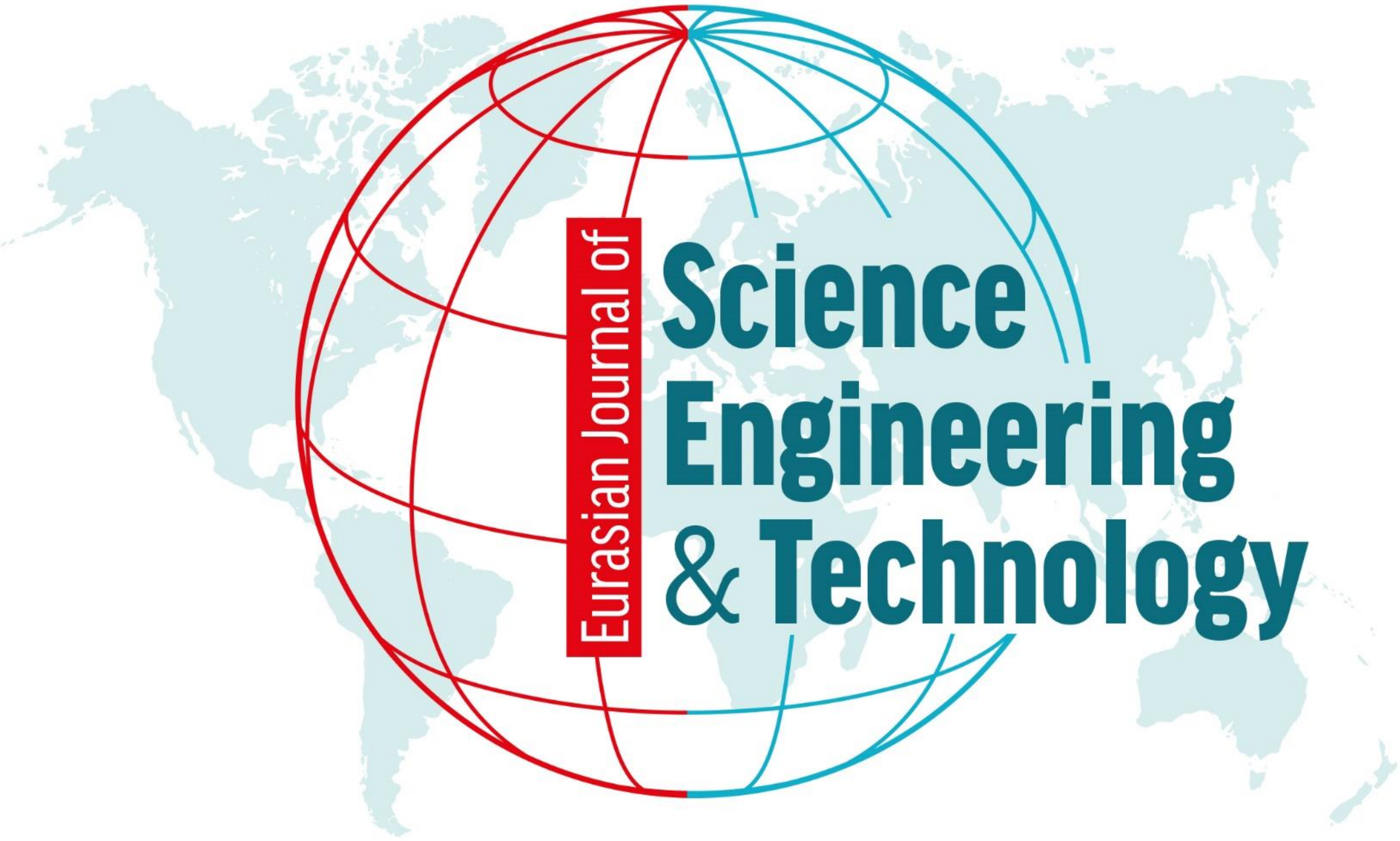

Eurasian Journal of Science Engineering and Technology

Editors

Prof. Dr. Murat BARUT, mbarut@ohu.edu.tr, NIGDE OMER HALISDEMIR UNIVERSITY

Assoc. Prof. Recep ZAN, recep.zan@ohu.edu.tr, NIGDE OMER HALISDEMIR UNIVERSITY

Editorial Board

Zeliha YILDIRIM, zeliha.yildirim@ohu.edu.tr, NIGDE OMER HALISDEMIR UNIVERSITY

Bora TİMURKUTLUK, bora.timurkutluk@ohu.edu.tr, NIGDE OMER HALISDEMIR UNIVERSITY

Alper GÜRBÜZ, agurbuz@ohu.edu.tr, NIGDE OMER HALISDEMIR UNIVERSITY

Metin Hakan SEVERCAN, msevercan@ohu.edu.tr, NIGDE OMER HALISDEMIR UNIVERSITY

Serkan ÇAYIRLI, scayirli@ohu.edu.tr, NIGDE OMER HALISDEMIR UNIVERSITY

Sevgi DEMİREL, sevgidemirel@ohu.edu.tr, NIGDE OMER HALISDEMIR UNIVERSITY

Yasemin ALTUNCU, yaltuncu@ohu.edu.tr, NIGDE OMER HALISDEMIR UNIVERSITY

Kutalmış GÜMÜŞ, kgumus@ohu.edu.tr, NIGDE OMER HALISDEMIR UNIVERSITY

Çiğdem ULUBAŞ SERÇE, cigdemserce@ohu.edu.tr, NIGDE OMER HALISDEMIR UNIVERSITY

Sibel CANOĞULLARI, scanogullari@ohu.edu.tr, NIGDE OMER HALISDEMIR UNIVERSITY

Ufuk DEMİREL, ufukdemirel@ohu.edu.tr, NIGDE OMER HALISDEMIR UNIVERSITY

Tefide KIZILDENİZ, tkizildeniz@ohu.edu.tr, NIGDE OMER HALISDEMIR UNIVERSITY

Halil TOKTAY, h.toktay@ohu.edu.tr, NIGDE OMER HALISDEMIR UNIVERSITY

Hakan DEMİR, hdemir@ohu.edu.tr, NIGDE OMER HALISDEMIR UNIVERSITY

Gazi GÖRÜR, ggorur@ohu.edu.tr, NIGDE OMER HALISDEMIR UNIVERSITY

Durmuş DAĞHAN, durmusdaghan @ohu.edu.tr, NIGDE OMER HALISDEMIR UNIVERSITY

Sefa ERTÜRK, sefa@ohu.edu.tr, NIGDE OMER HALISDEMIR UNIVERSITY

Ersen TURAÇ, ersenturac@ohu.edu.tr, NIGDE OMER HALISDEMIR UNIVERSITY

Eurasian Journal of Science Engineering and Technology

Scientific Board

Kutsi Savaş ERDURAN, kserduran@ohu.edu.tr, NIGDE OMER HALISDEMIR UNIVERSITY

Mehmet EMİN ÇALIŞKAN, caliskanme@ohu.edu.tr, NIGDE OMER HALISDEMIR UNIVERSITY

Aydın TOPÇU, aydintopcu@ohu.edu.tr, NIGDE OMER HALISDEMIR UNIVERSITY

Gazi GÖRÜR, ggorur@ohu.edu.tr, NIGDE OMER HALISDEMIR UNIVERSITY

Neslihan DOĞAN SAĞLAMTİMUR, nds@ohu.edu.tr, NIGDE OMER HALISDEMIR UNIVERSITY

Murat GÖKÇEK, mgokcek@ohu.edu.tr, NIGDE OMER HALISDEMIR UNIVERSITY

Metin YILDIRIM, metin.yildirim@ohu.edu.tr, NIGDE OMER HALISDEMIR UNIVERSITY

Bora TİMURKUTLUK, bora.timurkutluk@ohu.edu.tr, NIGDE OMER HALISDEMIR UNIVERSITY

Cahit Tağı ÇELİK, ctcelik@ohu.edu.tr, NIGDE OMER HALISDEMIR UNIVERSITY

Öner Yusuf TORAMAN, otoraman@ohu.edu.tr, NIGDE OMER HALISDEMIR UNIVERSITY

Mehmet ŞENER, msener@ohu.edu.tr, NIGDE OMER HALISDEMIR UNIVERSITY

Çiğdem ULUBAŞ SERÇE, cigdemserce@ohu.edu.tr, NIGDE OMER HALISDEMIR UNIVERSITY

Tefide KIZILDENİZ, tkizildeniz@ohu.edu.tr, NIGDE OMER HALISDEMIR UNIVERSITY

Ayten ÖZTÜRK, aozturk@ohu.edu.tr, NIGDE OMER HALISDEMIR UNIVERSITY

Adil CANIMOĞLU, acanimoglu@ohu.edu.tr, NIGDE OMER HALISDEMIR UNIVERSITY

Atakan Tuğkan YAKUT, sevaty@ohu.edu.tr, NIGDE OMER HALISDEMIR UNIVERSITY

Ersen TURAÇ, ersenturac@ohu.edu.tr, NIGDE OMER HALISDEMIR UNIVERSITY

Mustafa UÇAN, ucan@ohu.edu.tr, NIGDE OMER HALISDEMIR UNIVERSITY

Osman SEYYAR, oseyyar@ohu.edu.tr, NIGDE OMER HALISDEMIR UNIVERSITY

Eurasian Journal of Science Engineering and Technology

Correspondence Address

Niğde Ömer Halisdemir University
Eurasian Journal of Science Engineering and Technology Publishing Coordinatorship, 51240 Niğde/Turkey

E-mail**:** recep.zan@ohu.edu.tr

Web page**:** https://dergipark.org.tr/tr/pub/ejset

Publication information

The objective of Eurasian Journal of Science Engineering and Technology (EJSET) is to provide an academic environment for researchers in various fields of science and engineering and for the publication and dissemination of high-quality research results in the fields of science, applied science, engineering, architecture, agricultural science and technology.

Eurasian Journal of Science Engineering and Technology

İÇİNDEKİLER/*CONTENTS*

Eurasian Journal of Science Engineering and Technology

Research

EARLY GENERATION SELECTION IN DIFFERENT LOCATIONS IN POTATO BREEDING PROGRAM

Özge KOYUTÜRK[1,*], Güngör YILMAZ[2]

[1]*Middle Black Sea Transitional Zone Agricultural Research Institute, Tokat, Turkey*
[2]*Yozgat Bozok University, Faculty of Agriculture, Department of Field Crops, Yozgat, Turkey*

ABSTRACT

In variety development studies through hybridization, it is necessary to make hybridization with the parents suitable for the purpose, to obtain the tubers in seedling generation from the hybrid seeds obtained, and then to proceed to the clonal selection process. In this study, it was aimed to select clones suitable for tuber shape, earliness, table and industrial use in different locations in the first clonal generation stage from the variation created by hybridization between some commercially registered potato varieties, local potato varieties and some clones with superior characteristics. The study was conducted with 3316 clones in Artova and Kazova districts in Tokat province in Turkey. In this year, which was the first clonal selection stage, besides phenotypic characteristics such as breeder's preference, maturity group, tuber defects, skin roughness, skin and tuber flesh color, characteristics such as the number of tubers per hill, tuber yield per hill, average tuber weight, depth of lateral (eye) and apical buds were examined and data on clones belonging to each hybrid family were obtained. Thus, it was decided to proceed to the next selection stage with 918 clones selected due to their compliance with the criteria determined in the first clonal generation stage.

Keywords: First Clonal Generation, Potato, *Solanum tuberosum* L., Selection

1. INTRODUCTION

The aim of potato breeding is to develop varieties that are high yielding, early-maturing, suitable for the intended use, high quality, high adaptable, suitable for storage, resistant to diseases-pests and tolerant to stress factors [1], [2]. In order to achieve this goal, the phenotypic selection is made in each generation.

New cultivar development stages in potato breeding; are parental selection, hybridization between parents, starting F1 seedling generation by producing seedlings from the seeds obtained, selection of clones with the desired characters as a result of selection studies, and reaching a sufficient amount of selected clones. After that, clones are tested in some locations and superior varieties are registered and produced [3].

Potato clones are selected from F1 progeny by vegetative propagation without genetic modifications. Breeding experiments are largely based on phenotypic selection for yield and other related characteristics. On the other hand, due to the limited resources, it is not possible to examine all characteristics that can contribute to breeding goals [4].

In potato breeding, the selection made in the early generation period is mostly based on the experience of the breeder by examining at the external appearance of the plant and tuber. It is very important to use the phenotypic selection parameters optimally to achieve a maximum gain in variety development. For instance, about 18 phenotypic selection parameters are used in Agriculture and Agri-Food's breeding program. Phenotypic selection in the early period comprises characteristics such as tuber size, eye depth, number of eyes, early maturity, maturity group, etc. [5]. on the other hand, made evaluations on eye depth, apical bud depth, tuber shape, tuber size and general appearance and total yield in clones belonging to 12 hybrid families in their selection in terms of tuber yield and appearance [6].

Yılmaz et al. (2017a) stated that in order to develop new varieties in potatoes, it is necessary to make hybridization with suitable parents, to develop seed tubers by using hybrid seeds, seedling generation, and to proceed to the first clonal selection stage with these tubers. In their research, it was aimed to develop seed tubers required for the first clonal selection after seedling generation by using hybrid seeds from different potato combinations. The first field generation selection was made with approximately 8800 clones in their study, and as a result of the selection, 1186 clones suitable for marketable tuber characteristics were determined [7].

Yakar-Tan and Bilge (1979) stated that the variations to be observed when plants with the same genotype are grown in different places are caused by the environment. Furthermore, they reported that the issue of whether the genotype or environmental conditions have a greater effect on the phenotype can be determined by growing plants with different genotypes

---

* Corresponding author, e-mail: ozge.koyuturk@tarimorman.gov.tr (Ö. Koyutürk)
Recieved: 02.12.2021   Accepted: 08.02.2022
doi: 10.55696/ejset.1031168

in the same environmental conditions or growing individuals with the same genotype under different environmental conditions [8] Each new variety must be sustainable against changes in agricultural and climatic conditions [9]. Therefore, it is important to try these varieties in suitable environments for several years. Many characteristics of potatoes such as tuber yield, tuber number and size, dry matter content and quality are greatly affected by the environmental conditions in which the plant is grown [10]. In the present study, it was aimed to select clones that show superior characteristics in terms of tuber shape, earliness, cooking and industrial use in different locations in the first clonal generation stage from the segregated population created by hybridization between some commercial registered potato varieties, local potato varieties and some clones with superior characteristics.

2. MATERIAL AND METHOD

In the study, the variation was created by hybridization with some commercially registered potato varieties, some local potato varieties currently being produced in the high altitudes of Tokat province, and clones with some superior characteristics developed by the TÜBİTAK-TOVAG project numbered 106 O 626. The study was carried out in Tokat / Kazova (600-650 m) and Tokat / Artova (1100 m) locations in 2017.

The planting density of 3316 hybrid clones belonging to six combinations was 70x40 cm, and if the number was sufficient for each of the clones, two tubers each, if not enough, one tuber was planted (Table 1). The clones were planted in Tokat / Kazova on 30-31 March 2017 and in Artova on 15 May 2017. All treatments required for cultivation were carried out at this stage, and irrigation was carried out with the drip irrigation method in Artova location and with the sprinkler irrigation method in Kazova location. According to the results of soil analysis, fertilization was carried out as 20 kg Nitrogen, 10 kg Phosphorus and Potassium per decare. In the Tokat / Kazova location, the early-maturing clones were harvested on 16-17 August 2017, while the other clones were harvested on 6-13 September 2017. Moreover, the harvest in Tokat / Artova location was made on 17-18 October 2017. Tubers belonging to the plants in both locations were labeled separately, bagged and stored, then necessary observations and measurements were performed. In the first clonal generation, the clones belonging to each hybrid family were grown in two locations and started to be monitored. Clones with disease and clones with abnormal growth and habitus structure were removed before harvesting. The selection study was mostly carried out after the harvest. Moreover, the clones that were rough, cracked, cleft, shapeless, rotten, and clones that had the high depth of eye and apical bud, could not grow their tubers sufficiently and had an insufficient number of tubers were eliminated by the negative selection.

Table 1 Combinations and number of clones examined in the experiment

Combination	Parent-1		Parent-2	Number of hybrid clon
1	Slaney	x	T5/4	384
2	Başçiftlik Beyazı	x	Lady Olympia	526
3	A3/15	x	Bafana	690
4	Başçiftlik Beyazı	x	Slaney	769
5	T5/4	x	Marfona	613
6	T5/4	x	Bafana	334
Total				3 316

3. RESULTS AND DISCUSSION

In the present study, in the first clonal selection stage, besides phenotypic characteristics such as breeder's preference, plant growth form, tuber defects, skin roughness, skin and tuber flesh color, characteristics such as the number of tubers per hill, tuber yield per hill, average tuber weight, depth of eye and apical bud were considered.

3.1. Breeder's Preference Scale

Unlenen (2010) stated that different plant characteristics were taken into consideration before and after the harvest. Criteria such as plant height, plant growth type, stolon length, stem thickness, and maturity can be considered before the harvest while criteria such as stolon length, tuber shape, tuber defect, eye depth, skin smoothness, number of tubers per plant and yield can be considered during and after the harvest [11] According to the general appearance of the plants under field conditions and the tubers after the harvest, they were scored as 1- Very Bad, 2-Bad, 3- Medium, 4- Good, 5- Very Good and determined by taking their means. The clones belonging to the hybrid families were evaluated by the scoring parameters such as the affection level of the plants by diseases, growth form, stolon length and branching status, tuber shape, tuber color, tuber form, general appearance and bulk homogeneity of the tubers. Among the combinations in Kazova location, A3 / 15 x Bafana (11.3%) and Başçiftlik Beyazı x Lady Olympia (8.3%) had the highest number of clones in the very good category in terms of overall appearance (Table 2). Moreover, the clones evaluated at the Artova location belonging to the combinations of Slaney x T5 / 4 (7.6%) and Başçiftlik Beyazı x Lady Olympia (7.7%) were found to be very good in terms of general appearance before and after the harvest (Table 2).

Table 2 Evaluation of clones belonging to hybrids from Kazova and Artova locations according to the breeder's preference

Combination	**Number of plants**	**Very bad**	**%**	**Bad**	**%**	**Medium**	**%**	**Good**	**%**	**Very good**	**%**
Kazova											
1	274	16	5.8	71	25.9	84	30.7	93	33.9	10	3.6
2	349	27	7.7	57	16.3	121	34.7	115	33.0	29	8.3
3	506	9	1.8	50	9.9	190	37.5	200	39.5	57	11.3
4	615	21	3.4	150	24.4	257	41.8	162	26.3	25	4.1
5	468	43	9.2	205	43.8	151	32.3	60	12.8	9	1.9
6	265	15	5.7	82	30.9	101	38.1	53	20.0	14	5.3
Total	2 477	131	-	615	-	904	-	683	-	144	-
Average	-	22	5.6	102	25.2	151	35.8	114	27.6	24	5.7
Artova											
1	172	5	2.9	44	25.6	60	34.9	50	29.1	13	7.6
2	313	14	4.5	87	27.8	67	21.4	121	38.7	24	7.7
3	316	7	2.2	84	26.6	82	25.9	129	40.8	14	4.4
4	489	11	2.2	128	26.2	198	40.5	135	27.6	17	3.5
5	332	21	6.3	58	17.5	88	26.5	142	42.8	23	6.9
6	96	5	5.2	34	35.4	16	16.7	37	38.5	4	4.2
Total	1 718	63	-	435	-	511	-	614	-	95	-
Average	-	10	3.9	72	26.5	85	27.7	102	36.2	16	5.7
1=Slaney x T5/4, 2= Başçiflik Beyazı x Lady Olympia, 3=A3/15 x Bafana, 4=Başçiflik Beyazı x Slaney, 5=T5/4 x Marfona, 6= T5/4 x Bafana											

3.2. Plant Maturing Group

After sprouting, and before the five leaves at the top dried, observations were made and very early-maturing, early-maturing, medium early-maturing, late-maturing, and very late-maturing clones were determined. Of the 2476 clones examined in the Kazova location, 2.5% were found to be very early-maturing, 15.5% were early-maturing, 28.3% were medium early-maturing, 31.0% were late-maturing and 21.1% were very late-maturing (Table 3). When the plant maturing groups of the clones were examined in the Artova location, it was determined that 2.9% were very early-maturing, 7.9% were early-maturing, 31.1% were medium early-maturing, 38.3% were late-maturing and 19.9% were very late-maturing (Table 3). It is seen that the number of clones found to be late-maturing in both locations was high. It is thought that this situation was due to the fact that the maturity status of the parents used in crossbreeding was mostly late.

In a study conducted, it was investigated what percentage of clones could be lost when late-maturing clones were discarded, and the clones were examined under five groups as very early-maturing, early-maturing, mid-early-maturing, late-maturing and very late-maturing. Moreover, plant vitality (very weak, weak, medium, high, very high) was also scored. While 20% of the genotypes were found to be in the late-maturing group, 9.2% were in the very early-maturing group. Besides, it was concluded that 6.2% of late-maturing genotypes could be lost [12]. There is no problem with the loss of early-maturing plants, however, late-maturing plants can be eliminated due to this feature. However, if the plants are grown in short-day conditions, this risk can be eliminated since early tuber formation and early ripening will be encouraged [13].

Table 3 Plant maturing group of clones belonging to hybrids from Kazova and Artova locations (number)

Combination	**Number of plant**	**Very early-maturing**	**%**	**Early-maturing**	**%**	**Medium early-maturing**	**%**	**Late-maturing**	**%**	**Very late-maturing**	**%**
Kazova											
1	273	5	1.8	25	9.2	79	28.9	105	38.5	59	21.6
2	349	8	2.3	32	9.2	65	18.6	125	35.8	119	34.1
3	506	18	3.6	178	35.2	146	28.9	100	19.8	64	12.6
4	615	19	3.1	46	7.5	156	25.4	187	30.4	207	33.7
5	468	12	2.6	68	14.5	143	30.6	175	37.4	70	15.0
6	265	4	1.5	47	17.7	100	37.7	64	24.2	25	9.4
Total	2 476	66	-	396	-	689	-	756	-	544	-
Average	-	11	2.5	66	15.5	115	28.3	126	31.0	91	21.1
Artova											
1	172	3	1.7	12	7.0	43	25.0	67	39.0	47	27.3
2	313	13	4.2	16	5.1	78	24.9	106	33.9	100	31.9
3	316	8	2.5	21	6.6	200	63.3	52	16.5	35	11.1
4	489	9	1.8	37	7.6	91	18.6	236	48.3	116	23.7
5	332	16	4.8	56	16.9	164	49.4	64	19.3	32	9.6
6	96	2	2.1	4	4.2	5	5.2	70	72.9	15	15.6
Total	1 718	51	-	146	-	581	-	595	-	345	-
Average	-	8	2.9	24	7.9	97	31.1	99	38.3	57	19.9
1=Slaney x T5/4, 2= Başçiflik Beyazı x Lady Olympia, 3=A3/15 x Bafana, 4=Başçiflik Beyazı x Slaney, 5=T5/4 x Marfona, 6= T5/4 x Bafana											

3.3. Tuber Defects

Defects such as cracks, clefts, formlessness and secondary tuber formation, deformity and swollen eyes seen in the skin of the tubers were macroscopically observed and it was determined that if they were present or not. When the tuber defects belonging to the hybrid families in the Kazova location were examined, it was observed that 48% of the total 2477 clones did not have tuber defects, however, 51.7% of them had problems such as wrinkling, rotting, softening, secondary tuber formation, cracking, splitting, and deformity (Table 4). While 43.6% of tubers harvested from Artova location did not have any negative characteristics, 56.4% of tubers in Kazova location had defects (Table 4). In a study conducted by Ünlenen (2010), the values obtained from the scoring based on the observations at the first clonal generation stage were examined. In the research, it was determined that the rate of genotype with any tuber defect was 18.0%, and no tuber defect was observed in 82.0% of the genotypes [11]

Table 4 Tuber defect values of clones belonging to hybrids in Kazova and Artova locations

Combination	Number of plant	Any tuber defect	%	No tuber defect	%
Kazova					
1	273	142	52.0	131	47.9
2	349	203	58.2	146	41.8
3	506	240	47.4	266	52.6
4	615	235	38.2	380	61.8
5	468	244	52.1	224	47.9
6	265	132	49.9	133	50.2
Total	2 476	1 197	-	1 280	-
Average	-	199.3	49.6	213.3	50.3
Artova					
1	172	59	34.3	113	65.7
2	313	146	46.6	167	53.4
3	316	180	57.0	136	43.0
4	489	156	31.9	333	68.0
5	332	142	42.8	190	57.2
6	96	66	68.8	30	31.3
Total	1 718	750	-	969	-
Average	-	124.8	46.9	161.5	53.1
1=Slaney x T5/4, 2= Başçiflik Beyazı x Lady Olympia, 3=A3/15 x Bafana, 4=Başçiflik Beyazı x Slaney, 5=T5/4 x Marfona, 6= T5/4 x Bafana					

3.4. The Number of Tubers per Hill

The number of tubers per hill was determined by counting the tubers in each hill. As seen in Table 5, the average number of tubers per hill of 2476 clones examined in the Kazova location was 10.59. When the number of tubers was examined on a combination basis, the highest tuber number per hill was obtained from T5 / 4 x Marfona combination with 11.90 while the lowest tuber number per hill was obtained from the Başçiftlik Beyazı x Lady Olympia combination with 8.50. There were 1132 clones above the average. When the mean number of tubers per hill in Artova location was evaluated, the mean of 1718 clones was 4.54 and 676 clones were above the average.

When the combinations are considered, it is observed that, Başçiftlik Beyazı x Slaney had the highest value with 6.02 while the Başçiftlik Beyazı x Lady Olympia had the lowest value with 3.25 (Table 5). Although the number of tubers is an important feature that affects the yield, the seed value effects are not the same due to the structural heterogeneity, size and other characteristics of the tubers taken from the first generation seeds. Therefore, the deviations in the number of tubers in the first field generation were at the expected level. Although the number of tubers is not an absolute feature during selection, it is also thought that it is not a feature away from attention. Therefore, clones with a low number of tubers were not eliminated much, other characteristics were also examined, however, clones with a high number of tubers were followed closely [14].

Table 5 The average number of tubers (number) per hill of clones belonging to the hybrids in Kazova and Artova locations

Combination	**Number of plant**	**The number of tubers per hill (average)**	**Above average number of clones**
Kazova			
1	273	10.87	118
2	349	8.50	147
3	506	11.70	225
4	615	9.97	280
5	468	11.90	246
6	265	10.61	116
Total	2 476	-	1 132
Average	-	10.59	-
Artova			
1	172	5.59	73
2	313	3.25	109
3	316	3.42	106
4	489	6.02	217
5	332	4.84	130
6	96	4.14	41
Total	1 718	-	676
Average	-	4.54	-

1=Slaney x T5/4, 2= Başçiflik Beyazı x Lady Olympia, 3=A3/15 x Bafana, 4=Başçiflik Beyazı x Slaney, 5=T5/4 x Marfona, 6= T5/4 x Bafana

3.5. Average Tuber Weight

The weight of tubers obtained from each hill was determined by dividing by their number. The mean of tuber weight of the clones examined at the Kazova location was 71.2 g. The Başçiftlik Beyazı x Lady Olympia combination had the highest average tuber weight (92.9 g) while the lowest one was determined in Başçiftlik Beyazı x Slaney combination as 55.7 g (Table 6). There were 1071 clones above the average. The tuber weight mean of the clones of six combinations in Artova location was 41.8 g. The combination with the highest mean tuber weight was A3 / 15 x Bafana with 46.0 g. Moreover, the lowest tuber weight was obtained from the combination of Başçiftlik Beyazı x Slaney (39.6 g). Furthermore, the number of clones above the average in all combinations was 599 (Table 6). The clones, which were decided to be selected in the study, were not chosen according to their unidirectional characteristics, but according to their status of having several properties together. However, in terms of giving an idea and revealing the condition of the first generation, the examination of tuber sizes made the selection easier.

Table 6 Evaluation of average tuber weight (g) of clones belonging to hybrids at Kazova and Artova locations

Combination	**Number of plant**	**Average tuber weight (g)**	**Above average number of clones**
Kazova			
1	273	63.1	120
2	349	92.9	149
3	506	74.0	220
4	615	55.7	264
5	468	74.4	201
6	265	67.4	117
Total	2 476	-	1 071
Average	-	71.2	-
Artova			
1	172	44.2	55
2	313	40.4	110
3	316	46.0	105
4	489	39.6	183
5	332	44.6	121
6	96	36.1	25
Total	1 718	-	599
Average	-	41.8	-
1=Slaney x T5/4, 2= Başçiflik Beyazı x Lady Olympia, 3=A3/15 x Bafana, 4=Başçiflik Beyazı x Slaney, 5=T5/4 x Marfona, 6= T5/4 x Bafana			

3.6. Tuber Yield per Hill

Tubers taken from each hill were weighed and determined in grams. The highest mean tuber yield per hill was obtained from T5 / 4 x Marfona (858.2 g) combination, followed by A3 / 15 x Bafana (819.0 g) (Table 7). The combination with the lowest average was Başçiftlik Beyazı x Slaney (543.2 g). The average tuber yield per hill of 2476 clones examined in the Kazova location was 710.5 g, and the number of clones above the average was 1103. In Artova location, the highest average tuber yield per hill (231.7 g) was obtained from the number 1 combination while the lowest (124.9 g) was obtained from Başçiftlik Beyazı x Lady Olympia. Moreover, the mean of 1718 clones was 177.2 g. (Table 7). Only negative selection is recommended for tuber yield and components in early generations in potato breeding programs. Simultaneous selection should be made for plant vigour, average tuber weight and tuber yield in increasing total yield in potatoes, furthermore, yield and components should be a good guide to improve the value of clones [15].

Table 7 Evaluation of average tuber yield per hill (g) of clones belonging to hybrids in Kazova and Artova locations

Combination	**Number of plant**	**Tuber yield per hill (g)**	**Above average number of clones**
Kazova			
1	273	641.5	120
2	349	736.6	152
3	506	819.0	231
4	615	543.2	263
5	468	858.2	220
6	265	664.5	117
Total	2 476	-	1 103
Average	-	710.5	-
Artova			
1	172	231.7	58
2	313	124.9	104
3	316	142.5	99
4	489	228.6	177
5	332	208.4	118
6	96	127.3	30
Total	1 718	-	586
Average	-	177.2	-
1=Slaney x T5/4, 2= Başçiflik Beyazı x Lady Olympia, 3=A3/15 x Bafana, 4=Başçiflik Beyazı x Slaney, 5=T5/4 x Marfona, 6= T5/4 x Bafana			

3.7. Lateral (eye) and Apical Buds Depth in Tubers

Another characteristic taken into consideration in selection in this study is the distribution of tubers with a high depth of apical bud. Measurements were made with a digital caliper, the means were expressed in mm and classification was made into 5 groups according to the 1-9 scale in the EAPR standards. When the average eye depth of the clones belonging to the combinations numbered 1, 2, 5 and 6 in Table 8 was observed, they were found to have shallow eye depth. Moreover, combinations 3 and 4 had very shallow eye depth. Besides, combinations 1, 2, 4, 5 and 6 were found to have a shallow apical bud. In the clones examined in Artova location, the average eye depth of clones belonging to all combinations was defined as the superficial eye. Moreover, apical bud depth means the protruding bud. In potato tubers, it is not desirable that the apical bud part protrudes excessively. Similarly, it is not preferred that the apical bud part is deep inward. In this case, it can be said that the superficial apical bud depth is appropriate, as in the eyes [14]. Those with very abnormal characteristics were eliminated in later generations, considering other characteristics.

Table 8 Eye and apical bud evaluation of clones belonging to hybrids in Kazova and Artova locations

Combination	Number of plant	Average eye depth	Meaning	Average apical buds depth	Meaning
Kazova					
1	273	1.02	shallow eye	1.10	shallow apical bud
2	349	1.20	shallow eye	1.10	shallow apical bud
3	506	0.90	very shallow eye	0.90	protruding bud
4	615	0.98	very shallow eye	1.03	shallow apical bud
5	468	1.01	shallow eye	1.11	shallow apical bud
6	265	1.05	shallow eye	1.04	shallow apical bud
Total	2 476	1.02	shallow eye	1.04	shallow apical bud
Artova					
1	172	0.66	shallow eye	0.60	protruding bud
2	313	0.65	shallow eye	0.67	protruding bud
3	316	0.73	shallow eye	0.64	protruding bud
4	489	0.86	shallow eye	0.84	protruding bud
5	332	0.76	shallow eye	0.68	protruding bud
6	96	0.71	shallow eye	0.68	protruding bud
Total	1 718	0.72	shallow eye	0.68	protruding bud

1=Slaney x T5/4, 2= Başçiflik Beyazı x Lady Olympia, 3=A3/15 x Bafana, 4=Başçiflik Beyazı x Slaney, 5=T5/4 x Marfona, 6= T5/4 x Bafana

3.8. Skin Smoothness

Skin smoothness in tubers of each clone selected after the harvest was determined according to a scale of 3-7 (3 = Smooth, 5 = Medium, 7 = Rough). Tubers belonging to all clones in Kazova location were examined in terms of skin roughness and 43.7% were found to be smooth, 52.2% medium, and 4.1% rough. In Artova location, 43.3% of the examined clones showed smooth, 52.6% medium and 4.1% rough skin characteristics (Table 9). Skin smoothness is a very important feature in terms of marketability. Although it is determined by the senses of sight and touch, it gives an important idea and is evaluated together with other characteristics. Moreover, it is considered in selection as a characteristic that directly affects the tuber mass quality.

Table 9 Skin roughness values of tubers of hybrids in Kazova and Artova locations (number)

Combination	Number of plant	Smooth (1-2)	%	Medium (3-4)	%	Rough (5)	%
Kazova							
1	273	120	43.8	137	50.4	16	5.8
2	349	164	47.0	158	45.3	27	7.7
3	506	274	54.2	222	43.9	10	2.0
4	615	182	29.6	413	67.2	20	3.3
5	468	245	52.4	211	45.1	12	2.6
6	265	98	37.0	150	56.6	17	6.4
Total	2 477	1 083	-	1 292	-	102	-
Average	-	-	43.7	-	52.2	-	4.1
Artova							
1	172	65	37.8	107	62.2	0	0
2	313	164	52.4	123	39.3	26	8.3
3	316	147	46.5	161	50.9	8	2.5
4	490	163	33.3	318	64.9	9	1.8
5	332	163	49.1	150	45.2	19	5.7
6	96	43	44.8	45	46.9	8	8.3
Total	1 719	745	-	904	-	70	
Average	-	-	43.3	-	52.6	-	4.1

1=Slaney x T5/4, 2= Başçiflik Beyazı x Lady Olympia, 3=A3/15 x Bafana, 4=Başçiflik Beyazı x Slaney, 5=T5/4 x Marfona, 6= T5/4 x Bafana

3.9. Skin and Tuber Flesh Color

After the harvest, the skin and tuber flesh colors of each clone were macroscopically determined. Skin and tuber flesh color is a very important feature in terms of marketability. When the skin colors of tubers belonging to 2477 clones in Kazova location were examined, it was observed that 855 of them (34.5%) were found to be light yellow, 738 (29.8%) were yellow, 869 (35.1%) were dark yellow, and 15 (0.6%) were red spotted (Table 10). Besides, it was determined that 34.6% of the 1719 clones examined in the Artova location had light yellow, 34.1% yellow, 30.2% dark yellow and 1.2% of the clones had red-spotted skin color (Table 10).

As a result of the observations made on the tubers of 2477 clones in Kazova, it was determined that 988 of the clones had light yellow flesh color, while 677 yellow, 279 dark yellow, 341 cream and 192 of them had white flesh color (Table 11). Of the 1719 clones observed in Artova location, 39.2% were found to have light yellow, 28.5% yellow, 10.8% dark yellow, 13.5% cream and 8.1% of them had white flesh color (Table 11). Although tuber flesh color formation is affected by environmental factors related to pigment formation and density, it attracts attention as a feature with high heritability. When examined from this aspect, no elimination process was done among the clones in terms of flesh color. This characteristic should be examined together with other quality characteristics in future generations in selection. Flesh color preference varies according to the intended use. In some cases, varieties with tubers that have quite white flesh color, and in some cases quite yellow, are preferred. Therefore, while classifying the tubers belonging to clones in terms of flesh color in the present study, it was aimed to produce information about the current variation in terms of the flesh color of the tuber.

Table 10 Tuber skin color of hybrids belonging to clones in Kazova and Artova locations (number)

Combination	**Number of plant**	**Light yellow**	**%**	**Yellow**	**%**	**Dark Yellow**	**%**	**Red spotted**	**%**
Kazova									
1	274	120	43.8	50	18.2	101	36.9	3	1.1
2	349	120	34.4	65	18.6	157	45.0	7	2.0
3	506	205	40.5	176	34.8	124	24.5	1	0.2
4	615	171	27.8	203	33.0	238	38.7	3	0.5
5	468	144	30.8	198	42.3	126	26.9	0	0
6	265	95	35.8	46	17.4	123	46.4	1	0.4
Total	2 477	855	-	738	-	869	-	15	-
Average	-	-	34.5	-	29.8	-	35.1	-	0.6
Artova									
1	172	83	48.3	38	22.1	50	29.1	1	0.6
2	313	117	37.4	73	23.3	109	34.8	14	4.5
3	316	135	42.7	125	39.6	56	17.7	0	0
4	490	127	25.9	180	36.7	179	36.5	4	0.8
5	332	99	29.8	144	43.4	89	26.8	0	0
6	96	33	34.4	26	27.1	36	37.5	1	1.0
Total	1 719	594	-	586	-	519	-	20	-
Average	-	-	34.6	-	34.1	-	30.2	-	1.2

1=Slaney x T5/4, 2= Başçiflik Beyazı x Lady Olympia, 3=A3/15 x Bafana, 4=Başçiflik Beyazı x Slaney, 5=T5/4 x Marfona, 6= T5/4 x Bafana

Table 11 Tuber flesh color of hybrids belonging to clones in Kazova and Artova locations (number)

Combination	**Number of plant**	**Light yellow**	**%**	**Yellow**	**%**	**Dark yellow**	**%**	**Cream**	**%**	**White**	**%**
Kazova											
1	274	150	55	49	18	24	9	39	14	12	4
2	349	172	49	87	25	45	13	17	5	28	8
3	506	166	33	235	46	78	15	27	5	0	0
4	615	164	27	40	7	60	10	214	35	137	22
5	468	251	54	161	34	3	1	39	8	14	3
6	265	85	32	105	40	69	26	5	2	1	0.4
Total	2 477	988	-	677	-	279	-	341	-	192	-
Average	-	-	40	-	27	-	11	-	14	-	8
Artova											
1	172	88	51	46	27	8	5	25	15	5	3
2	313	133	43	108	35	46	15	9	3	17	5
3	316	125	40	129	41	45	14	16	5	1	0.3
4	490	139	28	32	7	54	11	159	32	106	21
5	332	165	50	124	37	11	3	22	7	10	3
6	96	23	24	51	53	21	22	1	1	0	0
Total	1 719	673	-	490	-	185	-	232	-	139	-
Average	-	-	39	-	29	-	11	-	14	-	8
1=Slaney x T5/4, 2= Başçiflik Beyazı x Lady Olympia, 3=A3/15 x Bafana, 4=Başçiflik Beyazı x Slaney, 5=T5/4 x Marfona, 6= T5/4 x Bafana											

4. CONCLUSION

It was determined that the clones selected from the six combinations had 40% light yellow, 30.3% yellow, 10.3% dark yellow, 12% cream and 7.4% white tuber flesh color. According to the maturity groups, 2.3% were very early-maturing, 15.9% were early-maturing, 32% were mid-early-maturing, 29.7% were late-maturing, and 20.1% were very late-maturing. While the mean of tuber weight was 11-307 g, tuber yield per hill was 17-2879 g, a number of tubers per hill was 1-38, eye depth was 0.14-3.76 mm (very superficial-very deep), apical bud depth was 0.11-5.33 mm (protruding to very deep). In order to be evaluated in the second clonal generation stage, 103 clones from Slaney x T5 / 4 combination, 147 clones from Başçiftlik Beyazı x Lady Olympia, 200 clones from A3 / 15 x Bafana, 157 clones from Başçiftlik Beyazı x Slaney, 231 clones from T5 / 4 x Marfona, and 80 clones from T5 / 4 x Bafana were selected. As a result of selection in the first clonal generation stage, 918 clones were transferred to the second clonal generation stage. As a matter of fact, this number corresponds to 27.7% of the total material. Therefore, a selection intensity was 72.3%. Of the clones selected locations with different ecological conditions, 772 of them were selected from the Kazova location, while 146 were selected from the Artova location, besides, there were 45 clones selected from both locations.

SIMILARTY RATE: %2

ACKNOWLEDGEMENT

This work was supported by scientific research project of Tokat Gaziosmanpaşa University with the name of the improvement of some local potato (*Solanum tuberosum* L.) variety and promising clones with combination breeding as a doctoral thesis (Project numbers: 2015/51)

REFERENCES

[1] G. Acquaah, Principles of plant genetics and breeding. Library of Congress Cataloging in Publication Data by Graphicraft Limited, p, 978, Hong Kong, 2007.

[2] C. Gebhardt, D. Bellin, H. Henselewski, W. Lehmann, J. Schwarzfischer and J.P.T. Valkonen, Marker assisted combination of major genes for pathogen resistance in potato. Theoretical and Applied Genetics, 112: 1458-1464, 2006.

[3] J.M. Poehlman, and D. Sleper, Breeding Field Crops. 4th ed. Iowa State University Press/Ames, 1995, 419 p, Iowa.

[4] M.F. Paget, Genetic Evaluation Models and Strategies for Potato Variety Selection. A Thesis Submitted in Partial Fulfilment of the Requirements for the Degree of Doctor of Philosophy in the University of Canterbury, 2016.

[5] J. Yuan, A. Murphy, D. Koeyer, M. Lague and B. Bizimungu,. Effectiveness of the field selection parameters on potato yield in atlantic canada. Fredericton Research and Development Centre, Agriculture and Agri-Food Canada, Fredericton, 2018, NB E3B 4Z7, Canada.

[6] .G. Ney, L.R. Terres, G.O. Silva and A.S. Pereira, Expected response to early generation selection for yield and tuber appearance traits in potatoes. Ciências Agrárias, Londrina, v. 37, n. 5, 2849-2858, 2016.

[7] . Yılmaz, N. Kandemir, Y. Yanar and A. Kınay, TÜBİTAK 113O928, Obtaining Hybrid Clones Using Potato Genotypes with Superior Features and Breeding of Some Local Potato Varieties Project Result Report, 2017a.

[8] N. Yakar-Tan, and E. Bilge, General Botanical Book. Istanbul University Science Faculty Publications, Science Faculty Printing house, (2) 2668, 150, Istanbul, 1979.

[9] C.R. Brown, The contribution of traditional potato breeding to scientific potato improvement. Potato Research, 54: 287-300, 2011.

[10] S. Jansky,. Breeding, genetics and cultivar development. In: Singh, J., Kaur, L. (eds) Advances in Potato Chemistry and Technology. Academic Press, 2009, New York, 27–62.

[11] L.A. Ünlenen, Determination of reliable selection criteria for early generation in potato breeding. Mustafa Kemal Univ. Institute of Science, Department of Field Crops. Master Thesis, 2010.

[12] K. Li, B.O. Wayumba, H.S. Choi and L. YoungSeok, Selection for individual traits in the early generations of potato breeding program dedicated to processing chips. Journal of Agriculture and Environmental Sciences, 2016, 5 (2), 15-24.

[13] Pushkarnath. 1976. Potato in sub-tropics. Orient Longman, New Delhi, India, 1995.

[14] G. Yılmaz, Ş. Dökülen and A. Kınay, Seedling Generation with Hybrid Potato Seeds and Production of Seed Tubers for First Clonal Selection. Kahramanmaraş Sütçü İmam Univ. Journal of Natural, 20 (Special Issue), 177-180, 2017.

[15] J. Gopal, Genetic Parameters and Character Association for Clonal Selection in Potato Breeding Programmes. Genetic Parameters and Character Association for Clonal Selection in Potato Breeding Programmes. Agronomie, EDP Sciences, 2006, 19 (6), 531-539.

Eurasian J. Sci. Eng. Tech., 2022; 3(1): 014 - 028

Eurasian Journal of Science Engineering and Technology

Research

FORWARD & INVERSE KINEMATICS SOLUTION OF 6-DOF ROBOTS THOSE HAVE OFFSET & SPHERICAL WRISTS

Serap DİKMENLİ [1,*]

[1] *Altinay Robot Teknolojileri San. ve Tic. A.S., Istanbul Anadolu Yakasi O. S. B. Aydinli Mh. 2. Sanayi Cd. No.22, Tuzla 34956 Istanbul Turkey*

ABSTRACT

One of the critical design decisions that arise during the design of an industrial robot is the function of the joints to be used and their location. Of course, for the designed robot to provide the expected performance, the selection of the motors and gear reducers that will create these joints will primarily affect the determination of these joints. However, both the examination of the existing industrial robots and the fact that the motor and gear reducer information that can be supplied can be easily obtained with today's technology, these joints can be determined quickly as a result of a short investigation. Along with the mechanical design, robot control unit design also has stages that progress in parallel and depend on or affect the mechanical design decisions. One of the most important of these is that especially inverse kinematics calculations can be performed analytically, enabling the robot control unit to make decisions and give commands in real-time.

This article aims to publish the geometric calculation of inverse kinematics of commonly used exampled configuration of 6-DOF industrial robot that has offset and spherical joint along with interactive calculation tables and sheets. There are numerous articles published on the same subject but none of them has provided any verification supplement so far. Thus, it is also aimed to confirm and verify the calculations given in this article by providing convenient tables and sheets and to create a solid foundation for future studies.

Keywords: Inverse kinematics, Forward kinematics, 6-DOF Industrial robot, Spherical wrist, Offset wrist, Analytical solution, Geometric solution.

1. INTRODUCTION

In simple words, kinematics is the study of motion while ignoring the causes of that. Any component of that motion is considered to be rigid. Connections among those components are called joints. There are many joint types but in the end, they all can be expressed with two base joint types; prismatic (sliding) and rotating. Each base joint in the kinematic body defines the DOF[1] of that mechanism. For industrial robots, usually, a rotating joint type is used and if the robot has 6 DOF, it generally means it has 6 rotating joints.

Forward kinematics is to compute the position of end-effector[2] by using specified joint parameters (for rotating joint, it is rotation angle). The solution of any DOF robotic manipulator has to be done in advance and is straightforward theoretical calculation [1], [2], [3], [4], [5], [6], [7], [8], [9]. A method called Denavit Hartenberg[3] convention widely used solution for both Forward & Inverse solutions.

Inverse kinematics is exactly the opposite of forward kinematics, which is to compute joint angles by using a specified end-effector position. The solution is also diverse with numerous approaches. Some most well know theoretical ones [3], [6] are:

Algebraic Solution: Forward kinematics calculations like approach. It has several advantages, such as a) being the most robust solution for real-time calculations, b) it is a straightforward math calculation scheme that may not need DH convention, and c) it is feasible for 3 DOF robot kinematics. On the other hand, it requires an algebraic calculation of the inverse transformation matrix. It introduces the following disadvantages; a) not feasible for almost all 3+ DOF real-life robotics kinematics, b) the solution gets much more complicated when offsets exist and DOFs are increased.

Geometric Solution: Dividing mechanism into several plane geometry problems. When compared with Algebraic, this method also requires extended trigonometric knowledge besides conventional math. Advantages of the solution can be; a) as with algebraic, the solution does not strictly depend on robot structure. b) As in forward kinematics solution, DH parameters representation is also the de-facto standard for the geometric solution. c) the solution is recognized as suitable for real-time

---

[1] Degrees of Freedom

[2] Located at the end of the robotic arm, to interact with the environment

[3] Abbreviated as D-H or DH method and expressed with DH table

* Corresponding author, e-mail: serap.dikmenli@gmail.com (S. Dikmenli)

Recieved: 04.03.2022   Accepted: 05.05.2022
doi: 10.55696/ejset.1082648

calculations. Disadvantages might be; a) avoidance might be possible but, almost all solutions include singularities, b) nonlinearities (multiple solutions) exist due to the use of local coordinates.

Quaternion Solution: This is the newest solution approach that uses an alternative artificial imaginary complex space called Quaternion. Advantages are a) introducing compact formulation; b) reduced number of equations, c) gimbal lock and other singularities are avoided. Drawbacks might be; a) rotations only mechanisms can be handled. b) needs more math to comprehend; c) difficult to interpret and d) less intuitive.

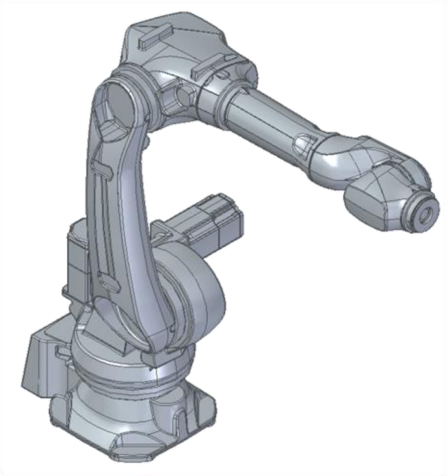

Figure 1. An example robot CAD model

Since our kinematic mechanism includes rotations for each DOF, the quaternion solution seems to be the best fit, but for intuition and easy interpretation, the geometric solution approach will be exercised in this paper. In reality, exampled robot joints are in 3D space, but for the sake of solution simplicity, they all are projected onto a single plane. Shifts between joints are called offsets and the exampled robot has two offsets; the first one is between 1st & 2nd joints and the second one is between 3rd & 4th joints [10]. The 4th, 5th & 6th joints altogether forms spherical wrist [1]. 6-DOF exampled robot will be divided into two 3-DOF mechanisms; the first one compromises 1st, 2nd, and 3rd joints, and the second one compromises spherical wrist joints.

Due to the nature of the inverse kinematics solution, each joint angle could have multiple values. This nature is well documented and investigated in many literature [11], [12]. This article and its supplements will only reveal just the single solution which covers the widest range.

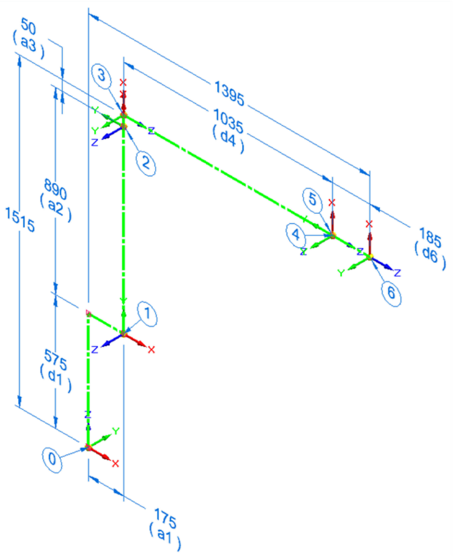

Figure 2. Schematic of robot shown at Figure 1

2. EXAMPLED ROBOT AND ITS SCHEMATIC REPRESENTATION

A 6-DOF industrial robot is chosen. Below find its CAD model (Figure 1), and schematics (Figure 2&3) to be used to define its home position. Initial solution parameters & variables will be extracted from these schematics as well.

3. ROBOT VARIABLES, PARAMETERS & DENAVIT HARTENBERG TABLE

A very commonly used 6-DOF robot has the following variables, parameters, parameters and corresponding Denavit-Hartenberg (DH) table. In this section, these known and unknown will be exposed using the schematics in previous section 2.

3.1 Variables

This 6-DOF robot manipulator has six links and all of them are revolute joints. By changing the angle of these revolute links, a robot can reach and fulfill its function as expected. Therefore, variables of the kinematics system of the introduced robot manipulator are these revolute joint angles and their starting value accepted as 0 (zero) at home position, and it should be bigger than -180° and less than or equal to 180°. In this article and its supplements;

- θ denotes joint angle,
- Subscript n (where n = 1...6) denotes revolute joints,
- A number (1...6) subscript denotes a revolute joint number which is starts from the robot base and goes to the tip,
- Subscript v denotes variable,
- Subscript h denotes home offset joint angle at home position,
- Subscript f denotes joint angle for forward kinematics calculation which includes both variable and home offset part,
- Subscript i denotes joint angle for inverse kinematics calculation which includes both variable and home offset part.

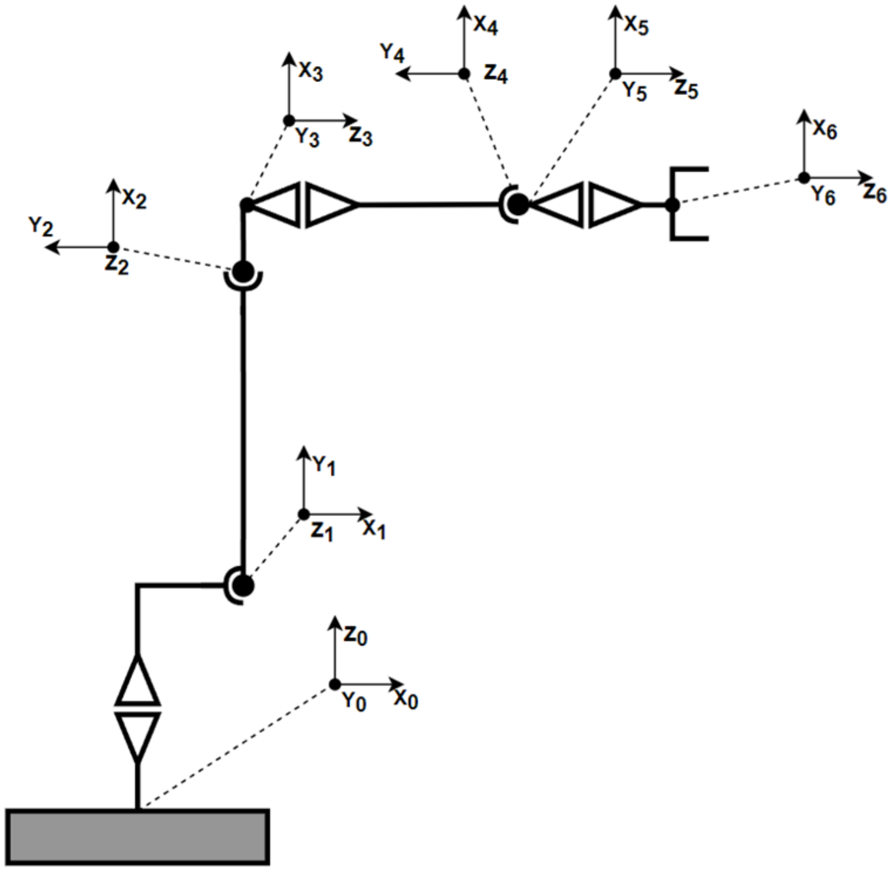

Figure 3: 2D Representation of schematics on Figure 2

3.2 Parameters & Denavit-Hartenberg Table

For the specified home position in schematic Figure 2&3, joint angle offset (θ), twist angle (α), joint offset (d), and joint length (a) should be defining column parameters of the Denavit-Hartenberg (DH) table. Each row of the DH table defines mentioned parameters of each joint. Therefore, we have 6 (row) joints by 4 (column) parameters table. Definition of each parameter is;

θ: Angle about the previous Z, from old X to new X.

α: Angle about new X, from old Z-axis to new Z-axis.

d: Offset distance along the previous Z, from old joint to new joint center.

a: Length along new X, from old joint to new joint center.

In addition to that while placing the local coordinates in Figure 2 following rules apply;

- Z-axis is always the joint axis on which the joint rotates about if it is a rotational joint or moves along if it is a translational joint.
- X-axis must be perpendicular and intersect both new Z & old Z
- Y-axis's placement follows the right-hand rule based on the X & Z axes

By using the above transformation parameters definitions, constraints between axes and the schematic representation of the robot manipulator shown in Figure 2&3, D-H parameters shown in Table 1 can be derived.

The most crucial steps for constructing the D-H table are the placement and orientation of local coordinates so that the complexity of our solution is minimized.

Table 1: D-H Parameters of robot manipulator that's schematics shown in Figure 2&3

	$\theta°_h$	α°	d(mm)	a(mm)
1st Joint	0	90	575	175
2nd Joint	90	0	0	890
3rd Joint	0	90	0	50
4th Joint	0	-90	1035	0
5th Joint	0	90	0	0
6th Joint	0	0	185	0

When variables and parameters merged, the θ, α, d and a values for each joint would be as follows;

$$
\begin{array}{llll}
\theta_{1f} = \theta_{1v} + \theta°_{1h} & \alpha_{1f} = 90° & d_{1f} = 575 & a_{1f} = 175 \\
\theta_{2f} = \theta_{2v} + \theta°_{2h} & \alpha_{2f} = 0° & d_{2f} = 0 & a_{2f} = 890 \\
\theta_{3f} = \theta_{3v} + \theta°_{3h} & \alpha_{3f} = 90° & d_{3f} = 0 & a_{3f} = 50 \\
\theta_{4f} = \theta_{4v} + \theta°_{4h} & \alpha_{4f} = -90° & d_{4f} = 1035 & a_{4f} = 0 \\
\theta_{5f} = \theta_{5v} + \theta°_{5h} & \alpha_{5f} = 90° & d_{5f} = 0 & a_{5f} = 0 \\
\theta_{6f} = \theta_{6v} + \theta°_{6h} & \alpha_{6f} = 0° & d_{6f} = 185 & a_{6f} = 0
\end{array}
$$

In a nutshell, for forward kinematics calculation, the rotation angle at each joint is a variable. There are also 4 D-H parameters for each joint. Therefore, for the 6 DOF mechanism robot, there will be 6 variables and 6x4=24 variables to calculate the end-effector's 3 (x,y,z) cartesian location and 3 angular orientation. For forward kinematics calculation, these six total unknowns always stay constant, whether the mechanism has 2, 3 or 10 joints.

An increased number of DOF on robotics kinematics has almost no effect on forward kinematics, but this cannot be said for inverse kinematics calculation. Depending on the number of additional DOF and each joint's formation, the chosen method may not be feasible.

4. FORWARD KINEMATICS CALCULATION

In 1955, Denavit and Hartenberg proposed a matrix method to construct the coordinate system connected to each link in the robot's joint chains to describe the translational and rotational relationship between adjacent links. This robot kinematics model is based on the D-H coordination system. Transformations between two consecutive joints can be written by substituting the parameters in the parameter table in their corresponding place in the matrix called "A_n", where;

$$A_{nf} = \begin{bmatrix} \cos\theta_{nf} & -\sin\theta_{nf}\cos\alpha_{nf} & \sin\theta_{nf}\sin\alpha_{nf} & a_{nf}\cos\theta_{nf} \\ \sin\theta_{nf} & \cos\theta_{nf}\cos\alpha_{nf} & \cos\theta_{nf}\sin\alpha_{nf} & a_{nf}\sin\theta_{nf} \\ 0 & \sin\alpha_{nf} & \cos\alpha_{nf} & d_{nf} \\ 0 & 0 & 0 & 1 \end{bmatrix}$$

When known joint parameters are put into their corresponding place in this matrix, then the following matrices are obtained for each joint starting from the base (1) to the tip (6);

$$A_{1f} = \begin{bmatrix} \cos\theta_{1f} & 0 & \sin\theta_{1f} & a_{1f}\cos\theta_{1f} \\ \sin\theta_{2f} & 0 & -\cos\theta_{1f} & a_{1f}\sin\theta_{1f} \\ 0 & 1 & 0 & d_{1f} \\ 0 & 0 & 0 & 1 \end{bmatrix}$$

$$A_{2f} = \begin{bmatrix} \cos\theta_{2f} & -\sin\theta_{2f} & 0 & a_{2f}\cos\theta_{2f} \\ \sin\theta_{2f} & \cos\theta_{2f} & 0 & a_{2f}\sin\theta_{2f} \\ 0 & 0 & 1 & 0 \\ 0 & 0 & 0 & 1 \end{bmatrix}$$

$$A_{3f} = \begin{bmatrix} \cos\theta_{3f} & 0 & \sin\theta_{3f} & a_{3f}\cos\theta_{3f} \\ \sin\theta_{3f} & 0 & -\cos\theta_{3f} & a_{3f}\sin\theta_{3f} \\ 0 & 1 & 0 & d_{3f} \\ 0 & 0 & 0 & 1 \end{bmatrix}$$

$$A_{4f} = \begin{bmatrix} \cos\theta_{4f} & 0 & -\sin\theta_{4f} & 0 \\ \sin\theta_{4f} & 0 & \cos\theta_{4f} & 0 \\ 0 & -1 & 0 & d_{4f} \\ 0 & 0 & 0 & 1 \end{bmatrix}$$

$$A_{5f} = \begin{bmatrix} \cos\theta_{5f} & 0 & \sin\theta_{5f} & 0 \\ \sin\theta_{5f} & 0 & -\cos\theta_{5f} & 0 \\ 0 & 1 & 0 & 0 \\ 0 & 0 & 0 & 1 \end{bmatrix}$$

$$A_{6f} = \begin{bmatrix} \cos\theta_{6f} & -\sin\theta_{6f} & 0 & 0 \\ \sin\theta_{6f} & \cos\theta_{6f} & 0 & 0 \\ 0 & 0 & 1 & d_{6f} \\ 0 & 0 & 0 & 1 \end{bmatrix}$$

For abbreviation and simplicity following notation substitutions will be used throughout this article;

$$C_n = \cos\theta_n \qquad S_n = \sin\theta_n$$

$$C_{ab} = C_aC_b - S_aS_b \qquad S_{ab} = C_aS_b + S_aC_b$$

The total transformation matrix from the robot base to the hand is as follows;

$$T_f = A_{1f}A_{2f}A_{3f}A_{4f}A_{5f}A_{6f} = \begin{bmatrix} n_{xf} & o_{xf} & a_{xf} & p_{xf} \\ n_{yf} & o_{yf} & a_{yf} & p_{yf} \\ n_{zf} & o_{zf} & a_{zf} & p_{zf} \\ 0 & 0 & 0 & 1 \end{bmatrix}$$

In which;

$$n_{xf} = C_{6f}\left(C_{5f}\left(C_{1f}C_{23f}C_{4f} + S_{1f}S_{4f}\right) - C_{1f}S_{23f}S_{5f}\right) + S_{6f}(S_{1f}C_{4f} - C_{1f}C_{23f}S_{4f})$$

$$n_{yf} = C_{6f}\left(C_{5f}\left(S_{1f}C_{23f}C_{4f} + C_{1f}S_{4f}\right) - S_{1f}S_{23f}S_{5f}\right) - S_{6f}(C_{1f}C_{4f} + S_{1f}C_{23f}S_{4f})$$

$$n_{zf} = C_{6f}\left(C_{23f}S_{5f} + S_{23f}C_{4f}C_{5f}\right) - S_{23f}S_{4f}S_{6f}$$

$$o_{xf} = S_{6f}\left(C_{1f}S_{23f}S_{5f} - C_{5f}\left(S_{1f}C_{23f}C_{4f} + S_{1f}S_{4f}\right)\right) + C_{6f}(S_{1f}C_{4f} - C_{1f}C_{23f}S_{4f})$$

$$o_{yf} = S_{6f}\left(S_{1f}S_{23f}S_{5f} - C_{5f}\left(S_{1f}C_{23f}C_{4f} + C_{1f}S_{4f}\right)\right) - C_{6f}(C_{1f}C_{4f} + S_{1f}C_{23f}S_{4f})$$

$$o_{zf} = -S_{6f}\left(C_{23f}S_{5f} + S_{23f}C_{4f}C_{5f}\right) - S_{23f}S_{4f}C_{6f}$$

$$a_{xf} = S_{5f}\left(C_{1f}C_{23f}C_{4f} + S_{1f}S_{4f}\right) + C_{1f}S_{23f}C_{5f}$$

$$a_{yf} = S_{5f}\left(S_{1f}C_{23f}C_{4f} - C_{1f}S_{4f}\right) + S_{1f}S_{23f}C_{5f}$$

$$a_{zf} = S_{23f}C_{4f}S_{5f} - C_{23f}C_{5f}$$

$$p_{xf} = d_{6f}(S_{5f}\left(C_{1f}C_{23f}C_{4f} + S_{1f}S_{4f}\right) + C_{1f}S_{23f}C_{5f}) + C_{1f}(a_{1f} + a_{2f}C_{2f} + a_{3f}C_{23f} + d_{4f}S_{23f})$$

$$p_{yf} = d_{6f}(S_{5f}\left(S_{1f}C_{23f}C_{4f} + C_{1f}S_{4f}\right) + S_{1f}S_{23f}C_{5f}) + S_{1f}(a_{1f} + a_{2f}C_{2f} + a_{3f}C_{23f} + d_{4f}S_{23f})$$

$$p_{zf} = a_{2f}S_{2f} + d_{1f} + a_{3f}S_{23f} - d_{4f}C_{23f} + d_{6f}(S_{23f}C_{4f}S_{5f} - C_{23f}C_{5f})$$

The lowest row in the resulting 4x4 transformation matrix is considered as the ineffective row. The top left 3x3 matrix is the rotation matrix, and the 3x1 matrix from top to bottom in the far right column is the translation matrix.

Accordingly, the rotation matrix from the base coordinate system of the robot to the tip of the robot;

$$T_{Rf} = \begin{bmatrix} n_{xf} & o_{xf} & a_{xf} \\ n_{yf} & o_{yf} & a_{yf} \\ n_{zf} & o_{zf} & a_{zf} \end{bmatrix}$$

Where;

[n_{xf} n_{yf} n_{zf}]: the unit vector indicates the direction of the X-axis at the robot end tip to the base coordinate system.

[o_{xf} o_{yf} o_{zf}]: the unit vector indicates the direction of the Y-axis at the robot end tip to the base coordinate system.

[a_{xf} a_{yf} a_{zf}]: the unit vector indicates the direction of the Z-axis at the robot end tip to the base coordinate system.

The unit vector shows the direction of the X, Y and/or Z-axis at the robot tip according to the base coordinate system. However, the expectation is to express all of these in angular form rather than vectorial. Below find how to express tip rotation in *ZY′Z″* Euler and *XY′Z″* Tait-Bryan angles. The matrices used to calculate these angles are available from [13].

ZY′Z″ Euler angles of the robot tip coordinate axis to the base coordinate axis (subscript *e* denotes Euler);

$$Z_{ef} = \text{arctan2}\left(\frac{a_{yf}}{a_{xf}}\right)$$

$$Y'_{ef} = \text{arctan2}\left(\frac{\sqrt{1-a_{zf}^2}}{a_{zf}}\right)$$

$$Z"_{ef} = \text{arctan2}\left(\frac{o_{zf}}{-n_{zf}}\right)$$

XY'Z'' Tait-Bryan angles of the robot tip coordinate axis with respect to the base coordinate axis (subscript *t* denotes Tait-Bryan);

$$X_{tf} = \text{arctan2}\left(\frac{-a_{yf}}{a_{zf}}\right)$$

$$Y'_{tf} = \text{arctan2}\left(\frac{a_{xf}}{\sqrt{1-a_{xf}^2}}\right)$$

$$Z"_{ef} = \text{arctan2}\left(\frac{-o_{xf}}{n_{xf}}\right)$$

The translation matrix from the base coordinate system of the robot to the tip of the robot;

$$T_{Tf} = \begin{bmatrix} p_{xf} \\ p_{yf} \\ p_{zf} \end{bmatrix}$$

The transformation matrix that both includes translation and *ZY'Z''* euler angles can be represented as;

$$T_{ef} = \begin{bmatrix} p_{xf} \\ p_{yf} \\ p_{zf} \\ Z_{ef} \\ Y'_{ef} \\ Z"_{ef} \end{bmatrix}$$

This concludes the forward kinematics calculation. In proceeding inverse kinematics calculations above derived T_{ef} matrix will be taken as input and θ_n joint rotations will be derived.

5. INVERSE KINEMATICS CALCULATION

In the previous session, we have found the end-effector location in cartesian space by inputting joint rotation angles. In real-world robots operates exactly the opposite; the robot controller needs to know the joint angles for a given end-effector's location. This is done by inverse kinematics calculation which will be explained in this session. Input variables of inverse calculation will be the T_{ef} matrix' cell values derived in the previous session, but all subscripts will be changed from *f* to *i* and therefore our input matrix will be;

$$T_{ei} = \begin{bmatrix} p_{xi} \\ p_{yi} \\ p_{zi} \\ Z_{ei} \\ Y'_{ei} \\ Z"_{ei} \end{bmatrix}$$

Rotational angles of each joint will be calculated by using the values in matrix T_{ei}, To do so transformation matrix will be constructed from T_{ei} by going reverse.

The translation part of the transformation matrix is evident; [p_{xi} p_{yi} p_{zi}] vertically forms the top of the rightmost column of the transformation matrix. In order to form the rotation matrix, it will be sufficient to substitute the rotation values given as input in the relevant euler rotation matrix. In reference [13] corresponding rotation matrix calculation for *ZY'Z"* euler angles is already stated. Following substitutions, notations and abbreviations are used to form the rotation matrix from euler angles. As an addition only *i* index is added as a subscript to indicate the inverse calculation;

$$\begin{array}{lll} \alpha_i = Z_{ei} & \beta_i = Y'_{ei} & \gamma_i = Z"_{ei} \\ c_{1i} = \cos(\alpha_i) & c_{2i} = \cos(\beta_i) & c_{3i} = \cos(\gamma_i) \\ s_{1i} = \sin(\alpha_i) & s_{2i} = \sin(\beta_i) & s_{3i} = \sin(\gamma_i) \end{array}$$

Using these abbreviations on the rotation part (3x3 one at upper left) in the transformation matrix;

$$T_i = \begin{bmatrix} c_{1i}c_{2i}c_{3i} - s_{1i}s_{3i} & -c_{3i}s_{1i} - c_{1i}c_{2i}s_{3i} & c_{1i}s_{2i} & p_{xi} \\ c_{1i}s_{3i} - c_{2i}c_{3i}s_{1i} & c_{1i}c_{3i} - c_{2i}s_{1i}s_{3i} & s_{1i}s_{2i} & p_{yi} \\ -c_{3i}s_{2i} & s_{2i}s_{3i} & c_{2i} & p_{zi} \\ 0 & 0 & 0 & 1 \end{bmatrix}$$

It was also shown in forward kinematics calculation, the abbreviated notation of this transformation matrix was as follows;

$$T_f = \begin{bmatrix} n_{xi} & o_{xi} & a_{xi} & p_{xi} \\ n_{yi} & o_{yi} & a_{yi} & p_{yi} \\ n_{zi} & o_{zi} & a_{zi} & p_{zi} \\ 0 & 0 & 0 & 1 \end{bmatrix} = A_{1i}A_{2i}A_{3i}A_{4i}A_{5i}A_{6i}$$

In the matrix, the translation values are already determined, rotational values are as follows;

$$\begin{array}{lll} n_{xi} = c_{1i}c_{2i}c_{3i} - s_{1i}s_{3i} & o_{xi} = -c_{3i}s_{1i} - c_{1i}c_{2i}s_{3i} & a_{xi} = c_{1i}s_{2i} \\ n_{yi} = c_{1i}s_{3i} - c_{2i}c_{3i}s_{1i} & o_{yi} = c_{1i}c_{3i} - c_{2i}s_{1i}s_{3i} & a_{yi} = s_{1i}s_{2i} \\ n_{zi} = -c_{3i}s_{2i} & o_{zi} = s_{2i}s_{3i} & a_{zi} = c_{2i} \end{array}$$

The schematic representation of the robot manipulator with dimensions is shown in **Hata! Başvuru kaynağı bulunamadı.**. The process of finding the angles of each joint of the robot manipulator can be divided into two steps as;

1) find the first three joint angles and then,
2) find the next three spherical joint angles by making use of the first three angles.

In **Hata! Başvuru kaynağı bulunamadı.**, a geometric explanation brought to finding the first joint angle θ_{1i}.

$$P_{04} = P_{06} - P_{46} \; where, P_{06} = \begin{bmatrix} p_{xi} \\ p_{yi} \\ p_{zi} \end{bmatrix}, \; P_{46} = d_{6i} \begin{bmatrix} a_{xi} \\ a_{yi} \\ a_{zi} \end{bmatrix}$$

$$P_{04} = \begin{bmatrix} x_{05} \\ y_{05} \\ z_{05} \end{bmatrix} = \begin{bmatrix} p_{xi} \\ p_{yi} \\ p_{zi} \end{bmatrix} - d_{6i} \begin{bmatrix} a_{xi} \\ a_{yi} \\ a_{zi} \end{bmatrix} = \begin{bmatrix} p_{xi} - d_{6i}a_{xi} \\ p_{yi} - d_{6i}a_{yi} \\ p_{zi} - d_{6i}a_{zi} \end{bmatrix}$$

Thus;

$$\theta_{1i} = \theta_{1v} = \text{arctan2}\left(\frac{p_{yi}-d_{6i}a_{yi}}{p_{xi}-d_{6i}a_{xi}}\right) \tag{1}$$

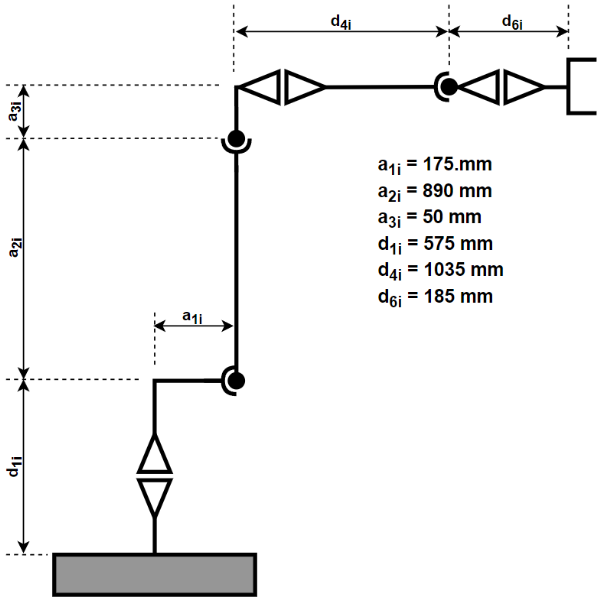

Figure 4: 2D Representation of robot manipulator with key dimensions

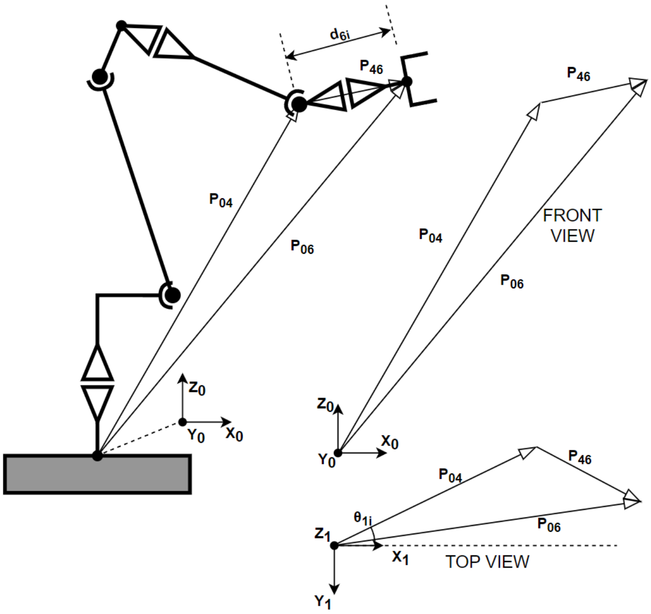

Figure 5: Graphical expression to derive θ_{1i}.

Again using the geometric solution shown in Figure 1 and cosine law (Figure 2), θ_{3i} can be derived as follows;

$$P_{01} = \begin{bmatrix} x_{01} \\ y_{01} \\ z_{01} \end{bmatrix} = \begin{bmatrix} a_{1i}C_{1i} \\ a_{1i}S_{1i} \\ d_{1i} \end{bmatrix}, P_{04} = \begin{bmatrix} x_{04} \\ y_{04} \\ z_{04} \end{bmatrix} = \begin{bmatrix} p_{xi} - d_{6i}a_{xi} \\ p_{yi} - d_{6i}a_{yi} \\ p_{zi} - d_{6i}a_{zi} \end{bmatrix}$$

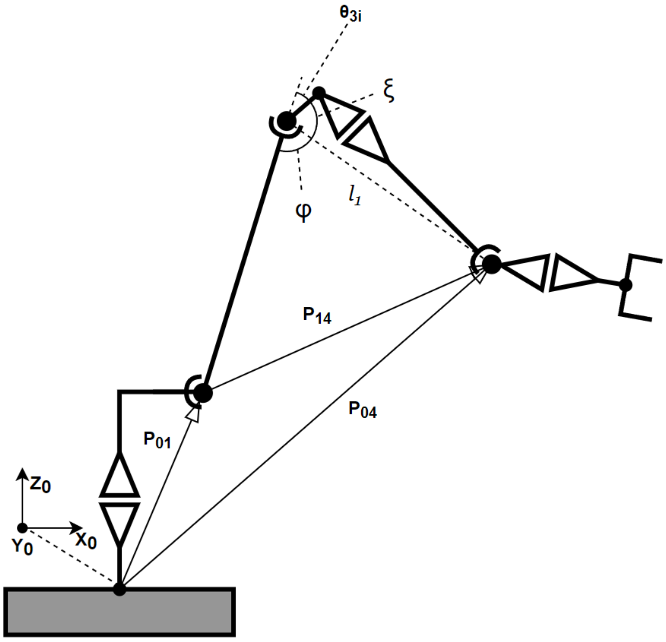

Figure 1: Graphical expression to derive θ_{3i}

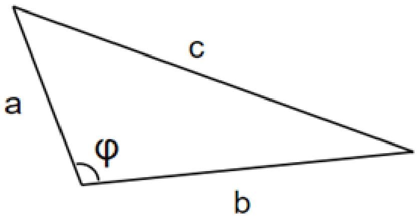

$$\cos(\varphi) = \frac{a^2 + b^2 - c^2}{2 . a . b}$$

Figure 2: Law of cosine

Thus;

$$P_{14} = \begin{bmatrix} x_{14} \\ y_{14} \\ z_{14} \end{bmatrix} = P_{04} - P_{01} = \begin{bmatrix} p_{xi} - d_{6i}a_{xi} - a_{1i}C_{1i} \\ p_{yi} - d_{6i}a_{yi} - a_{1i}S_{1i} \\ p_{zi} - d_{6i}a_{zi} - d_{1i} \end{bmatrix}$$

and,

$$P_{14L} = \sqrt{\mid P_{14}^{T} \cdot P_{14} \mid}\,, \qquad l_1 = \sqrt{a_{3i}^2 + d_{4i}^2}$$

Where *L* subscript represents the length of the corresponding vector. Applying cosine law and well known trigonometric formula;

$$\varphi = \arccos\left(\frac{l_1^2 + a_{2i}^2 - P_{14L}}{2 l_1 a_2}\right), \qquad \zeta = \operatorname{arctan2}\left(\frac{d_{4i}}{a_{3i}}\right)$$

Therefore;

$$\theta_{3i} = \theta_{3v} = \varphi - \zeta - \pi \tag{2}$$

Once again using the geometric solution described in Figure 3, cosine law (Figure 2), and well know trigonometric formula θ_{2i} can be derived as;

$$P_{14} = \begin{bmatrix} x_{14} \\ y_{14} \\ z_{14} \end{bmatrix} = \begin{bmatrix} p_{xi} - d_{6i} a_{xi} - a_{1i} C_{1i} \\ p_{yi} - d_{6i} a_{yi} - a_{1i} S_{1i} \\ p_{zi} - d_{6i} a_{zi} - d_{1i} \end{bmatrix}$$

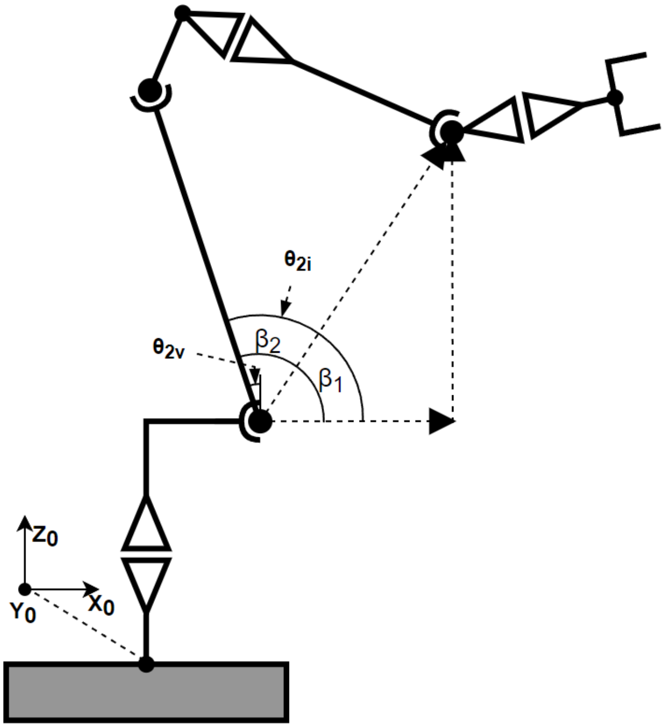

Figure 3: Graphical expression to derive θ_{2i}

From the above equation, β_1 and β_2 can be found as;

$$\beta_1 = \operatorname{arctan2}\left(\frac{z_{14}}{\sqrt{x_{14}^2 + y_{14}^2}}\right)$$

$$\beta_2 = \arccos\left(\frac{a_{2i}^2 - P_{14L}^2 - l_1^2}{2a_2 P_{14L}}\right)$$

From geometry;

$$\theta_{2\mathrm{i}} = \theta_{2\mathrm{v}} + \frac{\pi}{2} = \beta_1 + \beta_2 \tag{3}$$

The first phase of the inverse calculation is finalized by finding the first three joint rotational angles. The second and the last phase to find the rest of the three joints that make up the spherical wrist will be solved geometrically.

To calculate θ_{5i} we will assume $\theta_{4i} = 0$, or better, the absence of the 4th joint. Then the angle between the rotation vectors (R_z) will give us θ_{5i}.
Before doing that some equality declaration has to be stated to be the base for further calculations;

$$A_{1i} = \begin{bmatrix} C_{1i} & 0 & S_{1i} & a_{1i}C_{1i} \\ S_{1i} & 0 & -C_{1i} & a_{1i}S_{1i} \\ 0 & 1 & 0 & d_{1i} \\ 0 & 0 & 0 & 1 \end{bmatrix}$$

$$A_{2i} = \begin{bmatrix} C_{2i} & -S_{2i} & 0 & a_{2i}C_{2i} \\ S_{2i} & C_{2i} & 0 & a_{2f}S_{2i} \\ 0 & 0 & 1 & 0 \\ 0 & 0 & 0 & 1 \end{bmatrix}$$

$$A_{3i} = \begin{bmatrix} C_{3i} & 0 & S_{3i} & a_{3i}C_{3i} \\ S_{3i} & 0 & -C_{3i} & a_{3i}S_{3i} \\ 0 & 1 & 0 & 0 \\ 0 & 0 & 0 & 1 \end{bmatrix}$$

The following is also known;

$$C_{12} = C_1C_2 - S_1S_2 \qquad S_{12} = C_1S_2 + S_1C_2$$

For the sake of finding the 5th joint angle, it is assumed that the 4th joint is absent. 1st to 3rd joint transformation matrix will be also considered to be 1st to 4th joint transformation matrix. Since all first three joint angles know, A_{13} and consequently A_{14} can be derived;

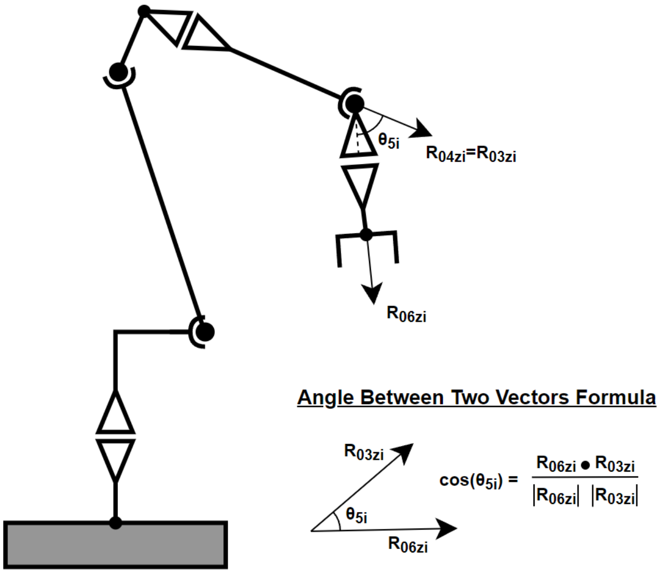

Figure 4: Graphical expression to derive θ_{5i}

$$A_{14i} = A_{13i} = A_{1i} \cdot A_{2i} \cdot A_{3i} = \begin{bmatrix} C_{1i}C_{23i} & S_{1i} & C_{1i}S_{23i} & C_{1i}(a_{1i} + a_{2i}C_{2i} + a_{3i}C_{23i}) \\ S_{1i}C_{23i} & -C_{1i} & S_{1i}S_{23i} & S_{1i}(a_{1i} + a_{2i}C_{2i} + a_{3i}C_{23i}) \\ S_{23i} & 0 & -C_{23i} & a_{2i}S_{2i} + d_{1i} + a_{3i}S_{23i} \\ 0 & 0 & 0 & 1 \end{bmatrix}$$

From input values, the rotation vector about *z* (R_{6zi}) is known. From the above-mentioned assumption that is R_{4zi} is equal to R_{3zi}, R_{4zi} is known. Then the angle between two vectors formula as shown on Figure 4 will be applied to find the θ_{5i} unknown.

$$R_{6zi} = \begin{bmatrix} a_{xi} \\ a_{yi} \\ a_{zi} \end{bmatrix}, \qquad R_{3zi} = R_{4zi} = \begin{bmatrix} C_{1i}S_{23i} \\ S_{1i}S_{23i} \\ -C_{23i} \end{bmatrix}$$

Since both R_{6zi} and R_{4zi} are unit vectors, matrix multiplication will give the cosine of the angle between two vectors;

$$\theta_{5i} = \theta_{5v} = \arccos\left(\overrightarrow{R_{6zi}} \cdot \overrightarrow{R_{3zi}}\right) \tag{4}$$

4th and 6th joints are only the joint angles left which are unknown to us.

Since both A_{13i} & A_{16i} are known, we can derive A_{46i} as follows;

$$A_{46i} = A_{13i}^{-1} \cdot A_{16i} = \begin{bmatrix} I_x & J_x & K_x & L_x \\ I_y & J_y & K_y & L_y \\ I_z & J_z & K_z & L_z \\ 0 & 0 & 0 & 1 \end{bmatrix}$$

Where all *I, J, K*, and *L* are calculated and known values.

On the other hand, the A_{46i} matrix can also be derived symbolically by multiplying the following matrices;

$$A_{46i} = A_{4i} \cdot A_{5i} \cdot A_{6i} = \begin{bmatrix} E_x & F_x & G_x & H_x \\ E_y & F_y & G_y & H_y \\ E_z & F_z & G_z & H_z \\ 0 & 0 & 0 & 1 \end{bmatrix}$$

Where;

$$E_x = C_{4i}C_{5i}C_{6i} - S_{4i}S_{6i} \quad F_x = -(C_{4i}C_{5i}S_{6i} + S_{4i}C_{6i}) \quad G_x = C_{4i}S_{5i} \quad H_x = C_{4i}S_{5i}d_{6i}$$

$$E_y = S_{4i}C_{5i}C_{6i} + C_{4i}S_{6i} \quad F_y = -S_{4i}C_{5i}S_{6i} + C_{4i}C_{6i} \quad G_y = S_{4i}S_{5i} \quad H_y = S_{4i}S_{5i}d_{6i}$$

$$E_z = -S_{5i}C_{6i} \quad F_z = S_{5i}S_{6i} \quad G_z = C_{5i} \quad H_z = C_{5i}d_{6i} + d_{4i}$$

From the previous symbolic matrix, it can be easily noticed that the inverse tangent (*arctan2*) of matrix elements 2.3 (H_y) over 1.3 (H_x) gives θ_{4i} and the inverse tangent of elements 3.2 (F_z) over 3.1 (E_z) gives θ_{6i}.

$$\theta_{4i} = \theta_{4v} = \text{arctan2}\left(\frac{H_y}{H_x}\right) = \text{arctan2}\left(\frac{L_y}{L_x}\right) \tag{5}$$

and,

$$\theta_{6i} = \theta_{6v} = \text{arctan2}\left(\frac{F_z}{E_z}\right) = \text{arctan2}\left(\frac{J_z}{I_z}\right) \tag{6}$$

Thus, all unknown angles for 6 joints are found by using the geometric solution approach.

6. CONCLUSION

Open source coding for forward and inverse kinematics solution might be obtained in low or high-level languages, but using the code might be painful for many reasons such as;

- compiler may need to be purchased
- coding language might be learned
- debugging is hard if there is any bug in the code
- coding should be fully understood before adapting or extending

These difficulties most likely lead to moving away from those who want to dive into robotics and progress at a rapid pace. With this article and provided supplemental calculation sheets (SMath & Excel) [14], a solid foundation is thought to be established for understanding both forward & especially inverse kinematics solutions.

For both easy understanding and solution simplicity, just a single solution is introduced. Inverse kinematics solution covers the widest but limited range. For instance, the 5th joint cannot derive to negative rotational angles. Angles on the 1st and 2nd quadrants of the unit circle are covered because this joint angle is derived from the *arccos* function.

Applicability of the chosen inverse calculation approach can be exercised with supplied interactive table sheet. Compared to quaternion, it is not a singularity-free solution. In case these singularities are in the robot's working space, additional algorithms may be needed to resolve them.

If desired, other inverse kinematics solution variants can be easily developed. Previously mentioned [11], [12] references are a great starting point.

SIMILARTY RATE: 10%

REFERENCES

[1] S. Asif, and P. Webb, "Kinematics Analysis of 6-DoF Articulated Robot with Spherical Wrist", *Hindawi Mathematical Problems in Engineering Volume 2021*, Article ID 6647035, 11 pages, 2020. [Online] Available: https://doi.org/10.1155/2021/6647035 [Accessed: May 7, 2022]

[2] Kepçeler, T. "Esnek Robot Kollarda Optimum Hareket Sentezi", PhD. Thesis, *Graduate School of Science & Engineering*, Yildiz Technical University, Istanbul, Turkey, 1999, p. 20-32

[3] S. Cubero, *Industrial Robotics: Theory, Modelling and Control*, plV pro literatur Verlag Robert Mayer-Scholz, DOI:10.5772/44, ISBN 3-86611-285-8, pp. 117-185, 2012.

[4] M. Dahari, J. D. Tan, "Forward and Inverse Kinematics Model for Robotic Welding Process Using KR-16KS KUKA Robot", *2011 4th International Conference on Modeling, Simulation and Applied Optimization*, IEEE, ICMSAO 2011, DOI: 10.1109/ICMSAO.2011.5775598, 2011.

[5] W. Guojun, X. Linhong, and H. Fulun, "Offline kinematics simulation of 6-DOF welding robot", *2009 International Conference on Measuring Technology and Mechatronics Automation*, ICMTMA 2009, vol. 2, DOI: 10.1109/ICMTMA.2009.608, 2009.

[6] E. Sariyildiz, E. Cakiray, and H. Temeltas, "A Comparative Study of Three Inverse Kinematic Methods of Serial Industrial Robot Manipulators in the Screw Theory Framework", *International Journal of Advanced Robotic Systems*, issue 5, vol. 8, DOI: 10.5772/45696, ISSN: 17298814, 2011.

[7] J. J. Craig, *Introduction to Robotics: Mechanics and Control*, 3rd Edition, Pearson Education Limited, ISBN 10: 1-292-04004-1, 2004, pp. 19-135.

[8] M. E. Kütük, M. T. Das, and L. C. Dülger, "Forward and Inverse Kinematics Analysis of Denso Robot", *Proceedings of the International Symposium of Mechanism and Machine Science, 2017*, AzC IFToMM-Azerbaijan Technical University, issue September, vol. 11, 2017.

[9] A. Khatamian, "Solving Kinematics Problems of a 6-DOF Robot Manipulator", *Int'l Conf. Scientific Computing*, CSC, 2015, pp. 228-233

[10] S. Kucuk, and Z. Birgul, "Inverse Kinematics Solutions for Industrial Robot Manipulators with Offset Wrists", *Applied Mathematical Modelling*, vol. 38, issue 7-8, DOI:10.1016/j.apm.2013.10.014, ISSN: 0307904X, 2014. [Online] Available: http://dx.doi.org/10.1016/j.apm.2013.10.014 [Accessed: May 7, 2022].

[11] P. Masajedi, K.H. Shirazi, and A. Ghanbarzadeh, "Verification of bee algorithm based path planning for a 6DOF manipulator using ADAMS", *Journal of Vibroengineering*, Vol. 15, Issue 2, 2013, pp. 805-815 [Online Document], Available: JVE Journals, https://www.extrica.com/article/14551 [Accessed: Feb. 24, 2022].

[12] L. Wu, X. Yang, K. Chen, and H. Ren, "A Minimal POE-Based Model for Robotic Kinematic Calibration with only Position Measurements", *IEEE Transactions on Automation Science and Engineering*, issue 2, vol. 12, DOI: 10.1109/TASE.2014.2328652, ISSN: 15455955, 2015.

[13] Wikipedia The Free Encyclopedia, "Euler Angles" (), *Wikipedia The Free Encyclopedia*, [Online]. Available: https://en.wikipedia.org/wiki/Euler_angles [Accessed: Dec. 19, 2021].

[14] S. Dikmenli, "Forward & Inverse Kinematics Solution of 6-DOF Robots Those Have Offset & Spherical Wrists - Supplementary Data", *Mendeley Data*, V1, doi: 10.17632/nfbjphjvkn.1, 2022. [Online]. Available: http://dx.doi.org/10.17632/nfbjphjvkn.1 [Accessed: May 7, 2022]

Eurasian Journal of Science Engineering and Technology

Research

PREPARATION OF CZTS THIN FILM EMPLOYING RAPID THERMAL PROCESSING METHOD

Mehmet Ali OLĞAR[1,*], Yavuz ATASOY[2]

[1]*Niğde Ömer Halisdemir University, Department of Physics, 51240, Niğde*
[2]*Niğde Ömer Halisdemir University, Niğde Zübeyde Hanım Health Services Vocational High School, 51240 Niğde*
[1,2] *Niğde Ömer Halisdemir University, Nanotechnology Application and Research Center, 51240 Niğde*

ABSTRACT

CZTS thin film was fabricated by sulfurization process of deposited thin films on Mo coated glass substrates. Cu, Zn, and Sn thin film layers were deposited sequentially to form Glass/Mo/CuSn/Zn/Cu. The CuSn layer in the stacked structure was formed by annealing process in the sputtering chamber after sequential deposition of Cu and Sn, respectively. The sulfurization process was performed by rapid thermal processing method (RTP) so as to obtain kesterite CZTS structure. The obtained CZTS thin film was analyzed using several characterization methods such as EDX, XRD, Raman spectroscopy, SEM and PL measurements. The EDX measurements showed that elemental loss was not observed after the annealing process in sulfur atmosphere. The fabricated CZTS thin film showed Cu stoichiometric and Zn rich composition. The XRD pattern of annealed sample revealed formation of kesterite CZTS structure. The Raman spectra of the sample proved formation of kesterite CZTS structure. In addition, some CTS phases were detected in the structure by Raman spectroscopy. Polycrystalline surface microstructure was seen in SEM surface measurement. The room temperature PL measurement exhibited a transition around at 1.39 eV that is very close to band gap of kesterite CZTS structure. Overall, with this study, it has been shown that the CZTS thin film structure can be easily produced using the RTP method with very high heating rate.

Keywords: CZTS, RTP, Sputtering, Kesterite, Thin film

1. INTRODUCTION

Cu_2ZnSnS_4 (CZTS) thin film semiconducting materials gained huge interest in thin film photovoltaic (PV) industry recently. Although the CdTe and Cu (In, Ga)Se_2 (CIGS) based thin films are the most common materials studied in this area due to their high conversion efficiencies, the scarce nature of In and Ga, and toxic nature of Cd cause a reduction in further improvement of such kind of solar materials [1, 2]. Therefore, the CZTS is emerged as an alternative material thanks to the fact that it contains plentiful raw materials, 1.4-1.5 eV direct optical band gap, convenient absorption coefficient, and p-type conductivity [3]. Such optical and electrical characteristics of CZTS thin film make this material favorable for photovoltaic applications.

The CZTS samples commonly fabricated by two stage process [4]. In this first stage, deposition of precursor layers (Cu, Sn, and Zn) are performed using either vacuum-based or solution-based techniques. The most common used vacuum and solution-based techniques are DC and RF magnetron sputtering [5, 6], thermal and e-beam evaporation [7, 8], pulsed laser deposition [9], spin coating [10], electrodeposition [11], spray pyrolysis etc. [12]. The sputtering method is the more preferable technique in preparation of CZTS thin films because it ensures pure, uniform, more controllable film thickness, and more suitable for large scale production.

The CZTS solar cell has a theoretical limit above the 30% conversion efficiency [13]. However, the record conversion efficiency is 13.0 % [14]. Many different approaches are being tried to increase the cell efficiency and converge to highest CZTS based solar cell efficiency. Foremost among these approaches is optimizing the growth parameters of the CZTS films. For example, employing various stacking order of precursor layers [15], preparing the CZTS compound in different chemical composition [16], and optimizing the sulfurization parameters [17, 18].

The sulfurization process is generally carried out by two different procedures that are conventional thermal processing (CTP) and rapid thermal processing (RTP) methods [19, 20]. The latter method ensures that reaching to reaction temperature is more quickly (up to 50 °C/s), minimizing the decomposition processes, and reducing production time and cost.

In this work, CZTS semiconductor compound was prepared by annealing of Glass/Mo/CuSn/Zn/Cu stacked film prepared by sputtering system using RTP method in sulfur atmosphere. The Glass/Mo/CuSn/Zn/Cu stack was selected for preparation of CZTS thin films since more promising films were obtained using this stack by our research group [21]. Furthermore, the CuSn structure was formed intentionally in the sputtering chamber so as to prevent Sn-loss in the sample. It is well known that SnS is

---

* Corresponding author, e-mail: mehmetaliolgar@ohu.edu.tr (M. A. Olğar)

Recieved: 05.04.2022 Accepted: 18.04.2022
doi: 10.55696/ejset.1098850

a volatile phase due to its high vapor pressure. The CuSn alloy may limit formation of SnS phase and thus prevents the formation of decomposition reactions.

The prepared CZTS sample was characterized using several techniques, such as energy dispersive X-ray spectroscopy (EDX), X-ray diffractometer (XRD), Raman spectroscopy, scanning electron microscopy (SEM), and photoluminescence (PL).

2. MATERIAL AND METHOD

The Glass/Mo/CuSn/Zn/Cu stacked film was produced by sputtering method. High purity Mo (4N), Cu (5N), Zn (4N) and Sn (4N) targets were used for the fabrication of stacked precursor film. Prior to deposition process, the glass substrates were cleaned using the standard cleaning procedure. It was cleaned first in acetone, then isopropanol, and finally in distilled water solutions in ultrasonic cleaner. The cleaned glass sheets were dried with nitrogen gas and placed in the sputtering system for the deposition process. The Mo layer (250 nm) and Cu layers were deposited using DC power source, Zn and Sn layers were coated using RF power supply. After the glass substrate was coated with Cu and then Sn, the temperature of sample holder was set to 200 °C, and CuSn alloy was obtained by annealing this structure for 5 minutes in the sputtering chamber. Just above this structure, the Zn and approximately 30% of the total thickness of Cu were deposited sequentially to obtain complete Glass/Mo/CuSn/Zn/Cu stacked film. The thickness of Cu (175 nm), Zn (165 nm) and Sn (230 nm) was measured by profilometer.

After the precursor layer pulled out from the sputtering system, it was placed in the graphite box with 50 mg of high purity sulfur pieces and it was placed in the RTP system. The sulfurization process was carried out at 550 °C temperature using the highest heating rate (5 °C/s) allowed by our system, using a dwell time of 1 minute. The sulfurization temperature and time were selected subject to our previous reported studies [15, 22].

The chemical composition of the produced CZTS sample was analyzed by EDX, the structural properties were characterized by XRD and Raman spectroscopy (633 nm), the surface morphology was investigated by SEM, and the optical properties were determined by room temperature PL measurements.

3. RESULTS AND DISCUSSION

The chemical composition of precursor and CZTS thin films was characterized by EDX measurement. The EDX spectrum of CZTS thin film was given in Fig. 1.

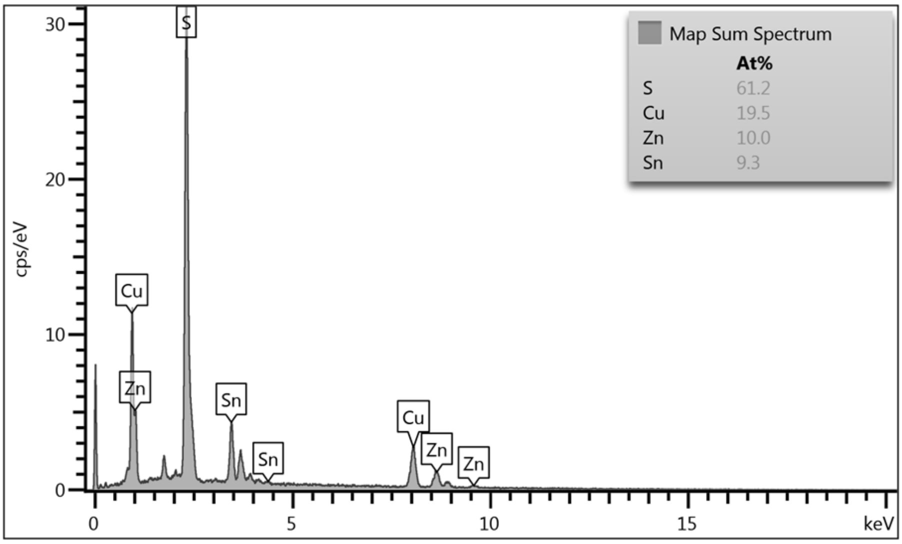

Figure 1. EDX spectrum of CZTS thin film.

The EDX analyses performed by map measurement (~150 µm x 150 µm) since a point measurement may not reflect actual composition of the films due to inhomogeneous elemental distribution. The chemical composition of precursor and CZTS thin film were presented in Table 1. As displayed in the table, Cu/(Zn+Sn) and Zn/Sn ratio of the samples showed similar values. The Cu/(Zn+Sn) and Zn/Sn atomic ratios are ~1.01 and 1.08, respectively. These results showed that the sulfurization process did not cause any elemental loss in the sample. The SnS phase is a volatile phase since it has high vapor pressure and it causes

Sn-loss in the samples when unsuitable sulfurization conditions are applied to the precursor films [23]. According to our EDX results, it can be easily said that the sulfurization process was carried out successfully.

Table 1. Chemical composition of precursor and CZTS thin film.

Sample	**Atomic percentage %)**				**Atomic Ratio**		
	Cu	**Zn**	**Sn**	**S**	**Cu/(Zn+Sn)**	**Zn/Sn**	**S/Metal**
Precursor	50.5	25.7	23.8	-	1.02	1.08	-
CZTS	19.5	10.0	9.3	61.2	1.01	1.08	1.58

The crystal structure of CZTS thin film was characterized by XRD measurement. XRD plot of CZTS film was presented in Fig. 2.

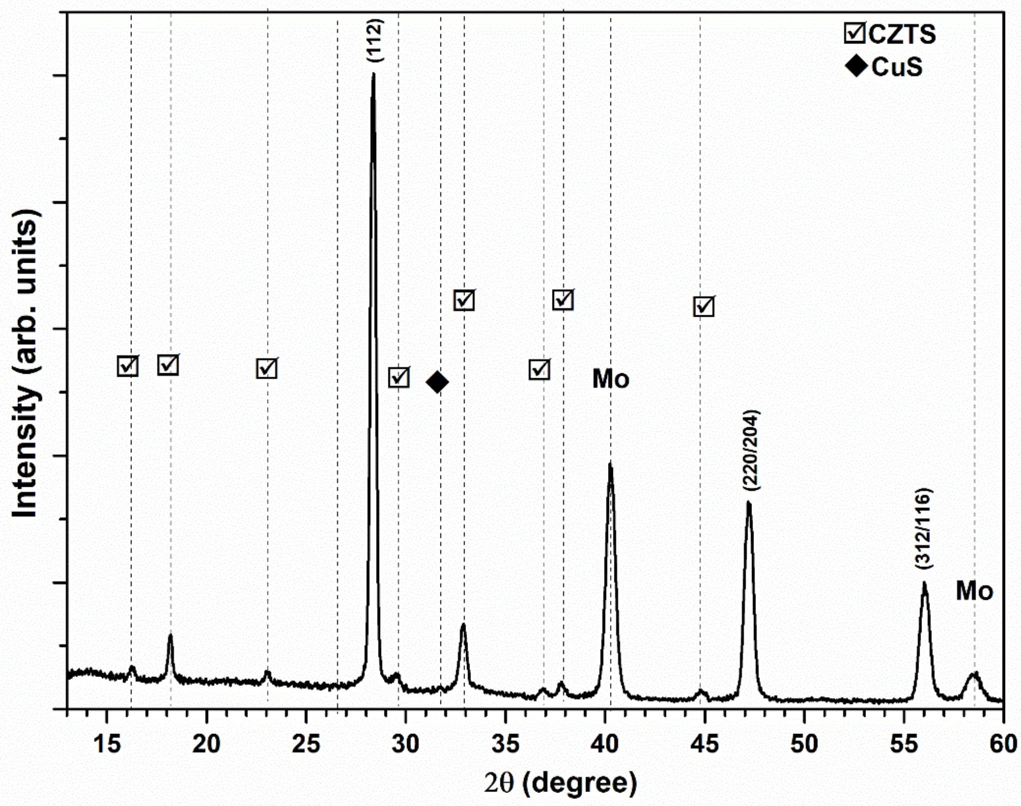

Figure 2. XRD pattern of CZTS sample prepared in this study.

As seen in the figure, the XRD pattern is dominated by (112), (220/204), and (312/116) diffraction planes of the kesterite CZTS phase (JCPDS 26-0575). The other peaks of the same phase are shown in the figure. The diffraction peaks from Mo back contact layer are also shown in the figure (JCPDS 42-1120). A very low intensity peak at around 2θ=31.70° was detected. This peak can be attributed to occurrence of CuS phase (JCPDS 03-065-3556). This phase can be removed from the surface of the sample by KCN etching process [24]. Therefore, it is possible to obtain almost pure kesterite CZTS sample by this simple etching process. Overall, except for minor peak of CuS, XRD pattern of CZTS sample revealed almost pure kesterite CZTS.

The Raman spectroscopy technique was used to prove occurrence of kesterite CZTS phase because Cu_2SnS_3 (CTS) and ZnS phases have resembling XRD patterns compared to CZTS structure [16].

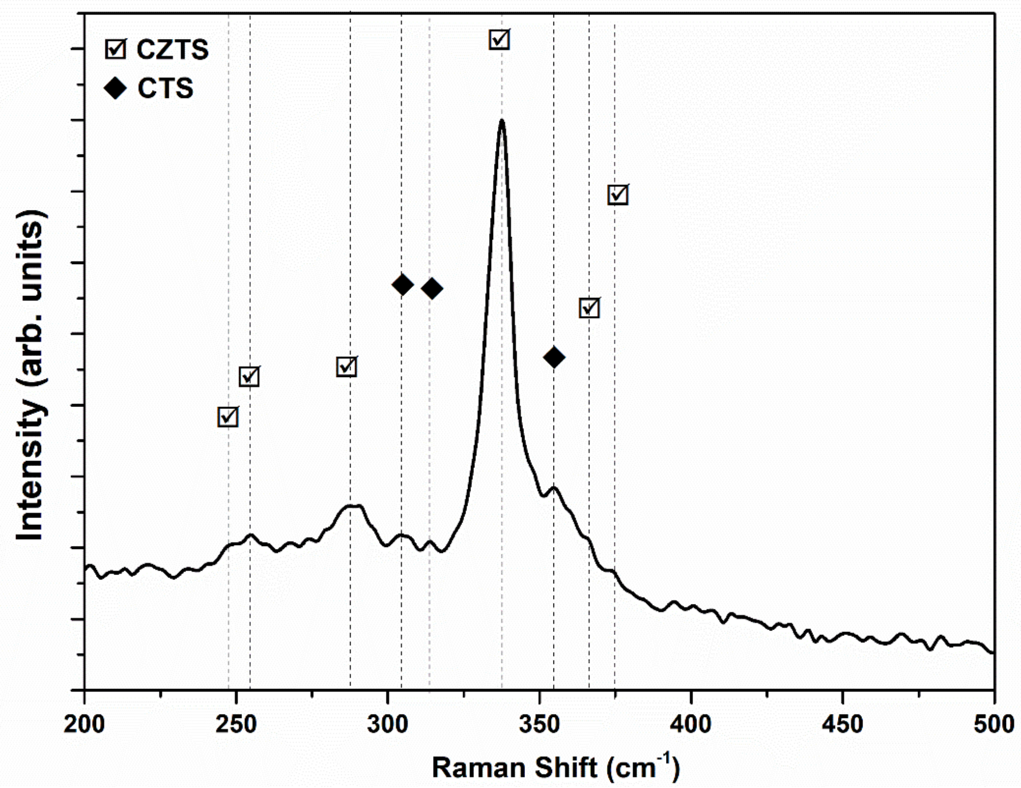

Figure 3. Raman spectrum of CZTS thin film.

As we can see from the figure that a strong peak at around 338 cm^{-1} was detected. It is attributed to vibration mode of kesterite CZTS phase [25]. The other CZTS peaks were marked in the figure. In addition to kesterite CZTS phase, some minor peaks at around 303, 314 and 355 cm^{-1} were detected [26]. These peaks can be ascribed to constitution of CTS phase that is not distinguished by XRD technique. Formation of this phase can be explained by short sulfurization time that may be not enough for obtaining complete CZTS structure [27].

The morphology of precursor and CZTS sample was investigated by SEM technique. The SEM microstructure of the films was displayed in Figure 4. As displayed in the figure, precursor film showed homogenous and dense surface microstructure. After the sulfurization process, the CZTS sample revealed dense and large-grained polycrystalline surface microstructure that is desired situation for solar cell application since small grains gives rise to formation of more grain boundaries and such formation act as recombination centers in the cell [28]. The grain size was found to be on the order of 1 µm.

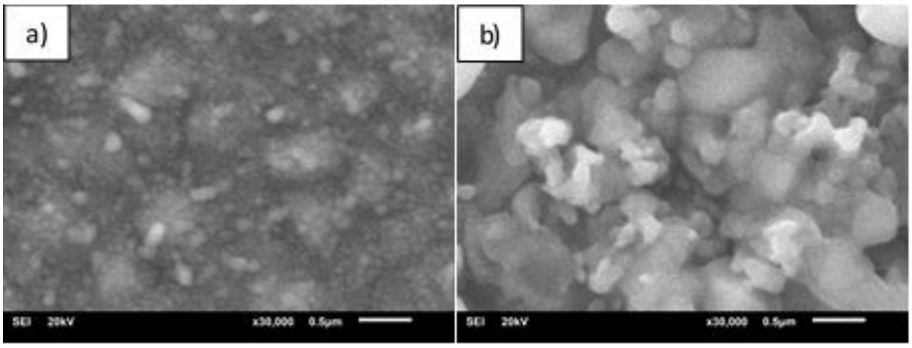

Figure 4. SEM surface image of a) precursor, and b) CZTS thin films.

The photoluminescence (PL) measurement was performed at room temperature and it was presented in Figure 5. As can be seen in the figure, a broad band peaked at around 1.39 eV. It was seen that the obtained value is in good agreement with the reported literature [22, 29]. Considering that the forbidden band gap energy of the kesterite CZTS phase is around 1.4-1.5 eV, it can be seen that the obtained value is very close to this range [30].

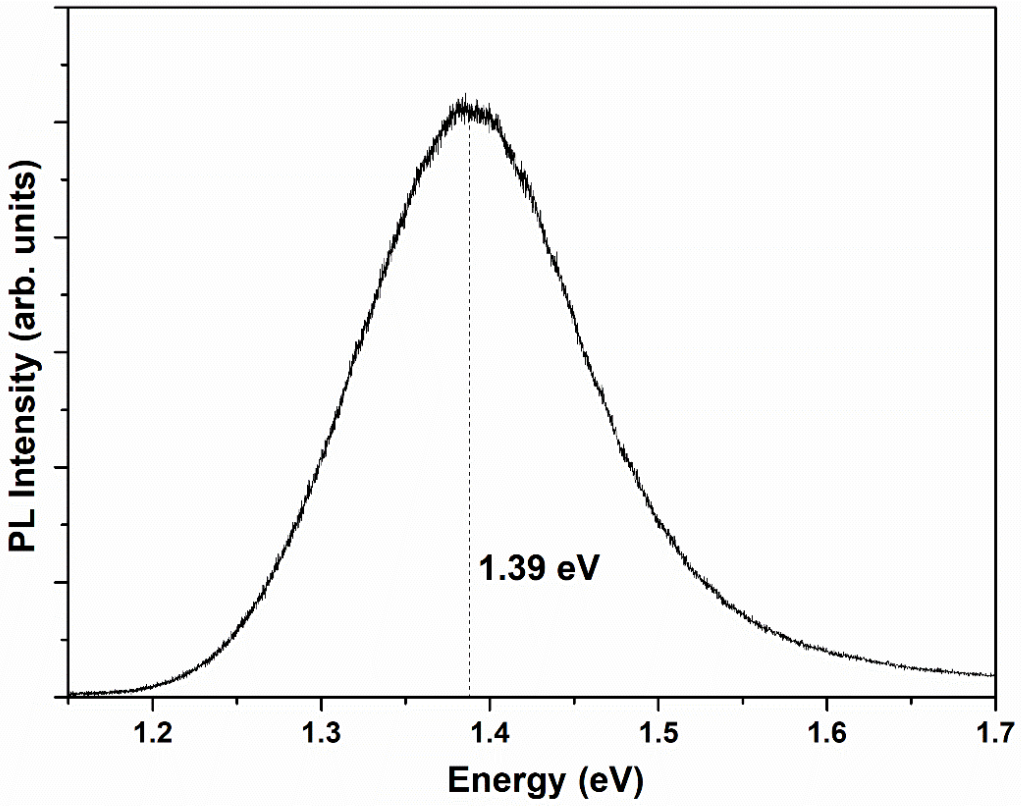

Figure 5. Photoluminescence spectrum of CZTS sample

4. CONCLUSION

In the present work, the CZTS sample was successfully produced using a two-stage method. In the first step, Cu, Sn and Zn layers were sputtered on Mo-coated glass to form Glass/Mo/CuSn/Zn/Cu. In the second stage, the precursor film annealed in sulfur atmosphere using the RTP method to convert it into kesterite CZTS structure. The CZTS sample was analyzed by different methods. As a result of EDX measurements, it was observed that there were no elemental losses as a result of the sulfurization process. The Cu stoichiometric and Zn rich composition was obtained in the prepared CZTS film. The diffraction planes of kesterite CZTS phase and trace of CuS were detected in the XRD pattern. As a result of Raman spectroscopy measurement, occurrence of kesterite CZTS phase was proved. In addition, presence of the CTS phase was also distinguished. The SEM image of CZTS sample exhibited polycrystalline surface structure. It was noted that the PL measurement show a transition around 1.39 eV and this is closed to the forbidden energy gap belonging to the CZTS phase. In summary, in this study, it has been shown that CZTS thin film structure can be formed without elemental loss with the RTP method employing very high heating rate.

SIMILARTY RATE: 22%

REFERENCES

[1] M. Nakamura, K. Yamaguchi, Y. Kimoto, Y. Yasaki, T. Kato, and H. Sugimoto, "Cd-Free Cu(In,Ga)(Se,S)2 Thin-Film Solar Cell With Record Efficiency of 23.35%," (in English), *IEEE Journal of Photovoltaics*, vol. 9, no. 6, pp. 1863-1867, Nov 2019, doi: 10.1109/jphotov.2019.2937218.

[2] M. A. Green, E. D. Dunlop, J. Hohl-Ebinger, M. Yoshita, N. Kopidakis, and X. Hao, "Solar cell efficiency tables (Version 58)," *Progress in Photovoltaics: Research and Applications,* vol. 29, no. NREL/JA-5900-80028, 2021.

[3] H. Katagiri, N. Sasaguchi, S. Hando, S. Hoshino, J. Ohashi, and T. Yokota, "Preparation and evaluation of Cu2ZnSnS4 thin films by sulfurization of E-B evaporated precursors," (in English), *Solar Energy Materials and Solar Cells,* vol. 49, no. 1-4, pp. 407-414, Dec 1997, doi: 10.1016/S0927-0248(97)00119-0.

[4] M. A. Olgar *et al.*, "Effect of heat treating metallic constituents on the properties of $Cu_2ZnSnSe_4$ thin films formed by a two-stage process," (in English), *Thin Solid Films,* vol. 624, pp. 167-174, Feb 28 2017, doi: 10.1016/j.tsf.2017.01.037.

[5] N. Akcay, T. Ataser, Y. Ozen, and S. Ozcelik, "Influence of Sulfurization Time on the Properties of Cu_2ZnSnS_4 Thin Films Deposited on Mo-coated Soda Lime Glass Substrates by Co-sputtering Technique," (in English), *Thin Solid Films,* vol. 704, p. 138028, Jun 30 2020, doi: ARTN 138028 10.1016/j.tsf.2020.138028.

[6] J. C. Jiang, L. Q. Zhang, W. Wang, and R. J. Hong, "The role of sulphur in the sulfurization of CZTS layer prepared by DC magnetron sputtering from a single quaternary ceramic target," (in English), *Ceramics International,* vol. 44, no. 10, pp. 11597-11602, Jul 2018, doi: 10.1016/j.ceramint.2018.03.225.

[7] Z. Zakaria *et al.*, "Effects of sulfurization temperature on Cu2ZnSnS4thin film deposited by single source thermal evaporation method," (in English), *Jpn J Appl Phys,* vol. 54, no. 8S1, p. 08KC18, Aug 2015, doi: 10.7567/jjap.54.08kc18.

[8] E. M. Mkawi, Y. Al-Hadeethi, E. Shalaan, and E. Bekyarova, "Substrate temperature effect during the deposition of (Cu/Sn/Cu/Zn) stacked precursor CZTS thin film deposited by electron-beam evaporation," (in English), *J Mater Sci-Mater El,* vol. 29, no. 23, pp. 20476-20484, Dec 2018, doi: 10.1007/s10854-018-0182-y.

[9] S. A. Vanalakar *et al.*, "A review on pulsed laser deposited CZTS thin films for solar cell applications," (in English), *J Alloy Compd,* vol. 619, pp. 109-121, Jan 15 2015, doi: 10.1016/j.jallcom.2014.09.018.

[10] H. Ahmoum *et al.*, "Impact of preheating environment on microstructural and optoelectronic properties of Cu_2ZnSnS_4 (CZTS) thin films deposited by spin-coating," (in English), *Superlattice Microst,* vol. 140, p. 106452, Apr 2020, doi: ARTN 106452 10.1016/j.spmi.2020.106452.

[11] R. Boudaira, O. Meglali, A. Bouraiou, N. Attaf, C. Sedrati, and M. S. Aida, "Optimization of sulphurization temperature for the production of single-phase CZTS kesterite layers synthesized by electrodeposition," (in English), *Surface Engineering,* vol. 36, no. 9, pp. 1000-1011, Sep 1 2020, doi: 10.1080/02670844.2020.1758013.

[12] K. V. Gunavathy, K. Tamilarasan, C. Rangasami, and A. M. S. Arulanantham, "Effect of solvent on the characteristic properties of nebulizer spray pyrolyzed Cu_2ZnSnS_4 absorber thin films for photovoltaic application," (in English), *Thin Solid Films,* vol. 697, p. 137841, Mar 1 2020, doi: ARTN 137841 10.1016/j.tsf.2020.137841.

[13] W. Shockley and H. J. Queisser, "Detailed Balance Limit of Efficiency of p-n Junction Solar Cells," (in English), *J Appl Phys,* vol. 32, no. 3, pp. 510-519, 1961, doi: 10.1063/1.1736034.

[14] Y. Gong *et al.*, "Identifying the origin of the V oc deficit of kesterite solar cells from the two grain growth mechanisms induced by Sn 2+ and Sn 4+ precursors in DMSO solution," *Energy & Environmental Science,* vol. 14, no. 4, pp. 2369-2380, 2021.

[15] M. Olgar, A. Sarp, A. Seyhan, and R. Zan, "Impact of stacking order and annealing temperature on properties of CZTS thin films and solar cell performance," *Renewable Energy,* vol. 179, pp. 1865-1874, 2021.

[16] O. Vigil-Galán *et al.*, "Secondary phases dependence on composition ratio in sprayed Cu_2ZnSnS_4 thin films and its impact on the high power conversion efficiency," (in English), *Solar Energy Materials and Solar Cells,* vol. 117, pp. 246-250, Oct 2013, doi: 10.1016/j.solmat.2013.06.008.

[17] H. Guan, H. L. Shen, C. Gao, and X. C. He, "Sulfurization time effects on the growth of Cu_2ZnSnS_4 thin films by solution method," (in English), *J Mater Sci-Mater El,* vol. 24, no. 8, pp. 2667-2671, Aug 2013, doi: 10.1007/s10854-013-1153-y.

[18] A. Emrani, P. Vasekar, and C. R. Westgate, "Effects of sulfurization temperature on CZTS thin film solar cell performances," *Solar Energy,* vol. 98, pp. 335-340, 2013.

[19] S. Yazici *et al.*, "Growth of Cu_2ZnSnS_4 absorber layer on flexible metallic substrates for thin film solar cell applications," (in English), *Thin Solid Films,* vol. 589, pp. 563-573, Aug 31 2015, doi: 10.1016/j.tsf.2015.06.028.

[20] J. He, L. Sun, Y. Chen, J. Jiang, P. Yang, and J. Chu, "Cu2ZnSnS4thin film solar cell utilizing rapid thermal process of precursors sputtered from a quaternary target: a promising application in industrial processes," (in English), *RSC Adv.,* vol. 4, no. 81, pp. 43080-43086, 2014, doi: 10.1039/c4ra07748b.

[21] M. A. Olgar *et al.*, "Effect of precursor stacking order and sulfurization temperature on compositional homogeneity of CZTS thin films," (in English), *Thin Solid Films,* vol. 615, pp. 402-408, Sep 30 2016, doi: 10.1016/j.tsf.2016.07.058.

[22] M. A. Olgar, M. Tomakin, T. Kucukomeroglu, and E. Bacaksız, "Growth of Cu_2ZnSnS_4 (CZTS) thin films using short sulfurization periods," (in English), *Materials Research Express,* vol. 6, no. 5, May 2019, doi: 10.1088/2053-1591/aaff78.

[23] V. Piacente, S. Foglia, and P. Scardala, "Sublimation study of the tin sulphides SnS_2, Sn_2S_3 and SnS," *J Alloy Compd,* vol. 177, no. 1, pp. 17-30, 1991.

[24] M. A. Olgar, J. Klaer, R. Mainz, L. Ozyuzer, and T. Unold, "Cu 2 ZnSnS 4 -based thin films and solar cells by rapid thermal annealing processing," (in English), *Thin Solid Films,* vol. 628, pp. 1-6, Apr 30 2017, doi: 10.1016/j.tsf.2017.03.008.

[25] P. A. Fernandes, P. M. P. Salome, and A. F. da Cunha, "Growth and Raman scattering characterization of Cu_2ZnSnS_4 thin films," (in English), *Thin Solid Films,* vol. 517, no. 7, pp. 2519-2523, Feb 2 2009, doi: 10.1016/j.tsf.2008.11.031.

[26] P. M. Salomé, P. A. Fernandes, J. P. Leitão, M. G. Sousa, J. P. Teixeira, and A. F. da Cunha, "Secondary crystalline phases identification in $Cu_2ZnSnSe_4$ thin films: contributions from Raman scattering and photoluminescence," *Journal of Materials Science,* vol. 49, no. 21, pp. 7425-7436, 2014.

[27] F. Hergert and R. Hock, "Predicted formation reactions for the solid-state syntheses of the semiconductor materials Cu_2SnX_3 and Cu_2ZnSnX_4 (X= S, Se) starting from binary chalcogenides," *Thin Solid Films*, vol. 515, no. 15, pp. 5953-5956, 2007.

[28] J. B. Li, V. Chawla, and B. M. Clemens, "Investigating the role of grain boundaries in CZTS and CZTSSe thin film solar cells with scanning probe microscopy," *Advanced Materials,* vol. 24, no. 6, pp. 720-723, 2012.

[29] M. A. Olgar, A. Seyhan, A. O. Sarp, and R. Zan, "The choice of Zn or ZnS layer in the stacked precursors for preparation of Cu_2ZnSnS_4 (CZTS) thin films," (in English), *Superlattice Microst,* vol. 146, p. 106669, Oct 2020, doi: 10.1016/j.spmi.2020.106669.

[30] H. Katagiri, N. Ishigaki, T. Ishida, and K. Saito, "Characterization of Cu2ZnSnS4Thin Films Prepared by Vapor Phase Sulfurization," (in English), *Jpn J Appl Phys,* vol. 40, no. Part 1, No. 2A, pp. 500-504, Feb 2001, doi: 10.1143/jjap.40.500.

Eurasian Journal of Science Engineering and Technology

Research

ZINC SULFIDE ANTI-REFLECTIVE THIN FILM COATING FOR GERMANIUM OPTICAL WINDOWS

Abdullah KARACA[1,*], Semran SAĞLAM[2], Emin BACAKSIZ[3], Süleyman ÖZÇELİK[4]

[1,3] Department of Physics, Faculty of Science, Karadeniz Technical University, Trabzon, Turkey.
[1] Department of Physics, Faculty of Science and Arts, Bozok University, Trabzon, Turkey.
[1,2,4] Department of Physics, Faculty of Science, Gazi University, Ankara, Turkey
[1,2,4] Photonics Application and Research Center, Gazi University, Ankara, Turkey

ABSTRACT

In this work, Anti-reflective thin film is made on Germanium (Ge) optical window, which is one of the most used materials in thermal imaging systems. ZnS material was used its optical transmittance between 2-14 µm and due to the fact that it has a refractive index proportional to the refractive index of Ge. ZnS thin films have been prepared by Radio Frequency (RF) magnetron sputtering on Germanium (Ge) optical windows for anti-reflection coating (ARC). ZnS films were produced at different thicknesses using RF sputtering system working pressures under 3, 20 and 30 mTorr. The other RF systems parameters such as RF power, deposition temperature were kept constant for all depositions. Crystal structures, optical and surface properties of ZnS thin films were characterized with X-ray diffraction (XRD), Atomic force microscopy (AFM), Fourier transform ınfrared (FTIR) and UV-VIS transmission spectrometer. The characterization results of Ge optical windows coated ZnS thin films grown at 3 mTorr pressure show that high optical transmission and good crystallinity in ınfrared wavelength region (2-14 µm).

Keywords: RF magnetron sputtering; Anti-reflective thin film; ZnS thin film, Growth parameters effect.

1. INTRODUCTION

Thin film anti-reflective coating is widely used the aim for fulfil or minimize reflections from the front and back surfaces of materials [1-4]. The increase in the permeability of the material with these coatings allows the improvement of optical properties. Unwanted reflection losses occur on the material surfaces, due to the high refractive index of the materials. For this reason, all nearly lens surfaces are given an antireflection coating to improve the light transmission and to eliminate detrimental effect [5-7].

Infrared transparent materials are gaining more and more importance every day especially night vision, remote sensing and communication. Germanium (Ge), one of these transparent materials, is the most commonly used material in infrared region as lens, optical windows, domes and optical filters due to its optical properties [8, 9]. The refractive index of single crystal Ge is about 4.00 (at 10 µm) and its reflection loss is approximately 50% in the wavelength range of 2-14 µm [8, 10, 11]. This unwanted reflection loss was occurred on the surface of its and reduces the optical efficiency [12, 13]. The optical transmission of Ge can have increased when AR coating is applied to the Ge's surface [14, 15]. Anti-reflection coating (ARC) for Ge lenses or optical windows is not only increased the optical transmission, but also provides surface adhesion, durability, protection and image clarity [4, 7, 16]. Material selection for ARC is one of the main problem in the desired wavelength range. The properties of many materials are not suitable for the ARC in infrared regions such as durability, toxicity, radioactivity, ect [17]. The other problem is the refractive index of the material. Particularly, ARC materials for the IR region must have both optical transmission and the refractive index must be proportional with the refractive index of Ge's. Considering these conditions, there is a limited number of coating materials.

It has been reported that single-sided, double-sided and multi-layer ARC can achieve high transmission by decreasing reflection between interfaces of air and materials. Especially with the integration of photovoltaic solar cells, ARC studies have gained a special importance. In solar cells, single layer ARC's such as MgF_2 (n=1.3 – 1.4) have been applied and short circuit current density value can improve. In order to achieve minimum reflection for infrared region imaging and other applications with low-cost, simple operation, Zinc sulfide (ZnS) was selected as anti-reflective coating material. ZnS is a semiconductor II-VI compound with refractive index of 2.20 and has an optical transmission of 0.4-13 µm [18]. This ensures that it is suitable as a transparent material in the visible and infrared regions. ZnS thin films can be produced into thin films using a variety of techniques such as thermal evaporation deposition, chemical bath deposition (CBD), electrochemical deposition, sol-gel, spin-coating or dip-coating, DC or RF magnetron sputtering etc [12, 18-22].

The thickness of the ZnS thin films is obtained for the Germanium using the Fresnel's equation [22].

---

* Corresponding author, e-mail: abdullah.karaca@bozok.edu.tr (A. Karaca)

Recieved: 05.04.2022 Accepted: 27.05.2022
doi: 10.55696/ejset.1099149

$$\boldsymbol{d} = \frac{\lambda}{4n_f} \tag{1}$$

in which n_f, are the refractive index of the ARC material and d is the thickness of the antireflection coating thin film, respectively. Single layer anti-reflective coatings exhibit maximum optical transmission for single wavelength, while multi layer anti-reflective coatings exhibit maximum optical transmission in the broad spectrum [23]. But for multi-layer antireflection, there are many difficulties affecting the characteristics of the film, such as the use of multiple materials, film production and stabilization to be optimized in appropriate thicknesses.

Herein, we prepared single layer, double layer and multi layer ZnS thin films as ARC on Ge optical window. The structural, optical and surface properties of ZnS anti-reflective thin films were investigated to some coating parameters. To depict the effect of pressure in ARC, single layer samples with the same thickness of multi-layer ARC properties have been conducted.

2. MATERIAL AND METHOD

Zinc sulfide (ZnS) thin films were fabricated on p-type Ge substrate by RF magnetron sputtering system. Ge were cleaned by ultrasonication bath for 15 min at 80°C bath temperature in deionized water and cleaned ethanol, acetone, respectively. After the cleaning process, the substrates were loaded into the RF magnetron system. ZnS with purity of 99,99% was used as target material for deposition into. The distance between the target and substrates were set up about 30 mm. Before deposition, sputtering system was evacuated to base pressure ($\approx 10^{-6}$ Torr) and Ar gas with flow rate 30 sccm was introduced into the chamber. The substrate temperature was set up 100 °C and were grown under 100 W. ZnS antireflective thin films generated chosen film thicknesses under working pressures 3,10 and 20 mTorr.
After the deposition, the thicknesses of the ZnS films were determined by stylus type profilometer (Veeco, Dektak 150) and shown in Table 1 and Table 2. The structural properties of Ge optical windows with and without ZnS thin films were obtained by X-ray diffraction (XRD) technique using APD 2000 PRO diffractometer system. The optical transmission properties of ZnS thin films were measured by the Vertex 80 Fourier transform infrared spectrometer (FTIR) in wavelengths ranging from 2 to 20 µm. UV-VIS transmission measurement were taken using Perkin Elmer Lambda 2. The surface morphology of ZnS thin films were imaged with an atomic force microscopy (NanoMagnetics Instruments Ltd., Oxford, UK).

Table 1. The thickness of ZnS thin films on single surface

Sample (for 3-5 µm)	Pressure (mTorr)	Average Thickness (nm)	Sample (for 8-12 µm)	Pressure (mTorr)	Average Thickness (nm)
S1	3	429	**S13**	3	1166
S2	20	430	**S14**	3	1226
S3	30	421	-	-	-

Table 2. The thickness of ZnS thin films on double surface

Sample (for 3-5 µm)	**Pressure (mTorr)**				**Average Thickness (nm)**			
	Front Surface		**Back Surface**		**Front Surface**		**Back Surface**	
S4	3		3		429		477	
S5	20		20		422		434	
S6	30		30		335		372	
Sample (for 8-12 µm)	**Pressure (mTorr)**				**Average Thickness (nm)**			
	Front Surface		**Back Surface**		**Front Surface**		**Back Surface**	
	First	**Second**	**First**	**Second**	**First**	**Second**	**First**	**Second**
S10	3	20	3	20	429	422	429	422
S11	3	-	3	20	429	-	429	422
S12	3	-	3	-	314	-	1195	-

After growing thin films at film thicknesses determined according to wavelength ranges, single-surface and double-surface coating analyzes were performed. After the samples grown under the same pressure from both sides, we were tested from both sides. According to the order determined in the table, the first coating of the front surface is carried out under 3 mTorr, while the second surface coating is carried out under the determined pressure for both surfaces. For example, while ZnS thin films are produced on both the front surface and the back surface under a pressure of 3-3 mTorr, 3-20 mTorr indicates that the back surface is growth under 20 mTorr. After the samples were characterized under 3, 20 and 30 mTorr, they were enlarged as a single surface, then a double surface, and then as a multi-layer under different pressure. In this context, while XRD and AFM was based on 3, 20 and 30 mTorr single surface coatings in characterization processes, FTIR measurements was performed for all samples.

3. RESULTS AND DISCUSSION

a) Structural Analysis

Especially, ZnS is commonly obtained in two crystalline forms: (a) cubic structure and (b) hexagonal wurtzite structure. These different phases are a recognizable difference in their physical properties. The peak of 2θ ≈ 28.50° is observed for all of thin film samples. This angle, which corresponds to the (111) plane in the ZnS cubic structure, forms the (002) plane in the hexagonal structure. The (100) plane is also consists of hexagonal wurtzite structure. The formation of these two phases depends on the applied temperature. Cubic phase is formed at low temperatures, while hexagonal phase is formed at high temperatures.

The structure of ZnS thin films were analyzed by X-ray diffraction (XRD). Fig. 1 shows XRD patterns of the ZnS thin films obtained at different pressures on Ge. Ge substrates were oriented (111) plane and single crystalline form (JCPDS file no. 4-545)[24]. The XRD patterns of ZnS thin films were scanned in the scattering angle (2θ) ranging from 10° to 90°. Between these angle values, it was given a range of 25° and 30° to determine which of the crystal structure is formed. On the other hand, in Fig. 1, the present samples grown at various pressures had only (111) plane and exhibited a cubic structure (JCPDS file no. 5-566)[25]. The highest peak value of XRD measurement comes from Ge optical windows and the pressure change affects film quality. As seen in Figure 2, it is seen that the hexagonal wurtzite structure is formed with the prolongation of the coating time (JCPDS file no. 36-1450)[26, 27]. Similar X-ray diffraction peaks were obtained many works for ZnS thin film deposited by RF-sputtering [26, 27]

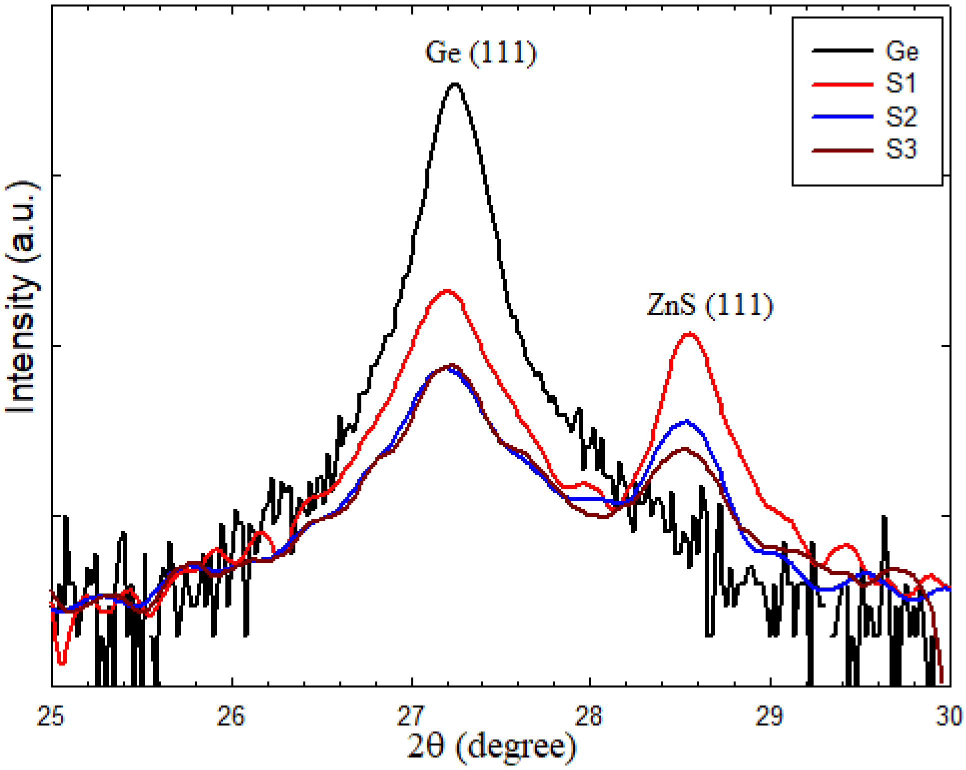

Figure 1. XRD patterns of ZnS films grown at different pressures

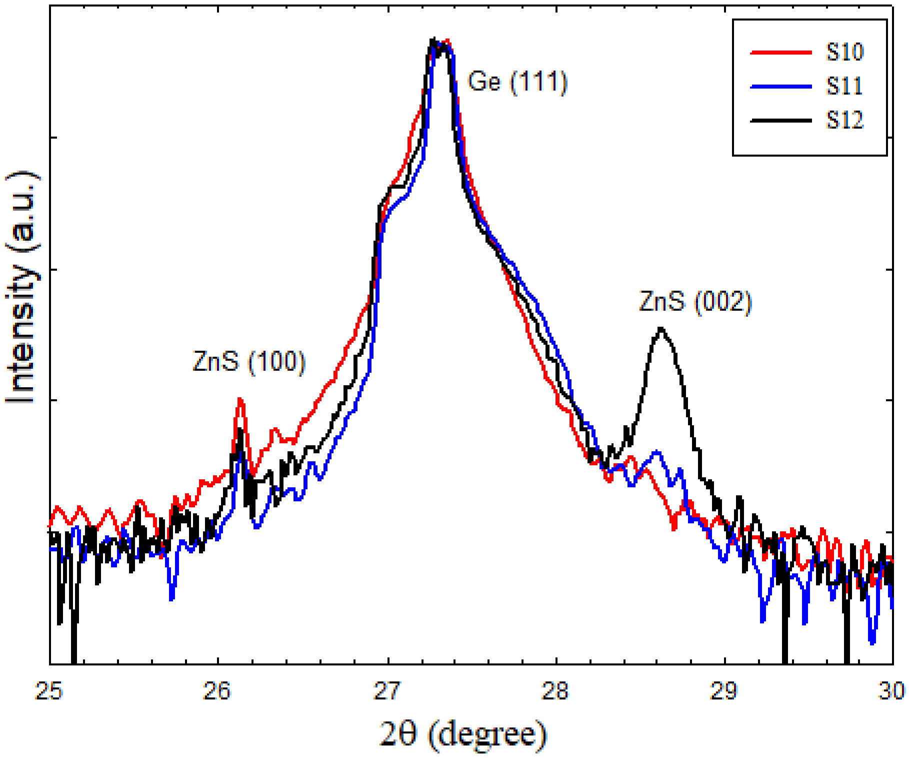

Figure 2. XRD patterns of ZnS films superimposed at different pressures

Figure 2. shows XRD patterns of superimposed ZnS thin films coating at different pressures. This indicated that the films were polycrystalline structures and that the planes were parallel to the substrate surface. For obtaining more structural information, the crystallite size of the prepared ZnS thin films were calculated from full width at half maximum (FWHM) of the diffraction peaks using the Debye-Scherrer equation [28];

$$D_{(hkl)} = \frac{k\lambda}{(\beta \cos \theta)} \tag{2}$$

where D is the crystallite size, k=0.9 is the crystallite shape factor, λ= 0.1540 nm is the wavelength of X-ray used for the diffraction measurements and β is the FWHM of the diffraction peaks at 2θ. The FWHM value of the film shows the disruption of the crystallinity, while the larger crystallite sizes indicate the improved crystallinity of the films [29]. FWHM values for ZnS thin films were measured by X-ray and shown in Table 3. XRD results shows better crystallinity for films produced under reduced pressures and the highest peak intensity clearly seen from the XRD spectra.

Table 3. The structural parameters of ZnS thin films

Sample	Average Thickness (nm)	β (degrees)	Crystallite Size by XRD (nm)
S1	429	0.261	32.83
S2	430	0.235	36,46
S3	421	0.228	37.59

b) Surface Analysis

The characterization of surface structures on a nanoscale is very important for the optoelectronic applications. Atomic force microscopy (AFM) is one of the several experimental techniques to study the surface properties of the deposited thin films [30]. AFM can be used to estimate crystallite grain size and surface roughness. AFM measurement was carried out to study the surfaces of Ge optical windows. Fig. 3 shows that two-dimensional (2D) and three-dimensional (3D) AFM images with 3 × 3 μm^2 scan area of the Ge optical windows with and without ZnS thin films.

We see a more homogeneous distribution in the scan with the presence of dark to indicate the presence of pockets or wells indicating the roughness of the thin films and also the absence of cracks on the surfaces of the layers, the same result was supported by Elidrissi. It can be seen in the Fig. 3 that the crystallinity of the films has been changed by different pressures of the sputtering system. Experimental results have shown that as the pressure increases, the crystal size values increase from 14.09 nm to 28.02 nm. The lowest roughness belongs to the sample grown under 3 mtorr pressure for films deposited in Ge optical windows. We can say that Ge is the smoothest substrate and has a size of the smallest grains. Surface roughness is all irregularities of the surface and micro-graphic character. This indicates that the rough nature of the thin layers of ZnS is caused by the growth mechanism of the technique of sputtering. Thanks to its roughness, this material allows light to be scattered rather than reflected at the interface; this allows high transmittance for almost all samples as shown in the subsequent analysis of optical spectra compared to the specular component.

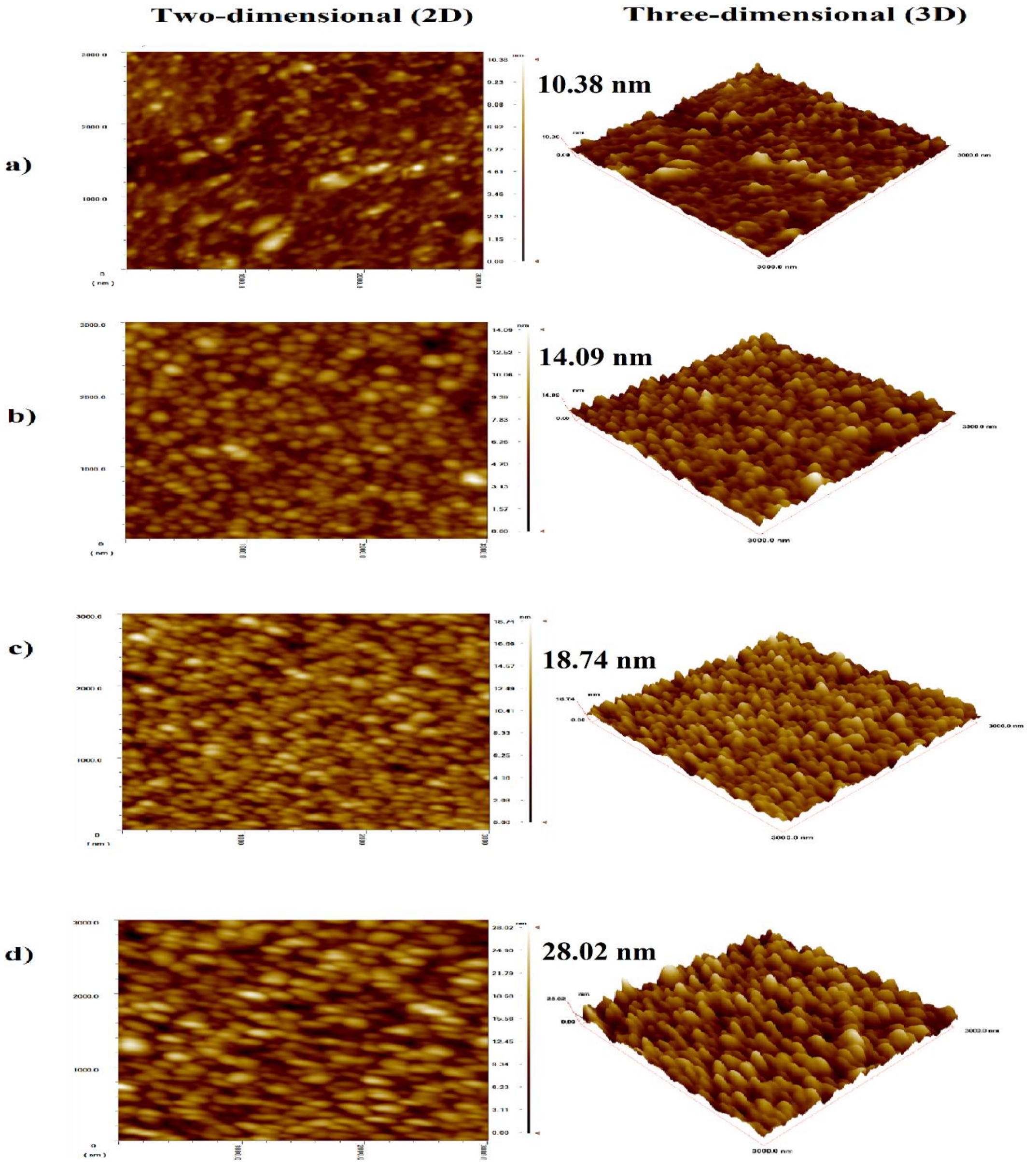

Figure 3. ZnS thin film AFM 2D and 3D images on Ge optical windows A) Ge without ZnS b) 3 mTorr Ge/ZnS c)20 mTorr Ge/ZnS d)30 mTorr Ge/ZnS

c) Optical Analysis

The optical properties of samples were analyzed using FTIR spectrometer. First of all, calibration was performed for FTIR device. ZnS thin film coated Ge optical windows are placed perpendicular to the beam direction. The transmission spectra for Ge optical windows are shown in Fig. 4-a, 4-b, 4-c and 4-d which was recorded at room temperature by the FTIR for wavelengths ranging from 2-20 µm. Figure 4-a and Figure 4-c are single-surface coated, while Figure 4-b and Figure 4-d are of samples double surface coated. While the maximum average transmittance, 67%, is observed for the film deposited one surface coating, double surface coating transmittance are observed 98% and 99%, respectively for 2-20 µm wavelength range. Growing ZnS atoms with different pressure parameters results in higher optical transmittance of the film. It can be seen that transmittance increases when the film thickness increases at superimposed thin films deposited. ZnS coated Ge optical windows can be observed to have increased optical transmission at certain wavelengths in the specified film thicknesses. Therefore, we note that the reflection curves are not interference; It is due to the multiple reflections of the two interference layers due to the importance of the roughness of thin films. Therefore, in our case this ZnS thin film can be applied as infrared imaging.

ZnS thin films were coated in soda lime glass using the same coating parameters to determine the refractive index. The UV-VIS transmission spectrum obtained glass, S1 and S10 samples and given in Fig. 5. Regarding the refractive index study as a function of wavelength variation in the UV- VIS region, it can be seen depending on the nature of the glass shown in Fig. 5. The graph indicate that the samples has a good optical transparency in visible and part of near infrared wavelength range with the average transmittance minimum of 60% and the maximum of 85%. The refractive index of ZnS was calculated as 2,18 with the help of envelope method [31, 32]. We note that the refractive index of the ZnS layer deposited on the glass is in agreement with reported references.

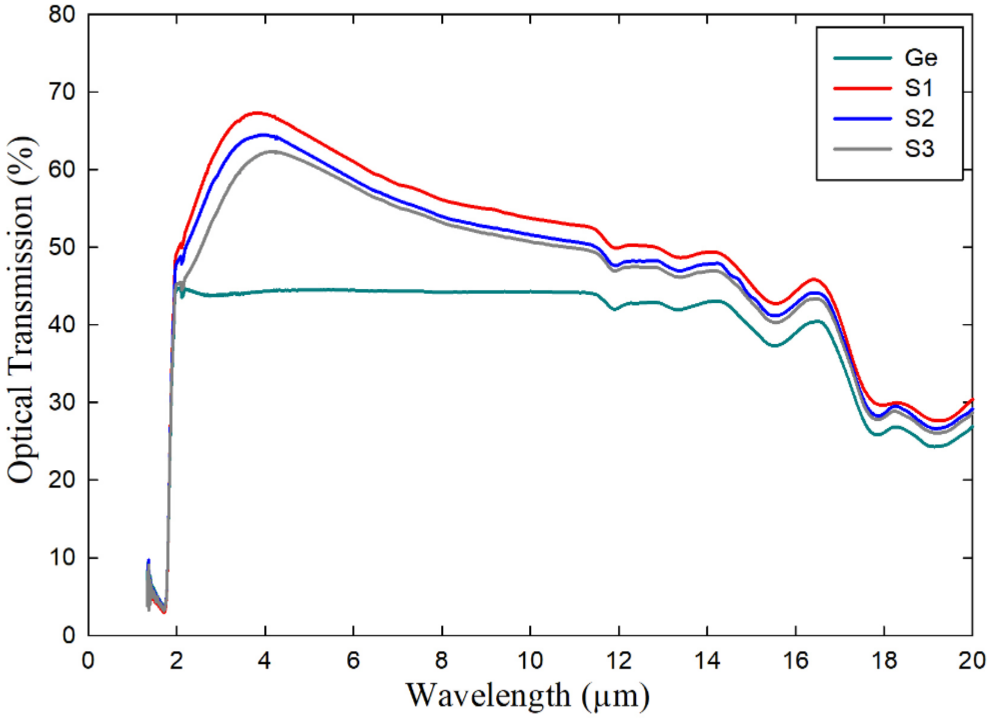

Figure 4- a. The optical transmission spectra of Ge optical windows with and without ZnS ARCs at different pressures

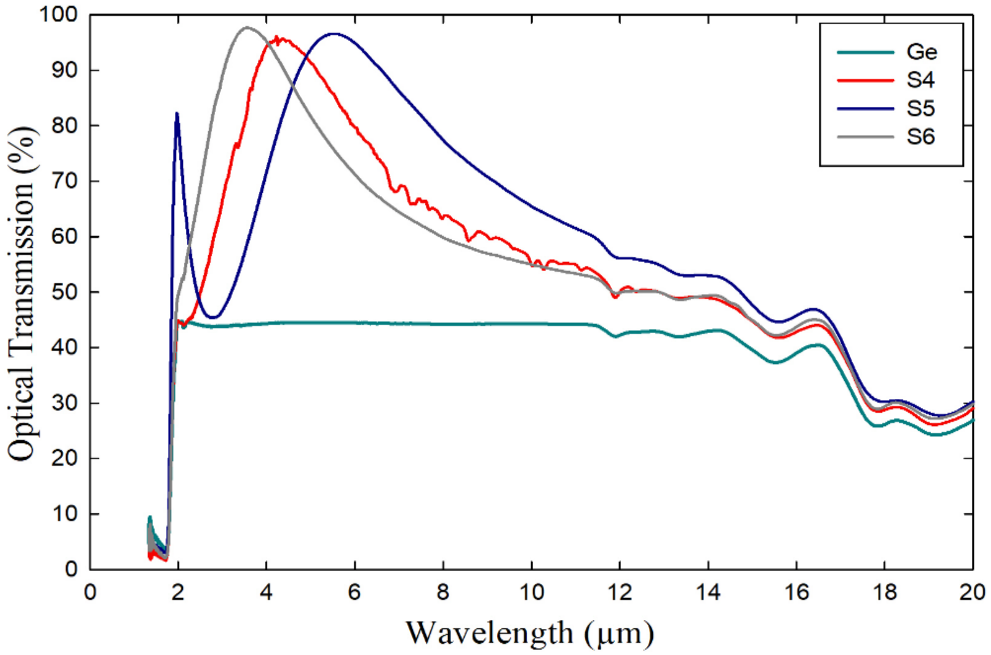

Figure 4- b. The optical transmission spectra of Ge optical windows coated on both surface at different pressures

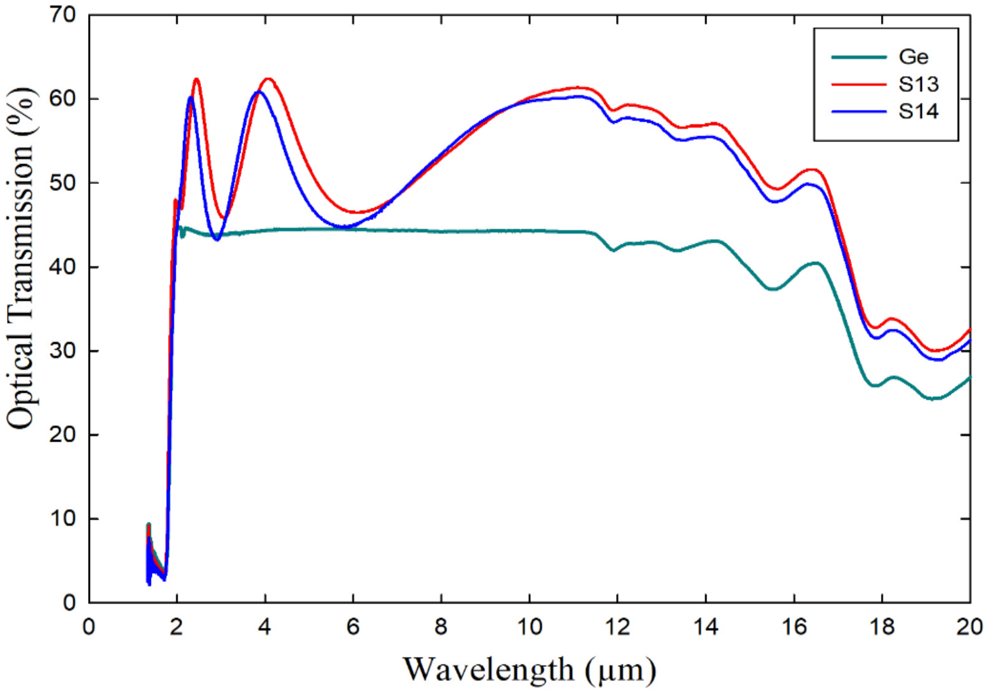

Figure 4- c. The optical transmission spectra of Ge optical windows with and without ZnS ARCs for 8 -12 µm at different pressures

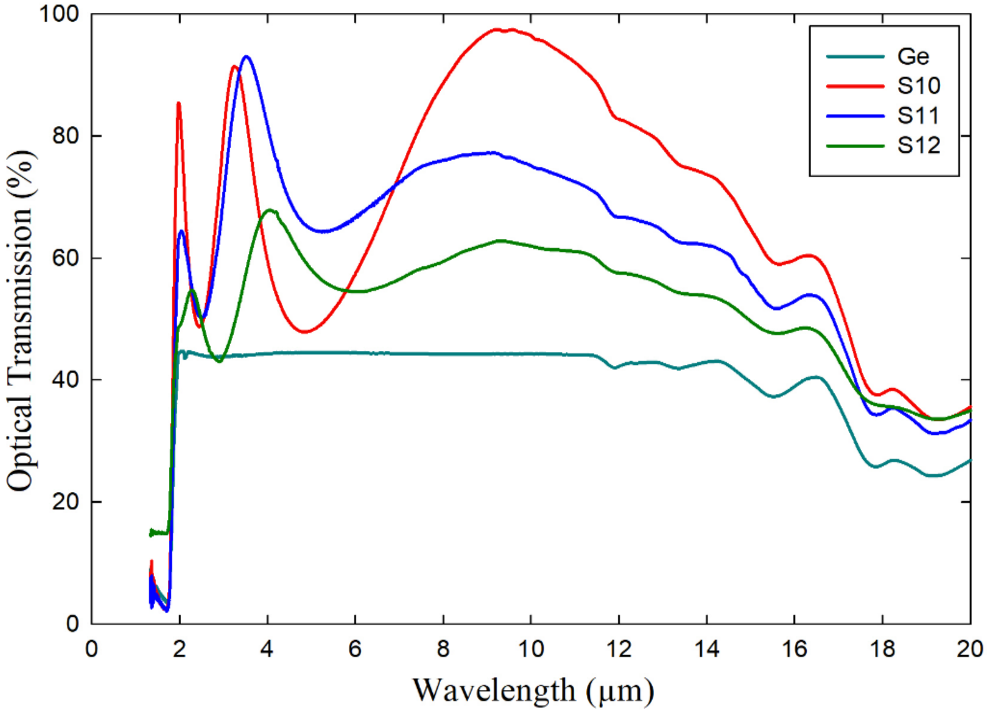

Figure 4- d. The optical transmission spectra of Ge optical windows coated on both surface at different pressures for 8 -12 µm.

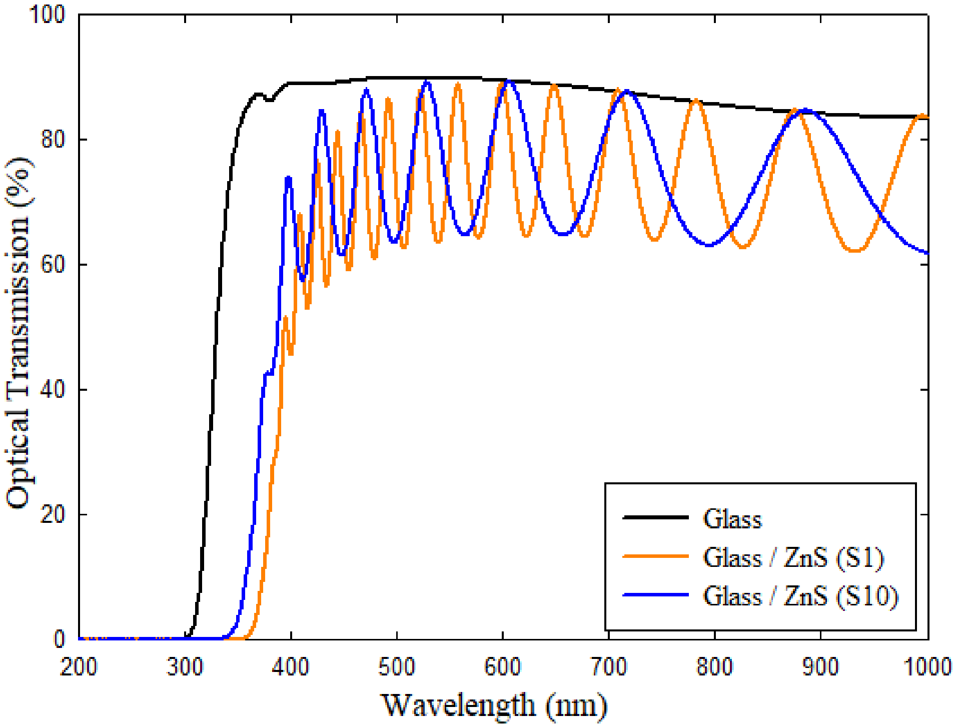

Figure 5. The optical transmission spectra of ZnS thin film on glass

4. CONCLUSION

In summary, ZnS antireflection films were successfully deposited on Ge optical windows and soda lime glass at different pressures by RF magnetron sputtering. It was found that the deposited ZnS thin films exhibited a strong XRD peak at around 28.50 degree with an orientation of the (111) plane. X-ray diffraction analysis has also revealed a change in the thin film structure from cubic to hexagonal. AFM measurements showed that the surface roughness and grain sizes of the films increased as the pressure decreased. The FTIR results indicate that the IR transmission increases by about 26% on surfaces of the Ge by deposition of single layer ZnS ARC and the maximum is almost 99% in the 2-14 nm wavelength range using double layer coating. Using envelope method, Refractive index was determined. UV - Vis spectra showed that ZnS thin films has a good transmission. The peak position of the maximum in the transmittance spectra for optical windows can be shifted to the wanted wavelength by changing the optical thickness of the coating.

SIMILARTY RATE: 16%

ACKNOWLEDGEMENT

This work was supported by Ministry of Development (TR) and TUBITAK under the 2011K120290 and 115F280 project numbers, respectively.

REFERENCES

[1] H. A. Macleod, *Thin-Film Optical Filters*, Fourth ed.: CRC press, London, 2010.
[2] C. Claeys and E. Simoen, *Germanium-based technologies: from materials to devices*: Elsevier, p.17, 2011.
[3] I. Chambouleyron and J. Martínez, "Optical Properties of Dielectric and Semiconductor Thin Films," in *Handbook of Thin Films*, ed: Elsevier, 2002, pp. 593-622.
[4] A. Musset and A. Thelen, "IV Multilayer Antireflection Coatings," in *Progress in Optics*. vol. 8, E. Wolf, Ed., ed: Elsevier, 1970, pp. 201-237.
[5] J. A. Dobrowolski, "Optical properties of films and coatings," *Handbook of optics*, vol. 1, pp. 42.3-42.130, 1995.
[6] R. Gade and T. B. Moeslund, "Thermal Cameras and Applications: a Survey," *Machine Vision and Applications*, vol. 25, pp. 245-262, 2014.
[7] J. M. Lloyd, *Thermal imaging systems*: Springer Science & Business Media, 2013.
[8] W. C. Dash and R. Newman, "Intrinsic Optical Absorption in Single-Crystal Germanium and Silicon at 77," *Physical Review*, vol. 99, pp. 1151-1155, 08/15/ 1955.
[9] A. R. Hilton, "Infrared transmitting materials," *Journal of Electronic Materials*, vol. 2, pp. 211-225, May 01 1973.
[10] B. Depuydt, M. De Jonghe, W. De Baets, I. Romandic, A. Theuwis, C. Quaeyhaegens, *et al.*, "Chapter 1 - Germanium Materials," in *Germanium-Based Technologies*, ed Oxford: Elsevier, 2007, pp. 11-I.
[11] G. K. Teal and J. B. Little, "Growth of germanium single crystals," in *Physical review*, 1950, pp. 647-647.
[12] H. K. Raut, V. A. Ganesh, A. S. Nair, and S. Ramakrishna, "Anti-reflective coatings: A critical, in-depth review," *Energy & Environmental Science*, vol. 4, pp. 3779-3804, 2011.
[13] A. Rogalski and K. Chrzanowski, "Infrared devices and techniques," *Optoelectronics Review*, vol. 10, pp. 111-136, 2002.
[14] A. Ghosh, P. Kant, P. Bandyopadhyay, P. Chandra, and O. Nijhawan, "Antireflection coating on germanium for dual channel (3–5 and 7.5–10.6 μm) thermal imagers," *Infrared physics & technology*, vol. 40, pp. 49-53, 1999.
[15] D. C. Harris, "Durable 3–5 μm transmitting infrared window materials," *Infrared physics & technology*, vol. 39, pp. 185-201, 1998.
[16] A. j. Mushtak, "Design of high efficiency multilayer antireflection coatings for visible and infrared substrates," *Journal of College of Education*, pp. 733-746, 2009.
[17] P. Klocek, *Handbook of infrared optical materials*: CRC Press, 2017.
[18] M. Nadeem, W. Ahmed, and M. Wasiq, "ZnS thin films–an overview," *Journal of research science*, vol. 16, pp. 105-112, 2005.
[19] M. Islam, M. Hossain, M. Aliyu, Y. Sulaiman, M. Karim, K. Sopian, *et al.*, "Comparative Study of ZnS Thin Films Grown by Chemical Bath Deposition and Magnetron Sputtering," in *Electrical & Computer Engineering (ICECE), 2012 7th International Conference on*, 2012, pp. 86-89.
[20] A. T. Salih, A. A. Najim, M. A. Muhi, and K. R. Gbashi, "Single-Material Multilayer ZnS As Anti-Reflective Coating For Solar Cell Applications," *Optics Communications*, vol. 388, pp. 84-89, 2017.

[21] D. Yoo, M. S. Choi, S. C. Heo, C. Chung, D. Kim, and C. Choi, "Structural, optical and chemical analysis of zinc sulfide thin film deposited by RF-mganetron sputtering and post deposition annealing," *Metals and Materials International,* vol. 19, pp. 1309-1316, November 01 2013.

[22] S. Firoozifar, A. Behjat, E. Kadivar, S. Ghorashi, and M. B. Zarandi, "A Study of the Optical Properties and Adhesion of Zinc Sulfide Anti-Reflection Thin Film Coated on a Germanium Substrate," *Applied Surface Science,* vol. 258, pp. 818-821, 2011.

[23] K. Wasa and S. Hayakawa, "Handbook of sputter deposition technology," p. 177, 1992.

[24] A. Rolo, O. Conde, M. Gomes, and M. Dos Santos, "Structural, chemical and optical characterisation of Ge-doped SiO2 glass films grown by magnetron rf-sputtering," *Journal of Materials Processing Technology,* vol. 92, pp. 269-273, 1999.

[25] C. Cruz-Vázquez, F. Rocha-Alonzo, S. Burruel-Ibarra, M. Barboza-Flores, R. Bernal, and M. Inoue, "A new chemical bath deposition method for fabricating ZnS, Zn (OH) 2, and ZnO thin films, and the optical and structural characterization of these materials," *Applied Physics A,* vol. 79, pp. 1941-1945, 2004.

[26] P. Chelvanathan, Y. Yusoff, F. Haque, M. Akhtaruzzaman, M. Alam, Z. Alothman, *et al.*, "Growth and characterization of RF-sputtered ZnS thin film deposited at various substrate temperatures for photovoltaic application," *Applied Surface Science,* vol. 334, pp. 138-144, 2015.

[27] D. H. Hwang, J. H. Ahn, K. N. Hui, K. San Hui, and Y. G. Son, "Structural and optical properties of ZnS thin films deposited by RF magnetron sputtering," *Nanoscale research letters,* vol. 7, pp. 1-7, 2012.

[28] H. Klug and L. Alexander, "Crystallite size and lattice strains from line broadening," *X-ray Diffraction Procedures for Polycrystalline and Amorphous Materials. New York, USA: Wiley-Interssciences,* pp. 618-708, 1974.

[29] L. Whittig and W. Allardice, "X-ray diffraction techniques," *Methods of Soil Analysis: Part 1—Physical and Mineralogical Methods,* pp. 331-362, 1986.

[30] F. J. Giessibl, "Advances in atomic force microscopy," *Reviews of modern physics,* vol. 75, p. 949, 2003.

[31] M. Caglar, Y. Caglar, and S. Ilican, "The determination of the thickness and optical constants of the ZnO crystalline thin film by using envelope method," *Journal of optoelectronics and advanced materials,* vol. 8, p. 1410, 2006.

[32] J. Müllerová and J. Mudro, "Determination of optical parameters and thickness of thin films deposited on absorbing substrates using their reflection spectra," *Acta Phys. Slov.,* vol. 50, pp. 477-488, 2000.

Eurasian Journal of Science Engineering and Technology

Research

IMPACT OF SELENIZATION TEMPERATURE AND PRE-ANNEALING TREATMENT ON THE MICROSTRUCTURAL PROPERTIES OF $Cu_2ZnSnSe_4$ THIN FILMS GROWN BY RAPID THERMAL PROCESS

Yavuz ATASOY[1*], Mehmet Ali OLĞAR[2]

[1,2] Nigde Omer Halisdemir University, Nanotechnology Research Center, 51240, Nigde, Turkey
[1]Niğde Ömer Halisdemir University, Niğde Zübeyde Hanım Health Services Vocational High School, 51240 Niğde
[2]Nigde Omer Halisdemir University, Physics Department, 51240, Nigde, Turkey

ABSTRACT

The impact of selenization temperature and pre-annealing treatment on the microstructural characteristics of CZTSe thin films were studied. CZTSe thin films were obtained by two-stage process. This processes includes deposition of metallic layers and Se cap layer employing physical vapor deposition systems followed by selenization process performed at elevated temperatures using RTP system with a heating rate of 8°C/s. The compositional properties of CZTSe thin films changed after the heat treatment, but performing pre-annealing treatment before high reaction temperature (550°C) partially prevented element loss in CZTSe compound. Both Raman and XRD measurements confirmed the formation of the kesterite CZTSe phase. However, according to Raman results, CZTSe phase started to decompose into secondary phases such as CTS regardless of temperature. According to the top view images of the samples, the grain structure completely changed with employing heat treatment. Zn-rich phase detected in reacted sample at 550 °C, which indicates decomposition of CZTSe that is confirmed in Raman spectra.

Keywords: CZTSe thin film, RTP, XRD, Microstructure

1. INTRODUCTION

$Cu_2ZnSn(S,Se)_4$ (CZTSSe) semiconductor compound can be used as an active absorber layer in thin film solar cells due to its optical and electrical properties such as 1.5 eV forbidden energy gap, high absorption coefficient ($\geq 10^4$ cm^{-1}) and p type conductivity. CZTSSe compound is seen to be as an alternative to the $CuInGaSe_2$ (CIGSe) in thin film solar cells, since it contains inexpensive and abundant raw materials. However, there is a huge difference between experimental and theoretical efficiency values of CZTSSe-based solar cells compared to CIGSe. Studies have been conducted to reveal the possible causes of this difference. The main reasons for such difference are the crystallization of the kesterite CZTSSe structure in a very narrow range in the phase diagram [1], requiring partial pressure for S and/or Se during annealing [2], and the decomposition of the CZTSSe compound at high temperatures [3].

There are several reported work in the literature to find out the optimum growth parameters of CZTSSe absorber material for understanding the efficiency limitations [4-8]. For example, Márquez-Prieto et al. examined the effect of the annealing treatment on the optical and structural properties of CZTSe thin films and they reported that the $SnSe_2$ phase was formed at low temperatures (450°), while the $MoSe_2$ phase was started to form as a result of the reaction of Mo back contact layer with Se at higher temperature (550°) [9]. On the other hand, Kumar et al. produced CZTSe thin films by thermal deposition of Cu, Zn, Sn, and Se on Mo-coated SLG substrates followed by selenization process using various temperature and time. According to this study, with increasing temperature, CuSe phase was formed in the film, grain size and conductivity of the film increased [10]. Several groups have included the pre-annealing step as a process strategy for CZTSe production [11, 12]. This pre-annealing treatment is applied to promote the diffusion and mixing of metals. In this way, the compositional and morphological homogeneity of the CZTSe film are promoted. In another study carried out by our group, the effect of mild annealing on the film features was studied. In that study, the metallic precursors were exposed to a pre-annealing treatment for 30 min at a temperature range of 200–350 °C and then selenized at 550 °C for 15 min in tubular furnace. We demonstrate that the CZTSe thin film produced by employing metallic stacks annealed at 250 °C was provided proper composition and crystalline quality [13].

In this study, we report the effect of selenization temperature and pre-annealing process on the microstructural properties of CZTSe thin films grown by rapid thermal processing (RTP).

---

* Corresponding author, e-mail: yavuzatasoy@ohu.edu.tr (Y. Atasoy)

Recieved: 07.04.2022 Accepted: 09.05.2022
doi: 10.55696/ejset.1100103

2. MATERIAL AND METHOD

The $Cu_2ZnSnSe_4$ thin films were produced by two-stage process consisting of i) sequential deposition of Cu (Kurt J. Lesker, 5N), Zn (Kurt J. Lesker, 4N), Sn (Beijing Goodwill Metal, 5N) layers by sputtering system, ii) deposition of Se cap layer using Se shots (Alfa Aesar, 5N) by vacuum evaporation, and iii) subsequent selenization (pre/post annealing) in graphite box using RTP method. The SLG/Mo/Cu/Sn/Zn/Cu stacked layer was covered onto Molibdenyum coated substrate. 500 nm thick Mo (Beijing Goodwill Metal, 4N) layer was deposited by DC sputtering system. While Cu layer was deposited using by DC source, Zn and Sn layers were deposited by RF power supply. The total thickness of stack is about 650 nm for the metallic layer with Cu / (Sn + Zn) = 0.80 and Zn / Sn=1.20 atomic ratio [14]. The thickness of the layers were measured using profilometre. The Se cap layer was coated onto metallic layers by vacuum evaporation with a thickness of 400 nm and the film thickness was monitored using a crystal controller. For formation of CZTSe, SLG/Mo/Cu/Sn/Zn/Cu/Se stacked precursor layers were placed in graphite box within a selenium powder (15 mg) and then annealing treatment was performed using 8 °C/s heating rate in RTP system. Selenization procedure was performed at 500°C and 550°C for 3 min. In addition, one CZTSe sample was prepared with pre-annealing at 250 °C for 3 min followed by post annealing at 550 °C for 1 min.

The atomic percentages of CZTSe samples were measured (point and map) by energy dispersive X-ray spectroscopy (EDS, FEI Quanta 250 equipped with EDX detector and Oxford Aztec software). The structural properties of the samples were characterized by X-ray diffraction method (XRD, Panalytical, Empyrean) and Raman spectroscopy (633 nm) (Renishaw, Invia). The surface structure of the CZTSe samples were monitored by scanning electron microscopy (SEM, FEI Quanta 250).

3. RESULTS AND DISCUSSION

The atomic percentage and some atomic ratios of metallic stack and the reacted CZTSe samples were given in Table 1. Cu / (Sn+Zn) and Zn / Sn ratio of the metallic layers are 0.86 and 1.19, respectively. The sample reacted at 500 °C continued to have a copper poor and zinc rich composition, but Zn / Sn value of the film increased to 1.53. This indicates that element loss (Sn) took place in the structure. On the other hand, it was determined that the Sn loss increased with the increment of reaction temperature, but the amount of Sn loss decreased partially by employing pre-treatment. Due to high vapor pressure, Sn(Se) is a volatile compound, that can evaporate easily [15, 16]. Under these experimental conditions, it has been determined that high heating rate was not sufficient to prevent Sn loss, but pre-annealing treatment inhibited the elemental loss partially by formation of metallic alloying.

Table 1. EDX results of CZTSe thin films

Sample	Cu (%)	Sn (%)	Zn (%)	Se (%)	$\frac{Cu}{(Sn+Zn)}$	$\frac{Zn}{Sn}$	$\frac{Se}{(Cu+Sn+Zn)}$
Metallic stack	46.16	24.56	29.28	-	0.86	1.19	-
CZTSe-(500)	23.20	9.51	14.60	52.69	0.96	1.53	1.11
CZTSe-(550)	19.59	10.00	16.95	53.46	0.73	1.69	1.14
CZTSe-(250/550)	20.26	10.02	16.34	53.38	0.77	1.63	1.14

The XRD pattern of CZTSe-(500), CZTSe-(550) and CZTSe-(250/550) samples measured in the range of 2θ=20-60° shown in Figure 1. Regardless of the reaction temperature, there are three main peaks located at 2θ= 27.1°, 45.1°and 53.4° which were respectively refered to (112), (220 / 204) and (312 / 116) diffraction planes of the kesterite CZTSe structure (JCPDS card no: 01-070-8930) [17]. Apart from the characteristic CZTSe peaks, the peak of the Mo phase was observed at an angle of about 2θ = 40.5 (JCPDS card no: 01-089-5023). In addition, the peaks of the $MoSe_2$ phase formed as a result of the Mo-Se reaction at high reaction temperature (>500°) that were detected at 2θ = 31.5° and 55.8° (JCPDS card no: 09-0312)

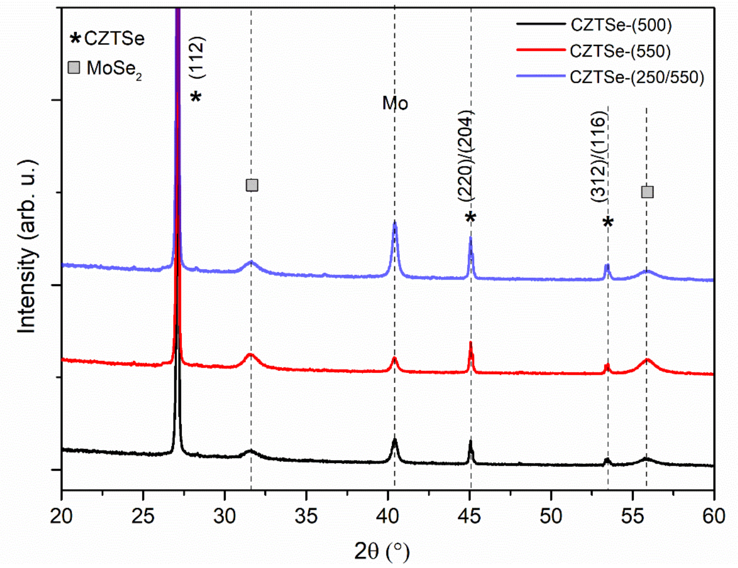

Figure 1. XRD spectra of CZTSe thin films

The crystallite size (D) and micro strain (Ɛ) values of the reacted samples were calculated using Equations 1 and 2, respectively [18, 19]. K is the shape factor (K=0.9), β_{hkl} is the full width at half maximum (FWHM) of (112) diffraction plane of the CZTSe samples and λ is the wavelength of the X-ray (λ=1.5406 Å). The calculated values were given in Table 2. The FWHM value, which is an indicator of crystal quality, expresses the formation of sharper peak due to the contribution of identically oriented planes to the diffraction peak. While this value was 0.125 for the sample reacted at 500°C, it reached the lowest value (best crystal quality) with increasing temperature to 550 °C, but it was increased partially with pre-annealing treatment. It was seen that the dependence of crystallite size and micro-strain values with annealing treatment is similar to the behavior of the FWHM value. As a result, it can be said that CZTSe-(550) has the highest crystal size and lowest strain, that is, it is low-defective and high-crystal-quality compound.

$$D = \frac{K\lambda}{\beta_{hkl}\cos\theta} \tag{1}$$

$$\varepsilon = \frac{\beta_{hkl}\cos\theta}{4} \tag{2}$$

The CZT(S,Se) structure has similar XRD patterns with the $Cu_2Sn(S,Se)_3$ and/or Zn(S,Se) phases. Therefore, Raman measurements of the samples were taken and given in Figure 2, for both confirmations the occurrence of the kesterite CZTSe phase and detection whether the crystallized phases with similar structures were formed. As seen in figure, the Raman peaks related to CZTSe kesterite phase were detected at 172, 195 and 235 cm^{-1} regardless of the temperature. In addition, relatively less intense peak was detected at 251 cm^{-1} which was attributed to CTSe phase in annealed samples. This shows that decomposition has started in the samples produced at ≥500°C temperature with high heating rate.

Table 2. Some structural parameters of the samples calculated by XRD datas

Sample	FWHM(°)	Crystallite size (nm)	ϵ (strain) (x10^{-4})
CZTSe-(500)	0.125	65.4	5.5
CZTSe-(550)	0.084	97.3	3.7
CZTSe-(250/550)	0.093	87.9	4.1

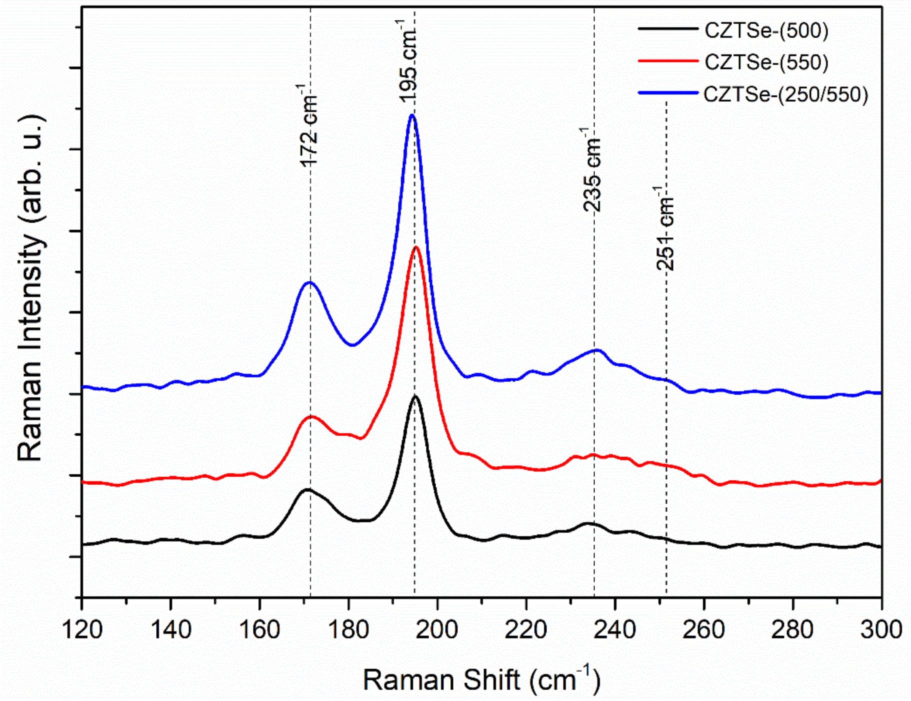

Figure 2. Raman spectra of CZTSe samples

Top view SEM images of CZTSe samples are demonstrated in Figure 3. According to images, CZTSe-(500) has a rounded-shape grain-structure which is dense and homogeneous but, some voids and/or cracks are also seen in the surface structure. It was observed that the grain size increased from 1-3 micrometers to 2-5 micrometers by increasing the temperature to 550°C. However, as the enlarged image of the sample was examined in detail (figure 3d), it was seen that submicron grains were formed both between and on the large grains. According to the atomic composition results given in Table 3, large grains have the targeted composition of CZTSe (point B), while small grains correspond to a Zn rich phase (point A). In addition to this, the phase of the small grain structure may be in the form of $Cu_{1.7}Zn_{2.2}Sn_1Se_{5.3}$. Employing with pre-annealing treatment to the same sample, it was observed that the grain size decreased, while a more compact structure was formed.

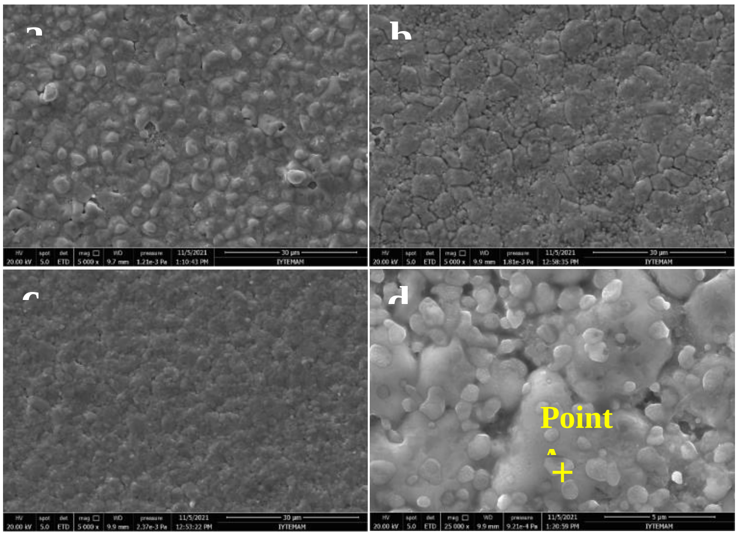

Figure 3. The SEM images of the surface morphology of CZTSe thin films; a) CZTSe-(500), b) CZTSe-(550), c) CZTSe-(250/550), d) Enlarged view of CZTSe-(550)

Table 3. EDX results from different points of the surface of the CZTSe-(550) sample

Sample	Cu (%)	Sn (%)	Zn (%)	Se (%)	$\frac{Cu}{(Sn+Zn)}$	$\frac{Zn}{Sn}$	$\frac{Se}{(Cu+Sn+Zn)}$
CZTSe-(550-point A)	15.84	9.35	20.88	53.93	0.52	2.23	1.17
CZTSe-(550-point B)	23.61	12.30	13.05	51.04	0.93	1.06	1.04

4. CONCLUSION

In this study, the effect of selenization temperature and pre-annealing treatment on the microstructural features and atomic composition of CZTSe thin film were investigated. The precursor stacks formed by deposition of Cu, Sn, Zn layers via sputtering system and thermally evaporated Se cap layer, then were annealed at different temperatures with a heating rate of 8°C/s using RTP system. The EDX measurements showed that after annealing treatments, the CZTSe thin film had a copper poor and zinc rich composition, but elemental Sn loss was determined. The XRD and Raman results of the samples demonstrated evolution of kesterite CZTSe structure. However, CTSe and Zn-rich undesired phases in the structure were detected in Raman spectra and SEM images, respectively. Overall, in a two-step process employed for the formation of CZTSe layer, it is recommended that pre-annealing reaction step can be used where the reaction temperature is raised rapidly to > 500°C in presence of Se atmosphere. In addition, further investigation is needed to obtain purer and higher quality of CZTSe thin film using various heating rates in the RTP system.

SIMILARTY RATE: 18%

ACKNOWLEDGEMENT

The work was supported by grants from TUBITAK (120F029).

REFERENCES

[1] I. Dudchak, L. J. J. o. a. Piskach, and compounds, "Phase equilibria in the Cu2SnSe3–SnSe2–ZnSe system," vol. 351, no. 1-2, pp. 145-150, 2003.

[2] J. J. Scragg, P. J. Dale, D. Colombara, and L. M. J. C. Peter, "Thermodynamic aspects of the synthesis of thin-film materials for solar cells," vol. 13, no. 12, pp. 3035-3046, 2012.

[3] A. Redinger *et al.*, "Route Toward High-Efficiency Single-Phase Cu $ _ {\bf 2} $ ZnSn (S, Se) $ _ {\bf 4} $ Thin-Film Solar Cells: Model Experiments and Literature Review," vol. 1, no. 2, pp. 200-206, 2011.

[4] P. Fan *et al.*, "Effects of annealing treatment on the properties of CZTSe thin films deposited by RF-magnetron sputtering," vol. 625, pp. 171-174, 2015.

[5] P. Salomé, P. Fernandes, and A. d. J. p. s. s. c. Cunha, "Influence of selenization pressure on the growth of Cu2ZnSnSe4 films from stacked metallic layers," vol. 7, no. 3-4, pp. 913-916, 2010.

[6] H. Yoo and J. J. T. S. F. Kim, "Growth of Cu2ZnSnS4 thin films using sulfurization of stacked metallic films," vol. 518, no. 22, pp. 6567-6572, 2010.

[7] M. J. S. Olgar and Microstructures, "Optimization of sulfurization time and temperature for fabrication of Cu2ZnSnS4 (CZTS) thin films," vol. 126, pp. 32-41, 2019.

[8] M. Olgar, A. Sarp, A. Seyhan, and R. J. R. E. Zan, "Impact of stacking order and annealing temperature on properties of CZTS thin films and solar cell performance," vol. 179, pp. 1865-1874, 2021.

[9] J. Márquez-Prieto *et al.*, "Impact of the selenisation temperature on the structural and optical properties of CZTSe absorbers," vol. 152, pp. 42-50, 2016.

[10] V. Kumar, A. Dutta, U. P. J. S. Singh, and Microstructures, "Optimization of selenization parameters for fabrication of CZTSe thin film," vol. 144, p. 106578, 2020.

[11] S. van Duren et al., "Pre-annealing of metal stack precursors and its beneficial effect on kesterite absorber properties and device performance," vol. 185, pp. 226-232, 2018.
[12] M. Arasimowicz, M. Thevenin, and P. J. J. M. O. P. L. Dale, "The effect of soft pre-annealing of differently stacked Cu-Sn-Zn precursors on the quality of Cu2ZnSnSe4 absorbers," vol. 1538, pp. 123-129, 2013.
[13] M. A. Olgar *et al.*, "Effect of heat treating metallic constituents on the properties of Cu2ZnSnSe4 thin films formed by a two-stage process," vol. 624, pp. 167-174, 2017.
[14] S. Chen, A. Walsh, X. G. Gong, and S. H. J. A. m. Wei, "Classification of lattice defects in the kesterite Cu2ZnSnS4 and Cu2ZnSnSe4 earth-abundant solar cell absorbers," vol. 25, no. 11, pp. 1522-1539, 2013.
[15] J. J. Scragg, T. Ericson, T. Kubart, M. Edoff, and C. J. C. o. M. Platzer-Bjorkman, "Chemical insights into the instability of Cu2ZnSnS4 films during annealing," vol. 23, no. 20, pp. 4625-4633, 2011.
[16] D. R. Lide, *CRC handbook of chemistry and physics*. CRC press, 2004.
[17] M. A. Olgar *et al.*, "Influence of copper composition and reaction temperature on the properties of CZTSe thin films," vol. 682, pp. 610-617, 2016.
[18] A. J. P. r. Patterson, "The Scherrer formula for X-ray particle size determination," vol. 56, no. 10, p. 978, 1939.
[19] D. Santos-Cruz, S. Mayén-Hernández, F. de Moure-Flores, J. Campos-Álvarez, M. Pal, and J. J. R. i. p. Santos-Cruz, "CuOX thin films by direct oxidation of Cu films deposited by physical vapor deposition," vol. 7, pp. 4140-4144, 2017.

Eurasian Journal of Science Engineering and Technology

Research

EFFECT OF CALCINATION TEMPERATURE AND CA:EG RATIO ON TL AND OSL CURVE COMPONENTS OF NEIGHBORITE

Veysi GUCKAN[1,*]

[1]*Physics Department, Cukurova University, 01330, Saricam, Adana, Turkey*

ABSTRACT

This study reveals the differences created by varying calcination temperature and citric acid/ethylene glycol ratio (CA:EG) in thermoluminescence (TL) and optically stimulated luminescence (OSL) curves so that the Neighborite ($NaMgF_3$) compound synthesized using sol-gel can be used as a radiation dosimeter. While producing $NaMgF_3$ phosphors, four different calcination temperatures (700, 800, 900 and 1000 °C) were applied for the calcination process. Characterization analyzes of the samples were performed using X-ray diffraction (XRD) and Scanning electron microscopy (SEM). It was observed that the oxide phases in the crystal structure of the sample increased gradually with increasing calcination temperature. At 1000 °C, it was observed that the crystal structure of the sample was deformed and moved away from the aimed structure. Considering the signal intensities in the TL and OSL glow curves obtained after radiation exposure and the data in the characterization analyzes, the calcination temperature of 800 °C was determined as the optimum temperature. This calcination temperature was kept constant and the samples were reproduced by changing the CA:EG ratio in four different ways (2:4, 4:4, 8:4 and 16:4). By comparing all the sample, the samples with the best crystallization and the most suitable surface morphology were determined. In TL glow curves, it was observed that deep traps could be formed only in samples calcined at 800 °C. Likewise, it was observed from the OSL glow curves that the samples calcined at 800 °C had higher sensitivity. It has been stated that the low sensitivity of the samples calcined at high temperatures is due to the density of the oxide phases formed in the calcination process.

Keywords: Thermoluminescence, Optically stimulated luminescence, Neighborite, Calcination conditions, Computerized deconvolution, Sol-gel technique

1. INTRODUCTION

Perovskites, with their variable formulas, flexible structures, numerous unique properties, and efficacy in a wide range of applications, are becoming hotspots and are being studied extensively [1,2]. The first identified perovskite is CaTiO3 by Gustav Rose in 1839 is named after the mineralogist L. A. Perovski [3], and then its formula is found in numerous new forms, such as ABX3, A3B2X9, etc., where A and B are cations (A has a larger radius than B) and X is a halogen or oxygen anion is derived [4]. Perovskite materials with a wide variety of properties and wide applications can be produced from different compositions and structures [5–8]. For example, luminescent perovskites are used in lighting [9], displays [10], biological imaging [11] or sensing [12], while some photoelectric perovskites are used in areas such as electrocatalysis [13] and photo-catalysis [14]. While the fields of use of perovskites with magnetic properties are magnetic cooling [15], information storage [16], biomedical imaging [17]; electrical perovskites are used to prepare ionic conductors [18], dielectric devices [19], etc. As we approach the present date, it is observed that researchers have done a lot of research into the luminescence in solid-state perovskites. The oldest known of these comes from a Chinese text published in the Song dynasty. Among these studies, luminescent perovskites have important applications in the fields of solar cells [20], lighting devices [21], scintillators [22], electronic devices; such as capacitors [23] or converters [24] or radiation dosimeters [25,26] . It would be helpful for readers to read some review articles for more information [27–29].

The mineral $NaMgF_3$, a material with a perovskite structure, was named Neighborite after the work of geologist Frank Neighbor, and then Chao and his colleagues described this mineral crystallographically [30]. O'Keefe and colleagues noted the structural similarity between NaMgF3 and MgSiO3 in the late 1970s [31]. Zhao and colleagues have done extensive work by studying the phase transitions [32] changing with temperature, and the structure of NaMgF3 [33]. NaMgF3 crystallizes into an orthorhombic crystal system and is identified in the space group Pcmn. It has a tetragonal structure between 760 and 900 oC and above 900 oC the unit cell becomes cubic [30].

The researchers stated that NaMgF3 has an effective atomic number (Zeff=10.4) close to the tissue equivalent and is a host compound that can be used for optical radiation dose estimation by OSL and RL methods, especially when used with lanthanide ions. It has been observed by some researchers that NaMgF3, which had many luminescence studies before, exhibited some

---

* Corresponding author, e-mail: veysiguckan@gmail.com (V. Guckan)

Recieved: 11.04.2022 Accepted: 07.06.2022
doi: 10.55696/ejset.1101711

interesting photoluminescence properties with divalent or trivalent lanthanides. In addition to the luminescence of trivalent lanthanides such as Pr [34], Er [35], Ce [36], Eu [37], Sm [38], Yb [39], Gd [40] and Dy [41], divalent lanthanides such as Sm [42,43], Yb [44] and Eu [45] were also reported.

In generally, NaMgF$_3$ is prepared using solid-state reactions. However, direct melting of the constituent fluorides has also been used. Simpler new techniques such as the solvothermal method, two-stage wet chemical methods have also been used recently. Fluoride salts are used as precursors in high-temperature techniques. Due to the ability of chlorine ions to prevent hydrolysis, some wet chemical methods that lead to the formation of OH-free fluorides are also preferred. It is necessary to remove traces of water to avoid parasitic oxyfluoride phases and thermal treatment should be in a reductive atmosphere. We obtained NaMgF$_3$ phosphors containing different activators by sol-gel method from metal fluoride solutions.

In this study, optimization studies were carried out for the variables (calcination temperature and CA:EG ratio) in the production process of the NaMgF$_3$ material, which was examined by some researchers for its use in the field of radiation dosimetry and stated to have superior dosimetric properties and very bright TL and OSL signals. NaMgF$_3$ microparticles with fluoride-based perovskite structure were obtained in laboratory conditions by Sol-gel method. For NaMgF$_3$, where no such optimization was found, the differences in calcination temperature and citric acid ratio in structure and luminescence efficiency were tested. It is thought that the optimization studies of the calcination temperature in this study will shed light on future dosimetric studies while investigating the effect of both TL and OSL signals. In this study, in which the difference in luminescence efficiency with the differences created by the calcination temperature in the host matrix was revealed, the differences in both TL and OSL curves were revealed by changing the CA:EG ratio. In addition, the luminescence efficiency of the doped NaMgF$_3$ samples produced using the optimized calcination temperature and CA:EG ratio is also presented.

2. MATERIAL AND METHOD

2.1. Sample preparation

In this study, the NaMgF$_3$ (Neighborite) sample as perovskite-type fluorides was synthesized using the sol-gel technique. NaMgF$_3$ polycrystal powder were prepared using the polycrystalline compound of NaF *(≥99.0%, Sigma Aldrich)* and MgF_2 *(≥99.99%, Sigma-Aldrich)* inappropriate proportions. Ethylene glycol (EG) solution *($C_2H_6O_2$, 99.8%, Sigma-Aldrich)* and citric acid (CA) *($C_6H_8O_7$, 99.5%, Sigma-Aldrich)* were used as a solvent and a reactant, respectively, with four different CA:EG ratios *(2:4, 4:4, 8:4 and 16:4).* The calcination process was performed using a high-temperature furnace at four different temperatures *(700, 800, 900 and 1000 °C)* for 2 h. To keep oxidation to a minimum and to prevent oxide formation, the oxygen level was reduced by passing argon gas through the furnace chamber during calcination process.

2.2. Luminescence measurements

Thermoluminescence and optically stimulated luminescence readouts were performed using a RisØ DA-20 TL/OSL reader system. This reader has a 90Sr–90Y beta source with the 6.689 Gy/min dose rate and 2.27 MeV maximum energy. All luminescence signals were recorded with a bialkaline photomultiplier tube (PMT) unit and Schott BG-39 (330-620 nm VIS range) and Hoya U 340 (290-390 nm UV range) filters placed in front of it. The luminescent samples were first irradiated with a beta dose of 0.2 Gy and then TL read-outs were performed from room temperature up to 500 °C. OSL readings were performed using the blue light source with a wavelength of 470 nm for 100 seconds of continuous stimulation (CW-OSL). All TL readouts and OSL pre-heatings were performed at 5 °Cs^{-1} heating rate.

3. RESULTS AND DISCUSSION

3.1. Structural Analysis

3.1.1. XRD

NaMgF$_3$ microparticles were successfully produced in laboratory conditions using the sol-gel method. The inconsistencies in TL and OSL curves obtained after the production stage and the different dose responses of different batches were problematic, and more consistent results were aimed by obtaining optimum conditions with the variables of calcination temperature and CA:EG ratio. In this way, the opportunity to test the luminescence efficiency with varying calcination temperatures and CA:EG mol ratios was occurred. Figure 1a presents the X-ray diffraction patterns of NaMgF$_3$ samples obtained using the sol-gel method and calcined at four different calcination temperatures ranging from 700 to 1000 °C. After the calcination temperature was determined, the CA:EG variable was tested at 2:4, 4:4, 8:4 and 16:4 ratios. The XRD patterns of the NaMgF$_3$ microparticles obtained as a result of the production, in which the CA:EG ratios vary, are given in Figure 1b. As seen in the figure, it was observed that the characteristic $NaMgF_3$ peaks as well as small oxide peaks increased with the increase of calcination temperature. However, it was observed that the structure was completely destroyed at 1000 °C or a different structure was formed unlike the $NaMgF_3$ phase. It is observed in the TL and OSL curves that the luminescence efficiency also decreases sharply with the deterioration of the structure (see Figure 3a and 4a). Different CA:EG mole ratios were compared in samples produced at 800 °C calcination temperature. The samples in which both the crystallization was better than the others (see Figure 1) and especially the OSL signals were the most intense (see Figure 4) were the $NaMgF_3$ microparticles produced in a 2:4 mole ratio. Miller indices of the main crystal structure of all the $NaMgF_3$ samples obtained except 1000 °C calcination temperature were indicated for the peaks associated with $NaMgF_3$ reported in the ICSD card numbered as ICSD:98-009-4085 and matched well with its Pnma space group with orthorhombic structure. In order to minimize oxidation and prevent the formation of oxide phases, the calcination process was carried out in an argon atmosphere. However, since the calcination process was carried out in a non-completely isolated high temperature furnace, this could not be prevented. Several oxide phases not mentioned here, for example MgO, were observed in the crystal structure.

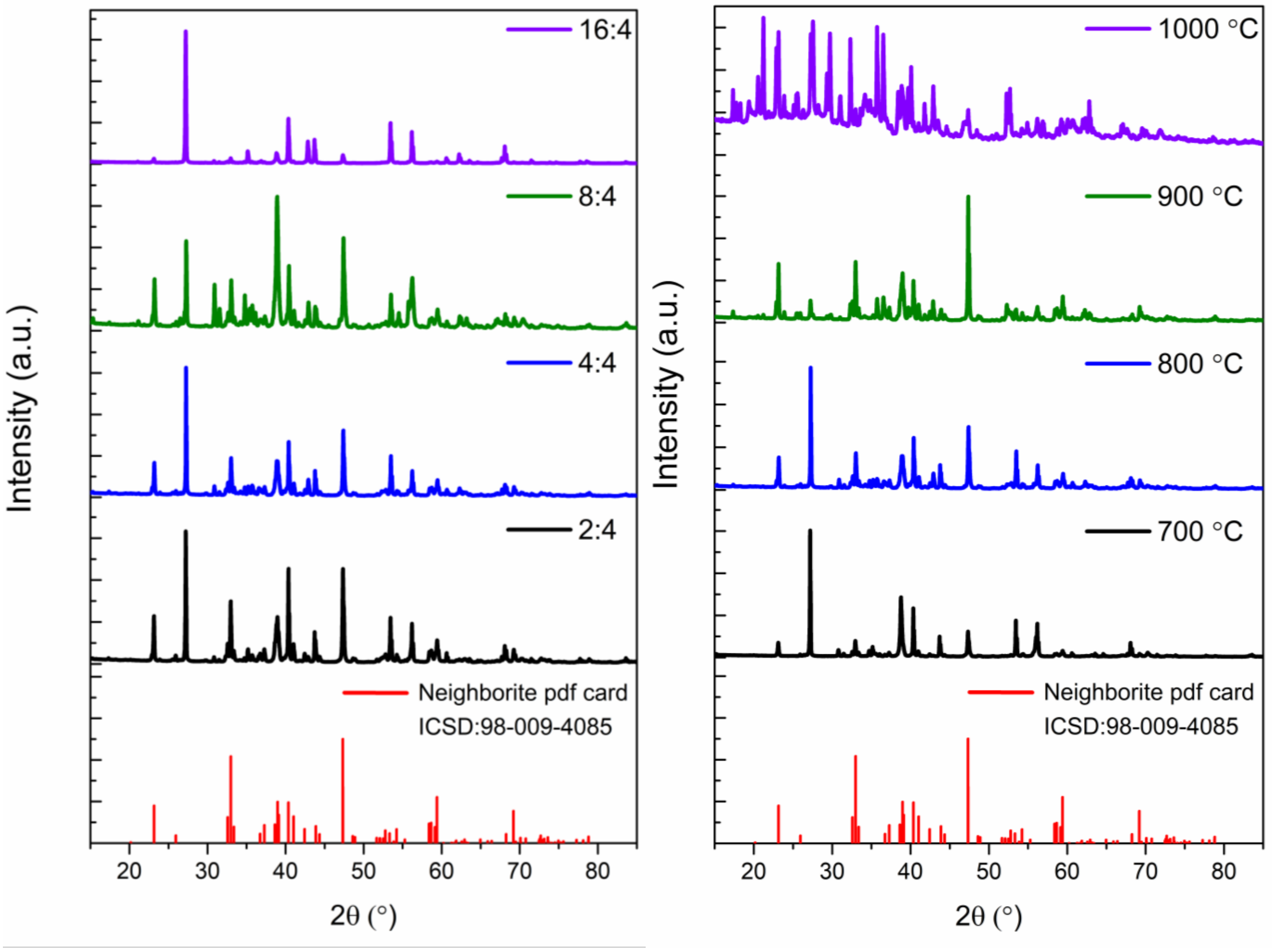

Figure 1. XRD patterns of $NaMgF_3$ microparticles synthesized using the sol-gel methods with different calcination temperatures and CA:EG molar ratios.

3.1.2. SEM

The surface morphology of $NaMgF_3$ fluoroperovskite was analyzed with SEM analysis at different magnifications of 5000 and 10000x. A series of SEM images of $NaMgF_3$ microparticles obtained with calcination conditions (700, 800, 900 and 1000 °C) and CA:EG molar ratios (2.4, 4:4, 8:4 and 16:4) were recorded. Increasing calcination temperatures in the $NaMgF_3$ structure improved the crystallinity of powders. SEM images reveal that the microparticles exhibit a self-repetitive image in a continuous distribution for all samples. (Figure 2a). In the SEM images obtained after the constant calcination temperature of 800 °C of the samples produced at different CA:EG ratios, it was observed that the homogeneous morphology on the surface in all case (see Figure 2b).

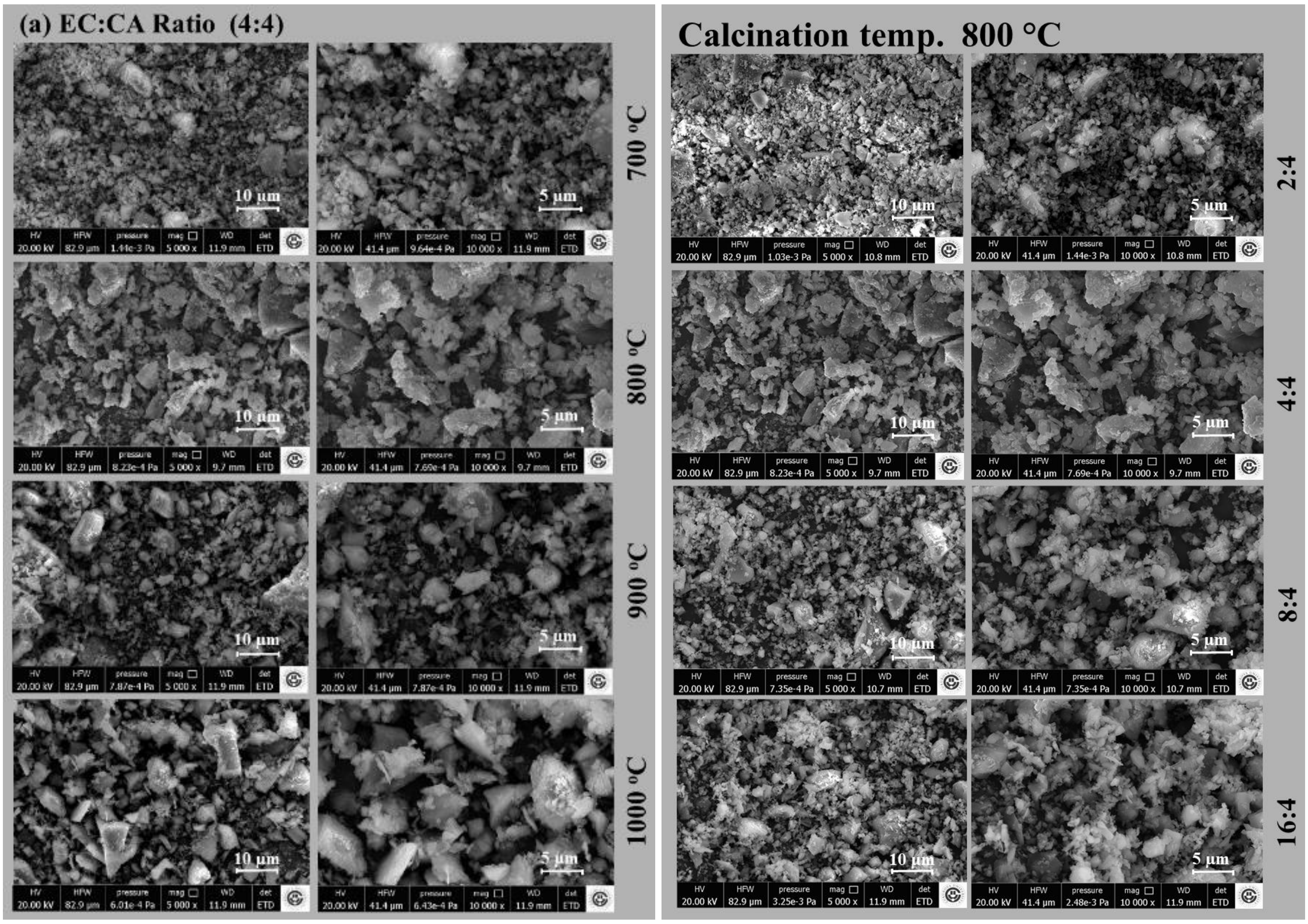

Figure 2. SEM images of the $NaMgF_3$ samples prepared using sol-gel method (a) calcined at different temperature and (b) prepared in different CA:EG molar ratios.

3.2. Luminescence characterization

3.2.1. TL glow curve analysis

TL glow curves of undoped $NaMgF_3$ obtained using the sol-gel method are given in Figures 3a and 3b. As can be seen from the TL glow curves due to different calcination temperatures, TL peaks were observed at around 75 and 120 °C with different intensities depending on the trap groups of $NaMgF_3$ phosphorus. Unlike the others, there was another broad TL peak, which appeared weaker than the other peaks between 225 and 360 °C under the 800 °C calcination condition. In generally, TL peaks located at high temperatures in TL glow curves of dosimeters are preferred because they indicate deeper traps than those at lower temperatures and relatively more stable signals are obtained from these traps. In such a case, the optimum calcination temperature was chosen as 800 °C. And then, by keeping this temperature constant, $NaMgF_3$ phosphor was reproduced with the four different ratios of CA-EG. It can be clearly seen that the 4:4 ratio of the CA:EG exhibits higher intensity TL signals than the others and can create deep traps. It should be noted that the TL glow curves here were recorded with a Schott BG-39 VIS band pass filter with transmittance in the visible region (330-620 nm).

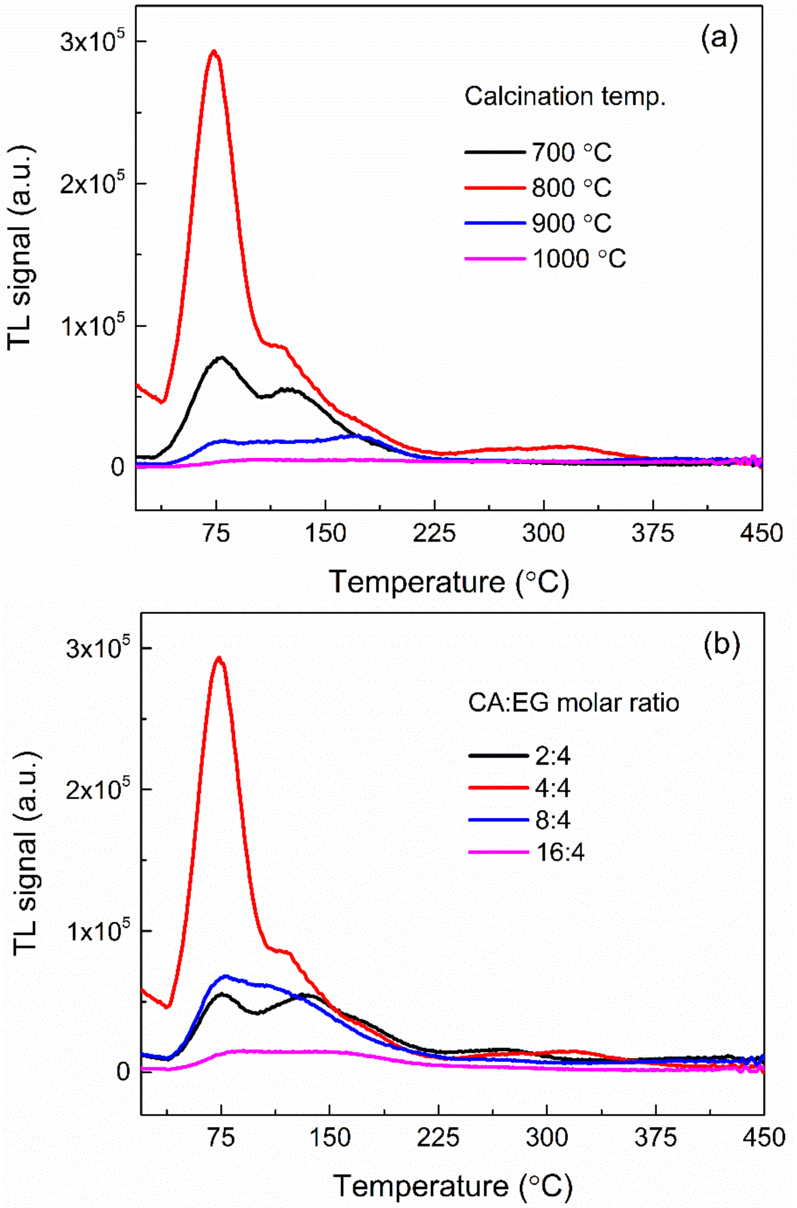

Figure 3. TL glow curves of $NaMgF_3$ differing with varying (a) calcination temperature and (b) CA:EG ratio. TL glow curves were recorded by heating from room temperature to 450 °C without preheating, and each TL glow curve presented was obtained by averaging the TL signals recorded from 3 samples.

The computerized glow curve deconvolution technique (CGCD) was used with the help of the Microsoft Excel spreadsheet [46] can be used for the analysis of the complex TL curves which have overlapping peaks. The kinetic parameters such as E_a, s, and b were calculated assuming the general order kinetic which is described by Kitis et al. [47]. The components which they are created in the TL glow curve are given in Figure 4. Goodness of fit value as Figure of Merit (FOM) was determined as 2.23%. Calculated kinetic parameters E_a, s, and b values were shown in Table 1. Activation energies were observed to have an increasing tendency between 0.76 and 1.17 eV. The frequency factors corresponding to the peaks were determined between 10^8-10^{10} s^{-1}. The lifetimes τ of the traps were calculated using Equation 1 [48] as 2.45 minutes, 1.30 hours, 5.15 days, 4.50 years and $1.50\text{x}10^3$ years, respectively.

$$\tau = s^{-1} exp\left(\frac{E}{kT}\right) \tag{1}$$

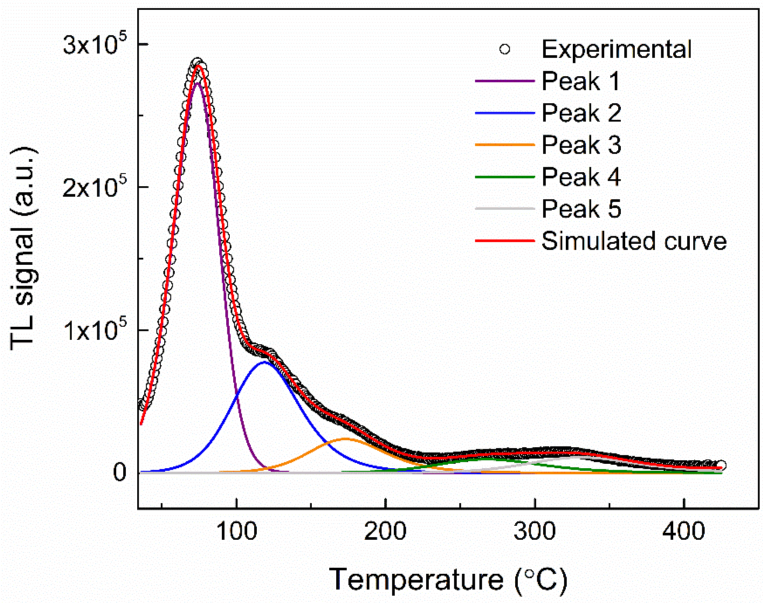

Figure 4. Deconvoluted TL glow curve from undoped $NaMgF_3$ using sol-gel method calcined at 800 °C with the CA:EG ratio of 4:4.

Table 1. Kinetic parameters obtained from deconvoluted TL glow curve

	T_{max} (°C)	**E(eV)**	**s (Hz)**	**b (a.u.)**	**τ**	**FOM (%)**
Peak 1	74	0.76	$3.38x10^{10}$	1.35	2.45 m	
Peak 2	118	0.80	$4.79x10^{9}$	2.00	1.30 h	
Peak 3	173	0.92	$6.15x10^{9}$	2.00	5.15 d	2.23
Peak 4	267	0.99	$2.94x10^{8}$	2.00	4.50 y	
Peak 5	330	1.17	$1.04x10^{9}$	2.00	$1.50x10^{3}$ y	

3.2.2. Continuous-wave OSL decay curve analysis

The OSL decay curves of the $NaMgF_3$ phosphors were recorded using 100 s blue light stimulation from samples calcined at different calcination temperatures with different ratio of CA:EG. The recorded OSL decay curves after 100 °C preheating of the $NaMgF_3$ samples are compared in Figure 5. Figure 5a presents the OSL signals of $NaMgF_3$ samples calcined at different calcination temperatures as a function of time. It was observed that the samples calcined at 800 °C gave the most intense OSL signals. This is thought to be due to the fact that the $NaMgF_3$ phase is formed more smoothly at 800 °C than the others and that different oxide phases are less common in the crystal structure. Figure 5b presents the OSL signals of $NaMgF_3$ samples produced with different CA:EG molar ratios and calcined at 800 °C as a function of time. Here, it was observed that the samples produced with the CA:EG ratio of 2:4 gave the most intense OSL signals among them.

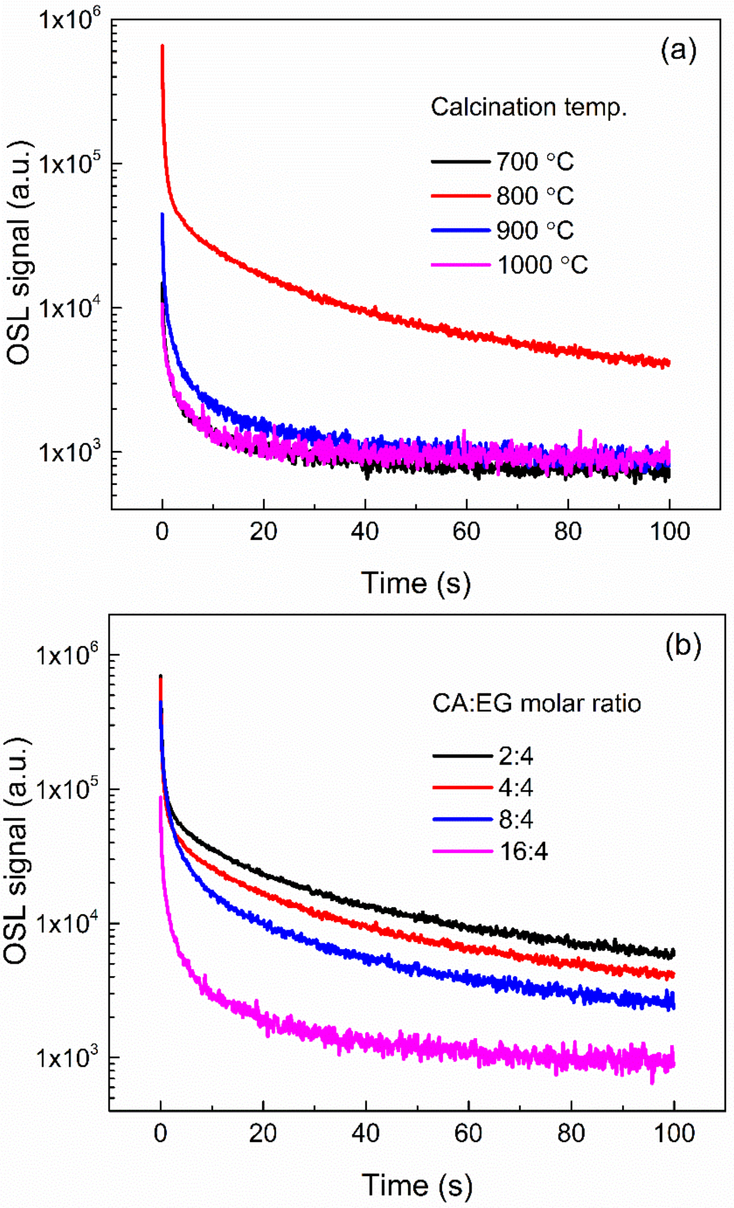

Figure 5. OSL decay curves of the NaMgF3 phosphors prepared using sol-gel method (a) at different calcination temperatures and (b) using different CA:EG ratios. OSL curves were recorded by blue light stimulation after 100 °C preheating, and each OSL decay curve presented was obtained by averaging the OSL signals recorded from 3 samples.

The CW-OSL decay curve of all $NaMgF_3$ samples were analyzed using the fitting method according to time decaying functions (see Figure 6) approximated by general-order which can be written as follows;

$$I\,(t) = bkg + I_1\left[1 + (b_1 - 1)\frac{t}{\tau_1}\right]^{-\frac{b_1}{b_1-1}} + I_2\left[1 + (b_2 - 1)\frac{t}{\tau_2}\right]^{-\frac{b_2}{b_2-1}} + \cdots \qquad (2)$$

where, each component is named as fast, medium and slow component, respectively, according to their lifer times $\tau_{1,2,3}$ values. $I(t)$ is the OSL intensity as a function of time, $I_{1,2,3..}$are the amplitudes, t is the stimulation time and bkg is the background signal of the reader. The decay of the undoped $NaMgF_3$ samples prepared with different conditions were characterized by a fast initial decay and then the medium and a slower decay. The fitting curves for all the undoped $NaMgF_3$

samples estimated using the three components were statistically found well. The related kinetic parameters and FOM value are given in Table 2.

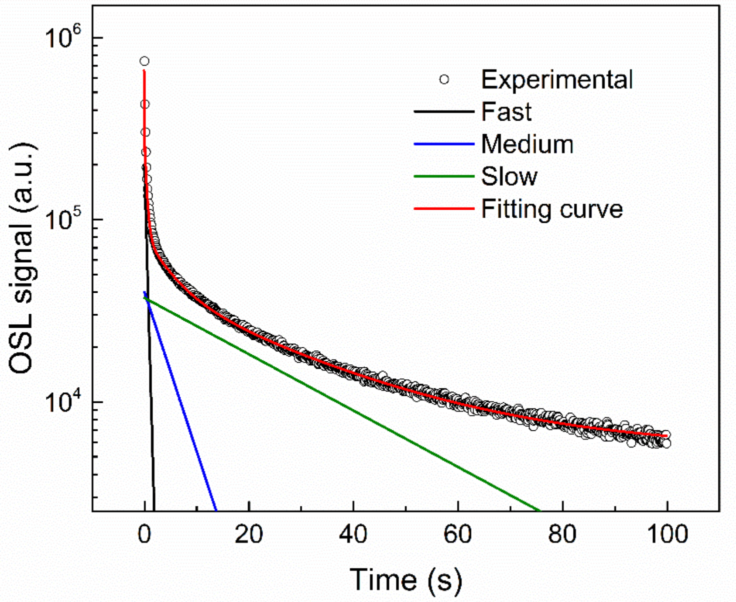

Figure 6. The OSL decay curve of the undoped $NaMgF_3$ calcined at 800 °C with the CA:EG ratio of 2:4 and its fast, medium and slow components.

Table 2. Decay constants for fast, medium and slow components of the OSL decay curve of $NaMgF_3$.

		Fast		**Medium**		**Slow**			
		A1	t1	A2	t2	A3	t3	bkg	FOM
CA:EG	Temp.								
4:4	700 °C	4853.87	0.46	2689.24	2.82	887.37	18.58	793.22	2.14
	800 °C	180917.70	0.38	32811.33	4.22	26785.06	25.25	3807.55	2.01
	900 °C	13861.43	0.42	7038.30	2.66	1763.43	19.26	936.01	2.35
	1000 °C	2323.34	0.45	2608.24	3.13	481.1763	18.38	920.05	2.96
Temp.	CA:EG								
800 °C	4:2	200588.01	0.43	40062.94	4.96	37222.76	28.06	543.50	1.76
	4:4	180917.70	0.38	32811.33	4.22	26785.06	25.25	3807.55	2.01
	4:8	137440.70	0.62	50339.46	3.34	15867.50	23.42	2307.60	2.11
	4:16	21923.39	0.47	10701.47	2.83	2858.22	18.69	989.36	2.86

4. CONCLUSION

In this study, $NaMgF_3$ samples were produced successfully with the uncommon sol-gel production technique. In XRD diffraction patterns, it is observed that the crystal structure gradually deteriorates due to the increasing calcination temperature and at the same time, different oxide phases increase. At the calcination temperature of 1000 °C, it is seen that the structure has completely deteriorated. This was an expected situation [30]. Obtained $NaMgF_3$ samples except 1000 °C are reported in the ICSD card numbered ICSD:98-009-4085 and fit well with the orthorhombic structure in Pnma space group. The complexity of the surface morphology (possibly due to the presence of oxide phases) makes it pointless to observe the effect of varying calcination temperature or CA:EG ratio. It is seen that TL peaks at low temperature are more intense in TL glow curves taken from samples obtained under different conditions. It was observed that high temperature TL peaks were obtained only in $NaMgF_3$

samples calcined at 800 °C and with a CA:EG ratio of 4:4, and the kinetic parameters of this curve were estimated by the CGCD method. Its activation energies of the traps corresponding to each TL peak were observed to have an increasing tendency between 0.76 and 1.17 eV. The situation did not change much in the OSL decay curves taken from the $NaMgF_3$ samples. Only $NaMgF_3$ samples calcined at 800 °C and with CA:EG ratios of 2:4 or 4:4 had high-intensity. The decay constants with its fast, medium and slow components of these OSL curves were estimated using fitting curve method.

This study reveals the changes in TL and OSL curves with changing calcination conditions and CA:EG ratio in the use of $NaMgF_3$ samples for dosimetric purposes, and the kinetic parameters that change depending on these changes. It is suggested that $NaMgF_3$ phosphorus has a high potential as a radiation dosimeter and should be investigated further for this purpose, and it is thought that this study will shed light on future studies.

SIMILARTY RATE: 19%

ACKNOWLEDGEMENT

I would like to thank Prof. Dr. Zehra YEGINGIL for the opportunities and valuable opinions she provided.

This research is sponsored by NATO's Emerging Security Challenges Division in the framework of “The Science for Peace and Security Programme (SPS)”. Financial assistance from the NATO SPS MYP under the research contract number G5647 are acknowledged. I would like to thank the Cukurova University Research Projects Development and Coordination Unit under FUA-2021-13936 are gratefully acknowledged.

REFERENCES

[1] Y. Zhang, W. Jie, P. Chen, W. Liu, J. Hao, Y. Zhang, P. Chen, W. Liu, W. Jie, J. Hao, Ferroelectric and Piezoelectric Effects on the Optical Process in Advanced Materials and Devices, Advanced Materials. 30 (2018) 1707007. https://doi.org/10.1002/ADMA.201707007.

[2] Y. Wei, Z. Cheng, J. Lin, An overview on enhancing the stability of lead halide perovskite quantum dots and their applications in phosphor-converted LEDs, Chemical Society Reviews. 48 (2019) 310–350. https://doi.org/10.1039/C8CS00740C.

[3] Z. Cheng, J. Lin, Layered organic–inorganic hybrid perovskites: structure, optical properties, film preparation, patterning and templating engineering, CrystEngComm. 12 (2010) 2646–2662. https://doi.org/10.1039/C001929A.

[4] Z. Zeng, Y. Xu, Z. Zhang, Z. Gao, M. Luo, Z. Yin, C. Zhang, J. Xu, B. Huang, F. Luo, Y. Du, C. Yan, Rare-earth-containing perovskite nanomaterials: design, synthesis, properties and applications, Chemical Society Reviews. 49 (2020) 1109–1143. https://doi.org/10.1039/C9CS00330D.

[5] R. Saha, A. Sundaresan, C.N.R. Rao, Novel features of multiferroic and magnetoelectric ferrites and chromites exhibiting magnetically driven ferroelectricity, Materials Horizons. 1 (2013) 20–31. https://doi.org/10.1039/C3MH00073G.

[6] W.J. Yin, B. Weng, J. Ge, Q. Sun, Z. Li, Y. Yan, Oxide perovskites, double perovskites and derivatives for electrocatalysis, photocatalysis, and photovoltaics, Energy & Environmental Science. 12 (2019) 442–462. https://doi.org/10.1039/C8EE01574K.

[7] L. Wang, H. Zhou, J. Hu, B. Huang, M. Sun, B. Dong, G. Zheng, Y. Huang, Y. Chen, L. Li, Z. Xu, N. Li, Z. Liu, Q. Chen, L.D. Sun, C.H. Yan, A Eu 3+ -Eu 2+ ion redox shuttle imparts operational durability to Pb-I perovskite solar cells, Science (1979). 363 (2019) 265–270. https://doi.org/10.1126/SCIENCE.AAU5701/SUPPL_FILE/AAU5701_WANG_SM.PDF.

[8] X. Zhang, Z. Li, H. Zhang, S. Ouyang, Z. Zou, Luminescence properties of Sr2ZnWO6:Eu3+ phosphors, Journal of Alloys and Compounds. 469 (2009) L6–L9. https://doi.org/10.1016/J.JALLCOM.2008.01.117.

[9] J.S. Yao, J. Ge, B.N. Han, K.H. Wang, H. bin Yao, H.L. Yu, J.H. Li, B.S. Zhu, J.Z. Song, C. Chen, Q. Zhang, H.B. Zeng, Y. Luo, S.H. Yu, Ce3+-Doping to Modulate Photoluminescence Kinetics for Efficient CsPbBr3 Nanocrystals Based Light-Emitting Diodes, J Am Chem Soc. 140 (2018) 3626–3634. https://doi.org/10.1021/JACS.7B11955/SUPPL_FILE/JA7B11955_SI_001.PDF.

[10] Y. Cheng, C. Shen, L. Shen, W. Xiang, X. Liang, Tb3+, Eu3+ Co-doped CsPbBr3 QDs Glass with Highly Stable and Luminous Adjustable for White LEDs, ACS Applied Materials and Interfaces. 10 (2018) 21434–21444. https://doi.org/10.1021/ACSAMI.8B05003/SUPPL_FILE/AM8B05003_SI_001.PDF.

[11] M. Pellerin, E. Glais, T. Lecuyer, J. Xu, J. Seguin, S. Tanabe, C. Chanéac, B. Viana, C. Richard, LaAlO3:Cr3+, Sm3+: Nano-perovskite with persistent luminescence for in vivo optical imaging, Journal of Luminescence. 202 (2018) 83–88. https://doi.org/10.1016/J.JLUMIN.2018.05.024.

[12] T. Addabbo, F. Bertocci, A. Fort, M. Gregorkiewitz, M. Mugnaini, R. Spinicci, V. Vignoli, Gas sensing properties of YMnO3 based materials for the detection of NOx and CO, Sensors and Actuators B: Chemical. 244 (2017) 1054–1070. https://doi.org/10.1016/J.SNB.2017.01.054.

[13] G. Chen, Y. Zhu, H.M. Chen, Z. Hu, S.F. Hung, N. Ma, J. Dai, H.J. Lin, C. te Chen, W. Zhou, Z. Shao, An Amorphous Nickel–Iron-Based Electrocatalyst with Unusual Local Structures for Ultrafast Oxygen Evolution Reaction, Advanced Materials. 31 (2019) 1900883. https://doi.org/10.1002/ADMA.201900883.

[14] E. Grabowska, Selected perovskite oxides: Characterization, preparation and photocatalytic properties—A review, Applied Catalysis B: Environmental. 186 (2016) 97–126. https://doi.org/10.1016/J.APCATB.2015.12.035.

[15] B. Arun, V.R. Akshay, G.R. Mutta, C. Venkatesh, M. Vasundhara, Mixed rare earth oxides derived from monazite sand as an inexpensive precursor material for room temperature magnetic refrigeration applications, Materials Research Bulletin. 94 (2017) 537–543. https://doi.org/10.1016/J.MATERRESBULL.2017.07.006.

[16] Y. Cao, S. Cao, W. Ren, Z. Feng, S. Yuan, B. Kang, B. Lu, J. Zhang, Magnetization switching of rare earth orthochromite CeCrO3, Applied Physics Letters. 104 (2014) 232405. https://doi.org/10.1063/1.4882642.

[17] X. Chen, J. Song, X. Chen, H. Yang, X-ray-activated nanosystems for theranostic applications, Chemical Society Reviews. 48 (2019) 3073–3101. https://doi.org/10.1039/C8CS00921J.

[18] T. Asano, A. Sakai, S. Ouchi, M. Sakaida, A. Miyazaki, S. Hasegawa, Solid Halide Electrolytes with High Lithium-Ion Conductivity for Application in 4 V Class Bulk-Type All-Solid-State Batteries, Advanced Materials. 30 (2018) 1803075. https://doi.org/10.1002/ADMA.201803075.

[19] X. Liu, N. Kent, A. Ceballos, R. Streubel, Y. Jiang, Y. Chai, P.Y. Kim, J. Forth, F. Hellman, S. Shi, D. Wang, B.A. Helms, P.D. Ashby, P. Fischer, T.P. Russell, Reconfigurable ferromagnetic liquid droplets, Science (1979). 365 (2019) 264–267. https://doi.org/10.1126/SCIENCE.AAW8719/SUPPL_FILE/AAW8719S9.MP4.

[20] C.M. Sutter-Fella, Y. Li, M. Amani, J.W. Ager, F.M. Toma, E. Yablonovitch, I.D. Sharp, A. Javey, High Photoluminescence Quantum Yield in Band Gap Tunable Bromide Containing Mixed Halide Perovskites, Nano Letters. 16 (2016) 800–806. https://doi.org/10.1021/ACS.NANOLETT.5B04884/SUPPL_FILE/NL5B04884_SI_001.PDF.

[21] Y. Kim, E. Yassitepe, O. Voznyy, R. Comin, G. Walters, X. Gong, P. Kanjanaboos, A.F. Nogueira, E.H. Sargent, Efficient Luminescence from Perovskite Quantum Dot Solids, ACS Applied Materials and Interfaces. 7 (2015) 25007–25013. https://doi.org/10.1021/ACSAMI.5B09084/SUPPL_FILE/AM5B09084_SI_001.PDF.

[22] M.D. Birowosuto, D. Cortecchia, W. Drozdowski, K. Brylew, W. Lachmanski, A. Bruno, C. Soci, X-ray Scintillation in Lead Halide Perovskite Crystals, Scientific Reports 2016 6:1. 6 (2016) 1–10. https://doi.org/10.1038/srep37254.

[23] H. Yokoi, N. Wakiya, K. Shinozaki, N. Mizutani, Dielectric Properties and its Frequency Dependence of BaTiO3 Thin Film Single-Layer Capacitor that is Applicable to Multilayer Structure, Key Engineering Materials. 269 (2004) 229–232. https://doi.org/10.4028/WWW.SCIENTIFIC.NET/KEM.269.229.

[24] I. Dursun, C. Shen, M.R. Parida, J. Pan, S.P. Sarmah, D. Priante, N. Alyami, J. Liu, M.I. Saidaminov, M.S. Alias, A.L. Abdelhady, T.K. Ng, O.F. Mohammed, B.S. Ooi, O.M. Bakr, Perovskite Nanocrystals as a Color Converter for Visible Light Communication, ACS Photonics. 3 (2016) 1150–1156. https://doi.org/10.1021/ACSPHOTONICS.6B00187/SUPPL_FILE/PH6B00187_SI_001.PDF.

[25] V. Guckan, D. Kaya, V. Altunal, A. Ekicibil, F. Karadag, A. Ozdemir, Z. Yegingil, Impact of Li concentration in KMgF3:Eu,Yb fluoroperovskite on structure and luminescence properties, Journal of Alloys and Compounds. 902 (2022) 163810. https://doi.org/10.1016/J.JALLCOM.2022.163810.

[26] Z. Li, X. An, X. Cheng, X. Wang, … H.Z.-C., undefined 2014, First-principles study of the electronic structure and optical properties of cubic Perovskite NaMgF3, Iopscience.Iop.Org. (n.d.). https://iopscience.iop.org/article/10.1088/1674-1056/23/3/037104/meta (accessed April 10, 2022).

[27] X. Li, F. Cao, D. Yu, J. Chen, Z. Sun, Y. Shen, Y. Zhu, L. Wang, Y. Wei, Y. Wu, H. Zeng, All Inorganic Halide Perovskites Nanosystem: Synthesis, Structural Features, Optical Properties and Optoelectronic Applications, Small. 13 (2017) 1603996. https://doi.org/10.1002/SMLL.201603996.

[28] D.B. Mitzi, Templating and structural engineering in organic–inorganic perovskites, Journal of the Chemical Society, Dalton Transactions. 0 (2001) 1–12. https://doi.org/10.1039/B007070J.

[29] D. Chen, X. Chen, Luminescent perovskite quantum dots: synthesis, microstructures, optical properties and applications, Journal of Materials Chemistry C. 7 (2019) 1413–1446. https://doi.org/10.1039/C8TC05545A.

[30] E.C.T. Chao, H.T. Evans Jr, B.J. Skinner, C. Milton, Neighborite, NaMgF3, a new mineral from the green river formation, South Ouray, Utah, American Mineralogist: Journal of Earth and Planetary Materials. 46 (1961) 379–393.

[31] M. O’Keeffe, J.O. Bovin, Solid Electrolyte Behavior of NaMgF3: Geophysical Implications, Science (1979). 206 (1979) 599–600. https://doi.org/10.1126/SCIENCE.206.4418.599.

[32] K.S. Knight, G.D. Price, J.A. Stuart, I.G. Wood, High-temperature structural phase transitions in neighborite: A high-resolution neutron powder diffraction investigation, Physics and Chemistry of Minerals. 42 (2015) 45–52. https://doi.org/10.1007/S00269-014-0698-5/FIGURES/3.

[33] Y. Zhao, D.J. Weidner, J. Ko, K. Leinenweber, X. Liu, B. Li, Y. Meng, R.E.G. Pacalo, M.T. Vaughan, Y. Wang, A. Yeganeh-Haeri, Perovskite at high P-T conditions: An in situ synchrotron X ray diffraction study of NaMgF3 perovskite, Journal of Geophysical Research: Solid Earth. 99 (1994) 2871–2885. https://doi.org/10.1029/93JB02757.

[34] N.J.M. le Masson, A.P. Vink, P. Dorenbos, A.J.J. Bos, C.W.E. VanEijk, J.P. Chaminade, Ce3+ and Pr3+5d-energy levels in the (pseudo) perovskites KMgF3 and NaMgF3, Journal of Luminescence. 101 (2003) 175–183. https://doi.org/10.1016/S0022-2313(02)00411-8.

[35] Y.P. Du, Y.W. Zhang, Z.G. Yan, L.D. Sun, S. Gao, C.H. Yan, Single-Crystalline and Near-Monodispersed NaMF3 (M=Mn, Co, Ni, Mg) and LiMAlF6 (M=Ca, Sr) Nanocrystals from Cothermolysis of Multiple Trifluoroacetates in Solution, Chemistry – An Asian Journal. 2 (2007) 965–974. https://doi.org/10.1002/ASIA.200700054.

[36] S. Watanabe, T. Ishii, K. Fujimura, K. Ogasawara, First-principles relativistic calculation for 4f–5d transition energy of Ce3+ in various fluoride hosts, Journal of Solid State Chemistry. 179 (2006) 2438–2442. https://doi.org/10.1016/J.JSSC.2006.04.040.

[37] J.J. Schuyt, G.V.M. Williams, Oxygen-impurity charge transfer in NaMgF3:Ln (Ln = Yb, Sm, or Eu): Establishing the lanthanide energy levels in NaMgF3, Journal of Luminescence. 211 (2019) 413–417. https://doi.org/10.1016/J.JLUMIN.2019.04.004.

[38] J.J. Schuyt, G.V.M. Williams, Radiation-induced changes in the optical properties of NaMgF3(Sm): Observation of resettable Sm radio-photoluminescence, Materials Research Bulletin. 106 (2018) 455–458. https://doi.org/10.1016/J.MATERRESBULL.2018.06.039.

[39] J. Zhang, J. Wang, J. Xie, L. Wang, Q. Zhang, Enhancement of upconversion luminescence intensity in NaMgF3:2.5%Yb3+, 0.5%Er3+ nanocrystals with Eu3+ doping, Journal of Materials Science: Materials in Electronics. 32 (2021) 20882–20890. https://doi.org/10.1007/S10854-021-06604-Z/FIGURES/8.

[40] M. Venkata Narayana, K. Somaliah, L.H. Brixner, Thermally stimulated luminescence of gadolnium-activated NaMgF3 at 77 K, Crystal Research and Technology. 25 (1990) K209–K213. https://doi.org/10.1002/CRAT.2170250921.

[41] J.J. Schuyt, G.V.M. Williams, Photoluminescence of Dy3+ and Dy2+ in NaMgF3:Dy: A potential infrared radiophotoluminescence dosimeter, Radiation Measurements. 134 (2020) 106326. https://doi.org/10.1016/J.RADMEAS.2020.106326.

[42] J.J. Schuyt, G.V.M. Williams, Quenching of the Sm2+ luminescence in NaMgF3:Sm via photothermal ionization: Alternative method to determine divalent lanthanide trap depths, Applied Physics Letters. 115 (2019) 181104. https://doi.org/10.1063/1.5122669.

[43] J.C. Gâcon, A. Gros, H. Bill, J.P. Wicky, New measurements of the emission spectra of Sm2+ in KMgF3 and NaMgF3 crystals, Journal of Physics and Chemistry of Solids. 42 (1981) 587–593. https://doi.org/10.1016/0022-3697(81)90107-4.

[44] H. Nalumaga, J.J. Schuyt, R.D. Breukers, G.V.M. Williams, Radiation-induced changes in the photoluminescence properties of NaMgF3:Yb nanoparticles: Yb3+ → Yb2+ valence conversion and oxygen-impurity charge transfer, Materials Research Bulletin. 145 (2022) 111562. https://doi.org/10.1016/J.MATERRESBULL.2021.111562.

[45] V.S. Singh, P.D. Belsare, S. v. Moharil, Synthesis, characterization, and luminescence studies of rare-earth-activated NaMgF3, Luminescence. 37 (2022) 89–96. https://doi.org/10.1002/BIO.4149.

[46] D. Afouxenidis, G.S. Polymeris, N.C. Tsirliganis, G. Kitis, Computerised curve deconvolution of TL/OSL curves using a popular spreadsheet program, Radiation Protection Dosimetry. 149 (2012) 363–370. https://doi.org/10.1093/RPD/NCR315.

[47] G. Kitis, J.M. Gomez-Ros, J.W.N. Tuyn, Thermoluminescence glow-curve deconvolution functions for first, second and general orders of kinetics, Journal of Physics D: Applied Physics. 31 (1998) 2636. https://doi.org/10.1088/0022-3727/31/19/037.

[48] V. Pagonis, G. Kitis, C. Furetta, Numerical and practical exercises in thermoluminescence, (2006). Numerical and practical exercises in thermoluminescence. Springer Science & Business Media, 2006.